MSc Thesis

Active Gust Load Alleviation for Flexible Wing Aircraft

Y.L. Ferrier

April 20th, 2017

Faculty of Aerospace Engineering

NASA Ames Research Center

Special thanks to Sjors for the design of the cover.

Active Gust Load Alleviation for Flexible Wing Aircraft

MASTER OF SCIENCE THESIS

To obtain the degree of Master of Science in Aerospace Engineering at Delft University of Technology

Y.L. Ferrier

April 20, 2017

Thesis committee:	dr. ir. Q.P. Chu,	TU Delft
	dr. ir. C.C. de Visser,	TU Delft
	ir. X. Wang,	TU Delft
	dr. ir. N.T. Nguyen,	NASA Ames
	dr. ir. R. De Breuker,	TU Delft

TU Delft

Preface

The report in front of you does not only mark the end of a nine-month thesis where I had the chance to integrate all the knowledge and skills I have gained in my academic career, but also marks the end of my student time at the TUDelft.

This thesis has proven to be an interesting challenge, in which I had to familiarize myself with new aerospace domains such as unsteady aerodynamics and aeroelasticity and combine this new knowledge with my specialization in control systems. My experience with this thesis has been very pleasant and I would like to acknowledge the people that have supported me during this research.

I would especially like to express my gratitude to my daily supervisors, Dr. de Visser, Dr. Chu and Sherry Wang. Your insightful guidance, flexibility, and enthusiasm were fundamental for the success of this thesis.

I am very thankful to Dr. Nguyen who gave me the opportunity to visit the Intelligent Systems Division at NASA Ames Research Center. Your mentorship and guidance have enhanced my research capabilities and inspired me to go the extra mile.

It was a great pleasure to work with the Advanced Control and Evolvable Systems Group at NASA Ames Research Center. I would like to thank Eric Ting, Daniel Chaparro and Michael Drew for their tremendous support.

Also, I want to express a warm thank you to Monique, Lucien, Ines, Yasmin, Sebastian and Frederique for their advice, mental support, and distraction when needed. You motivated me when times were tough and helped me celebrate the successes.

Lastly, I would like to thank the members of the thesis committee in advance for their time and effort.

Y.L. Ferrier
Delft, April 2017

Contents

Acronyms

AASC	Adaptive Aeroelastic Shape Control
ADR	Active Disturbance Rejection
AGLA	Active Gust Load Alleviation
ARE	Algebraic Ricatti Equation
ASE	Aeroservoelastic
CFD	Computational Fluid Dynamics
DOF	Degrees of Freedom
ESAC	Elastically Shaped Aircraft Concept
ESO	Extended State Observer
GLA	Gust Load Alleviation
GTM	Generic Transport Model
IMU	Inertial Measurement Unit
LIDAR	Light Detection and Ranging
LQG	Linear-Quadratic Gaussian
LQR	Linear-Quadratic Regulator
MLA	Maneuver Load Alleviation
MOFC	Multi-objective Flight Control
MPC	Model Predictive Control
MRAC	Model Reference Adaptive Control
NASA	National Aeronautics and Space Administration
NESO	Nonlinear Extended State Observer
OBLTR	Observer-based Robust Control with Loop Transfer Recovery
PAAW	Performance Adaptive Aeroelastic Wing
PID	Proportional Integral Derivative
VCCTEF	Variable Camber Continuous Trialing Edge Flap

List of Figures

List of Tables

1

Introduction

1.1. Background

The introduction of composite materials in commercial aircraft has disrupted the aviation industry. Airframes comprised of composite materials provide the same load-carrying capacity as aluminum structures at much lower weight. The reduction in weight that is afforded by using composite airframes can translate into a fuel consumption advantage. This advantage has triggered aircraft manufacturers to design the airframes of their new-generation aircraft mostly out of composite materials. Examples are the Boeing 787 Dreamliner and the Airbus A350 XWB, which use at least 50% composite materials in the airframe construction.

The usage of composite materials as the base of the airframe comes at a cost. Composite materials provide less structural rigidity than aluminum structures. Together with the trend of having high-aspect ratio wings in modern commercial aircraft, this lower structural rigidity can lead to large aeroelastic deflections at off-design flight conditions. Large aeroelastic deflections and aeroelastic interaction can degrade the aerodynamic efficiency and decrease the control surface effectiveness of the flexible wing aircraft. The decrease in aerodynamic efficiency can negate the benefit of lightweight composite structures by increasing the aircraft drag and hence the fuel burn. Furthermore, the lower rigidity makes the aircraft more sensitive to disturbances, affecting the ride and handling qualities.

A multi-disciplinary approach is needed to ensure that the aerodynamic efficiency and control effectiveness of high-aspect ratio flexible wing aircraft are retained. This approach should not only focus on neutralizing the negative aeroelastic effects but should also make use of the flexibility to improve the aerodynamic efficiency and handling of the aircraft. This can be achieved by deliberately reshaping the wing to adapt to various flight conditions. This idea is inspired by nature, where birds constantly change the camber of their wings to adjust to different flight stages. For this purpose, Performance Adaptive Aeroelastic Wing (PAAW) technology is developed. The wing is aeroelastically reshaped in flight to achieve an optimal performance throughout the flight envelope.

Besides a potential decrease in aerodynamic efficiency, flexible wing aircraft encounter operational constraints that must be addressed by PAAW technology. These constraints include reduced aeroelastic stability margins, increased airframe responses to gust and maneuver loads, and degraded pilot handling and ride qualities. A multi-objective flight control solution must be designed to maximize the aerodynamic performance while simultaneously addressing these operational constraints.

The Variable Camber Continuous Trailing Edge Flap (VCCTEF) is a candidate concept for PAAW technology. The VCCTEF has been jointly developed by NASA and Boeing Research & Technology under the NASA Fixed Wing project. The concept was originally developed under a NASA Innovation Fund study entitled "Elastically Shaped Future Air Vehicle Concept" in 2010 [1]. The VCCTEF is a multi-segment flap system that can change the camber of the wing to achieve an optimal lift distribution.

1.2. Problem statement

Previous research has investigated the possibilities of PAAW technology and the implementation of the VCCTEF as an aeroelastic wing shaping control device. The effectiveness of the VCCTEF within a multi-objective flight control design has been investigated with respect to aeroelastic mode suppression [2], drag reduction [3–5], real-time drag minimization [6] and maneuver load alleviation [7].

The response of a high-aspect ratio flexible wing aircraft to wind gusts and turbulence is another important segment of the multi-objective flight control design. Gust load alleviation is dedicated to diminishing the detrimental effects of gusts and turbulence. The objective of this thesis is to implement a gust load alleviation control approach within a multi-objective flight control framework for a flexible wing aircraft embodied with the VCCTEF.

This thesis objective will be achieved by answering the main research question and a set of sub-questions (SQ). The main research question is formulated as:

How can gust load alleviation be provided within a multi-objective flight control framework and with the use of the Variable Camber Continuous Trailing Edge Flap for a flexible wing aircraft?

The following sub-questions need to be answered to answer the main research question:

SQ1. *How do you integrate different control objectives within a multi-objective flight control framework?*

SQ2. *What are the state-of-the-art control methods for gust load alleviation?*

SQ3. *How can the Variable Camber Continuous Trailing Edge Flap be used for gust load alleviation?*

SQ4. *What metrics are used to evaluate the performance of a gust load alleviation control method?*

SQ5. *What is the state-of-the-art in gust model development?*

SQ6. *What are the dynamics, characteristics, and limitations of a flexible wing aircraft?*

Sub-questions 1, 2, and 3 will be answered in the literature study in chapters 3, 4, and 2, respectively. Sub-question 4 will be discussed in chapter 9. Sub-questions 5 and 6 will be answered in the third part on aircraft and turbulence model development in chapters 5 and 6. The main research question will be answered in the conclusion of this thesis in chapter 11.

1.3. Research approach

The first part of the thesis consists of a literature study. The goal of this literature study is to familiarize with Performance Adaptive Aeroelastic Wing technology, multi-objective flight control, and gust load alleviation. This is followed by an analysis of the aircraft and turbulence models and the development of the control design.

A multi-objective flight control (MOFC) framework will be designed with the inclusion of aeroelastic mode suppression, drag reduction, and gust load alleviation. An active gust load alleviation (AGLA) control approach is designed, which means that the controller directly suppresses the effect of the disturbance. To achieve this, the disturbance is estimated using an Extended State Observer (ESO). The controller consists of a baseline Linear-Quadratic Gaussian (LQG) controller that is augmented with Model Reference Adaptive Control (MRAC). The MRAC augmentation is the adaptive increment that provides the active gust load alleviation.

The performance of the multi-objective flight controller with active gust load alleviation is evaluated in simulations against a nominal rigid controller. The simulations use an aeroservoelastic model of the NASA Generic Transport Model integrated with the VCCTEF and a 1D severe von Kármán turbulence model. Next to this, the active gust load alleviation controller is validated for various turbulence scenarios.

1.4. Report structure

This report presents the literature survey, aeroservoelastic model, control design, and simulation and validation results for the thesis on Active Gust Load Alleviation for Flexible Wing Aircraft.

The first part contains an in-depth literature review divided into three chapters: Performance Adaptive Aeroelastic Wing technology (chapter 2), Multi-Objective Flight Control (chapter 3) and Gust Load Alleviation (chapter 4). The second part presents the formulation of the aeroservoelastic model (chapter 5) and the turbulence model (chapter 6). The third part discusses the control design. The multi-objective flight control design is derived in chapter 7. The active gust load alleviation and disturbance estimation are presented in chapter 8. The fourth part presents the simulation and validation results and the conclusions of the thesis. A discussion on performance metrics and the simulation results are given in chapter 9. The validation results are summarized in chapter 10. The conclusions and recommendations are discussed in chapter 11.

The relationship between the concepts that are discussed in the report is illustrated in Figure 1.1.

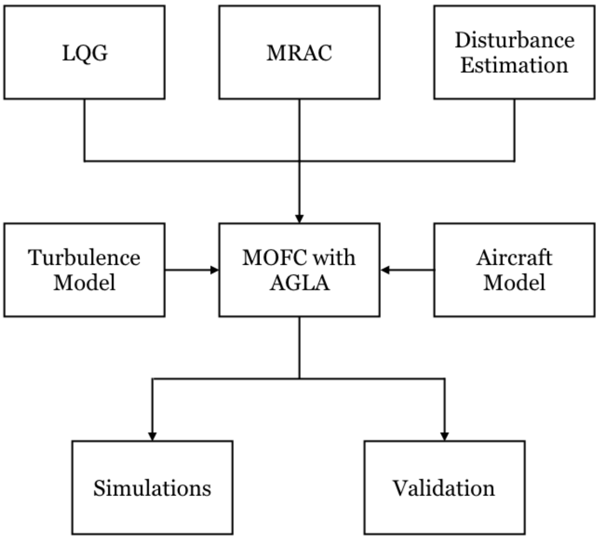

Figure 1.1: The relation between different concepts in this report

A conference paper is written on the content of this thesis and is added in Appendix F. This paper covers to a great extent the work presented in this report.

I

Literature Review

2

Performance Adaptive Aeroelastic Wing Technology

Performance Adaptive Aeroelastic Wing technology is a multi-disciplinary approach to ensure control effectiveness and aerodynamic efficiency of flexible wing aircraft. The idea is to aeroelastically reshape the wing in flight to adapt to various flight conditions. This is similar to birds adapting their wing shapes to achieve optimal performance during various flight phases [8] as illustrated in Figure 2.1.

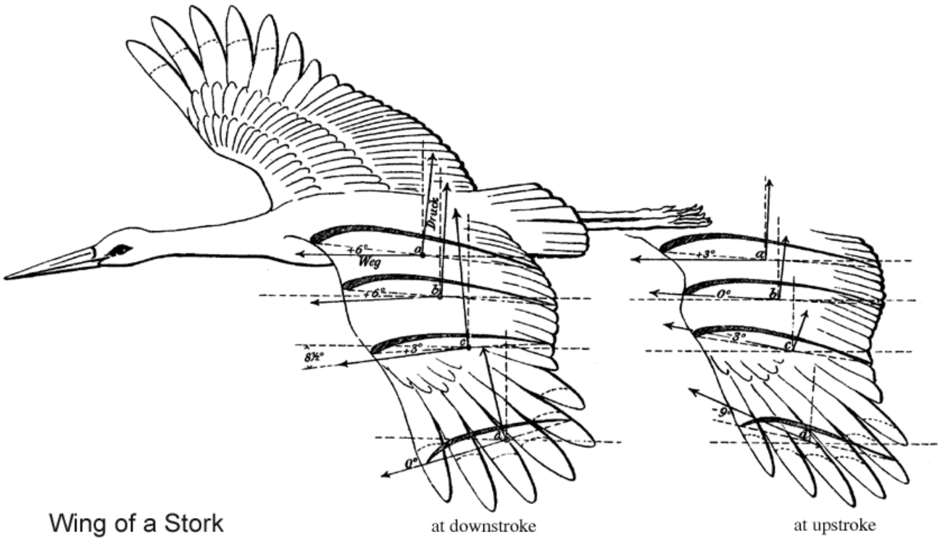

Figure 2.1: Birds can change their wing shape to adapt to various flight phases [9]

By aeroelastically shaping the wing, an optimum performance can be reached throughout the flight envelope. This has a great advantage over the traditional, more rigid wing, that needs to compromise its aerodynamic design to be sufficient at specific flight conditions. The advantages are amongst others, reduced fuel burn due to reduced drag, higher lift to drag ratios, and enhanced lift performance during take-off and landing [1].

2.1. Adaptive aeroelastic wing shaping

PAAW technology uses adaptive aeroelastic wing shaping to improve the aerodynamic performance of the aircraft in various flight conditions. The adaptive aeroelastic wing shaping consists of two assets:

1. The wing twist is optimized for the flexible wing aircraft design.
2. A multi-segment trailing-edge flap system improves the aerodynamics.

The influence of these assets on the aerodynamic performance is described by the formulation of the local angle of attack α_c. The local angle of attack influences the lift distribution and span load of the wing and thus the aerodynamic performance. The local angle of attack is described by the following equation:

$$\alpha_c = \alpha - \gamma - \Theta \cos\Lambda - W_x \sin\Lambda + \frac{\partial \alpha}{\partial \delta}\delta + \left(\frac{\partial \Theta}{\partial \delta}\cos\Lambda + \frac{\partial W}{\partial \delta}\sin\Lambda\right)\delta \tag{2.1}$$

where α is the aircraft angle of attack, γ is the twist of the jig shape, Θ is the wing torsional twist about the elastic axis, W is the wing vertical bending along the elastic axis, Λ is the sweep angle of the elastic axis and δ is the deflection of the multi-segment trailing-edge flap system [10].

In Equation 2.1, the term $\Theta \cos\Lambda - W_x \sin\Lambda$ represents the wing deflection in bending and torsion. The adaptive aeroelastic wing shaping is described by the last two terms in Equation 2.1. The term $\frac{\partial \alpha}{\partial \delta}\delta$ describes the influence of the multi-segment trailing-edge flap system on the aerodynamics and the terms $\frac{\partial \Theta}{\partial \delta}$ and $\frac{\partial W}{\partial \delta}$ describe the wing twist shaping control.

2.2. Variable camber continuous trailing edge flap

The Variable Camber Continuous Trailing Edge Flap is a candidate concept for Performance Adaptive Aeroelastic Wing technology. The VCCTEF was first introduced by Nguyen in a NASA Innovation Fund study in 2010 [1].

The VCCTEF is a novel trailing-edge flap system that enables aeroelastic wing shaping control. The flap system, illustrated in Figure 2.2, covers the entire span of the trailing-edge of the wings. From its introduction in 2010 onwards, the design has been evaluated and improved [11, 12]. Studies analyzed amongst all the optimal number of flap sections, flap section widths, and the camber shape. The VCCTEF is illustrated on the GTM aircraft in Figure 2.2. This thesis research uses the latest version of the VCCTEF design.

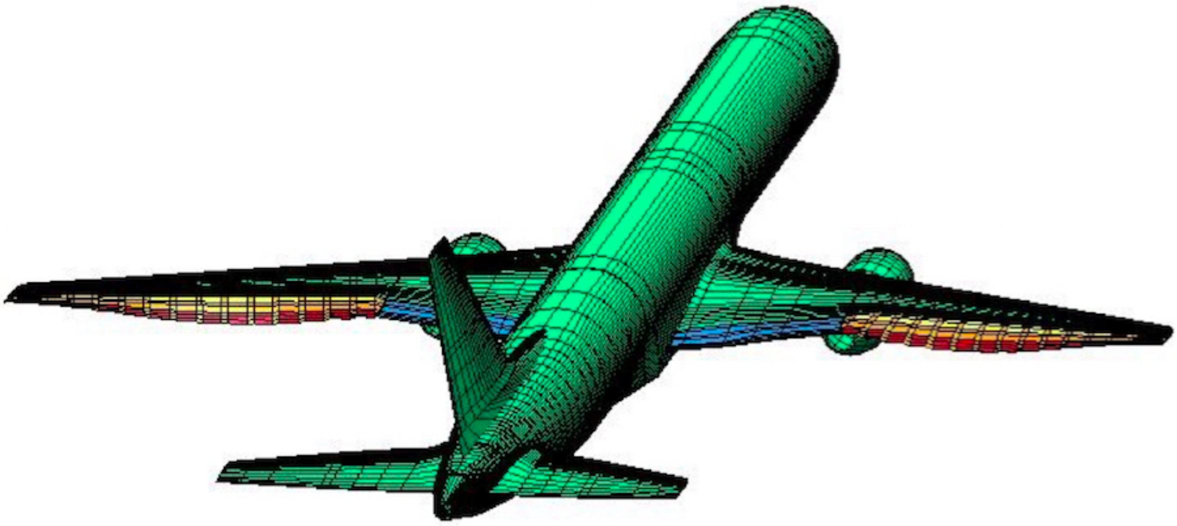

Figure 2.2: Generic transport model with VCCTEF

2.2.1. Spanwise lay-out and functionality

The VCCTEF contains 16 individual spanwise sections that enable different flap settings at each spanwise position. The flap system has one large flap section attached to the inner wing, and 15 smaller flap sections attached to the outer wing. The layout of the VCCTEF is illustrated on the left wing in Figure 9.12.

The individual flap sections can be deflected to change the wing twist shape spanwise. The wing twist shape directly influences the local lift distribution and thus the aerodynamic properties. The wing twist can be adjusted to minimize the drag for a specific lift for different flight stages or aircraft gross weight. This is an advantage over traditional commercial transport designs that must adhere to a fixed jig twist shape applied at manufacture. This jig twist shape is designed for one cruise configuration and thus sub-optimal for other flight phases or fuel loadings. The advantage of the VCCTEF over the traditional wing designs is the possibility to adapt the wing twist setting for different flights phases and depending on the aircraft gross

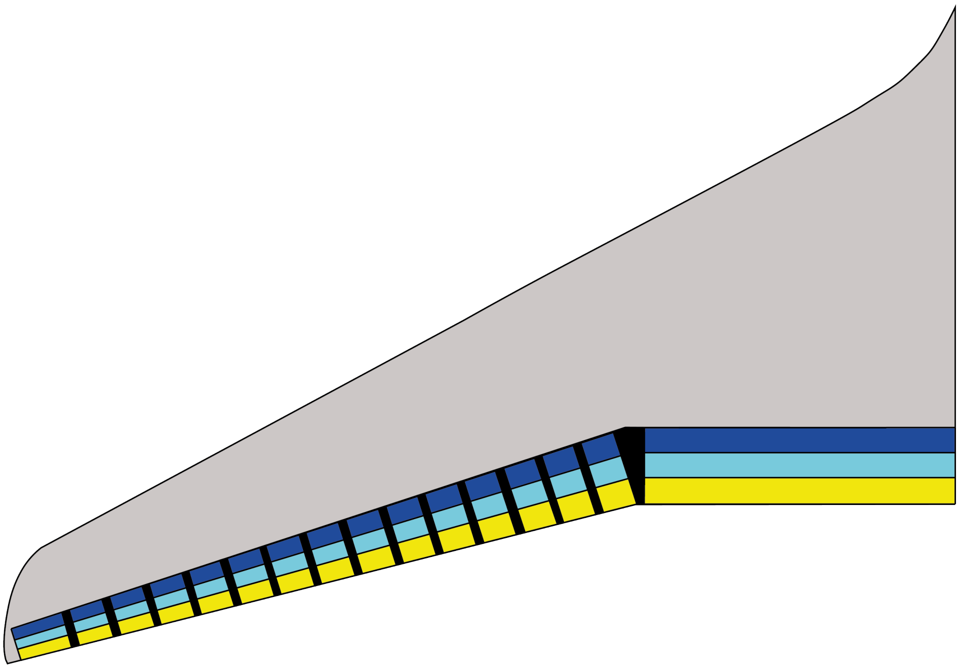

Figure 2.3: Wing configuration with VCCTEF

weight. The wing twist determines the spanwise loading and therefore the VCCTEF can be used to achieve minimum drag at specified lift coefficients.

The multiple spanwise flap sections are connected by an elastomer material and form a continuous trailing edge when the flap sections are deflected. The transition material is illustrated in black in Figure 9.12. The continuous trailing edge flap improves the aerodynamic efficiency by optimizing the spanwise lift distribution. Furthermore, the transition material is needed to prevent discontinuities between the flap sections that can cause the formation of strong vortices, especially when deflected.

2.2.2. Chordwise lay-out and functionality

The flap sections consist of three chordwise segments of equal chord length, illustrated in Figure 2.4. These chordwise segments can be deflected individually to create camber surfaces for the desired aerodynamic performance. In this study, the relative deflection of the chordwise segments is constrained to a circular-arc camber shape, which has a superior aerodynamic performance compared to other camber configurations [13],

$$\delta_{i,1} = \frac{1}{3}\delta_{i,3} \tag{2.2}$$

$$\delta_{i,2} = \frac{2}{3}\delta_{i,3} \tag{2.3}$$

This relation allows the control method to only regard the deflection of the outermost chordwise segment, $\delta_{i,3}$. The deflection angle of each chordwise segment is measured relative to the hinge and the undeflected trailing edge as shown in Figure 2.4.

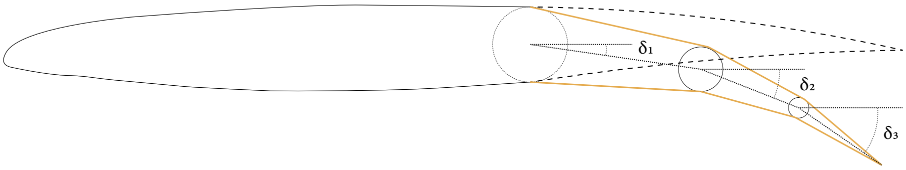

Figure 2.4: Three-segment variable camber continuous trailing edge flap

2.2.3. The role of VCCTEF within PAAW technology

The spanwise and chordwise lay-out of the VCCTEF enable the trailing-edge system to be used for multiple purposes.

The two inner chordwise flap segments are driven by shaped memory alloy actuators. These actuators are relatively slow. The two inner chordwise flap segments thus gradually change the VCCTEF shape. The outermost flap segment is driven by electro-mechanical actuators. These actuators are fast, enabling the outermost flap to have sufficient bandwidth and control power for fast movements.

The technical characteristics of the VCCTEF allow it to fulfill multiple roles within the context of PAAW. On the one hand, it serves as an active aeroelastic effector to optimize the wing shape for the purpose of drag minimization. On the other hand, it can function as a high bandwidth control device, allowing it to be used for flight maneuvering, load alleviation, and aeroelastic mode damping.

Research has been conducted on the use of the VCCTEF within the context of PAAW. Previous research mainly focused on drag reduction, for example at off-design cruise flight conditions [3], at subsonic cruise for rigid wing aircraft [4] and within a multidisciplinary drag optimization study for flexible wing aircraft [5]. These studies show the potential benefit that the VCCTEF can provide for drag reduction through simulation studies. Also, some experimental wind tunnel tests on the usage of the VCCTEF for drag minimization have been done, showing that the VCCTEF can achieve significant drag reduction in practice [14].

3

Multi-Objective Flight Control

The concept of multi-objective flight control is developed to simultaneously address aerodynamic performance optimization and operational constraints that may hinder the performance of flexible wing aircraft.

The design of traditional flight controllers focuses on a pilot command-following objective while taking into account performance and stability requirements. The idea of multi-objective flight control is to include an aerodynamic performance objective in the control design [2]. The aerodynamic performance objective strives to increase the lift-to-drag ratio during different flight phases such as take-off, cruise, landing, and maneuvers. The lift-to-drag ratio is increased by reducing the drag for a specified lift coefficient.

Active aeroelastic wing shaping can be used to simultaneously achieve the pilot command-following and aerodynamic performance objectives.

3.1. Control objectives

The first and foremost objective of a multi-objective flight control design is to follow a pilot command.

The second objective is to improve the aerodynamic performance during the entire flight envelope. As mentioned, the aerodynamic performance objective is translated to maximizing the aircraft lift-to-drag ratio and thus reducing the drag for a specified lift coefficient. The drag reduction is included in the flight control design framework by implementing a drag penalty for the control action.

In addition, two other control issues affect the performance of a flexible wing aircraft and therefore objectives regarding those issues are included in the multi-objective flight control framework.

First of all, stability is the most important consideration in flight control design. The flexibility of the aircraft structure of flexible wing aircraft can degrade the stability margins due to aeroelastic interactions. This can lead to a loss of control. Therefore, the third objective of the multi-objective flight control framework is to provide stability augmentation by suppressing aeroelastic modes. This objective ensures we meet pilot handling quality requirements.

Secondly, flexible wing aircraft also ask for a control approach with regards to gust load and maneuver load alleviation. Due to the flexibility of the aircraft structure, gust disturbances and maneuvers can cause pilot handling and ride quality issues. Gust load alleviation should focus on reducing the aeroelastic response of the aircraft to gust disturbances, while maneuver load alleviation should reduce the loads on the aircraft during maneuvers. The fourth objective of the multi-objective flight control framework is thus to provide gust load and maneuver load alleviation.

To summarize, multi-objective flight control design should compromise the following objectives:

1. traditional pilot command-following flight control

2. drag minimization

3. aeroelastic mode suppression

4. gust load and maneuver load alleviation

3.2. Control architecture

Striving to achieve these four control objectives in a synergistic manner results in a complex flight control design. This complex multi-objective flight control architecture is illustrated in Figure 3.1. The three control objectives that are added to the traditional pilot command-following control design framework are highlighted in green. Additionally, the figure shows the sensors that are required to achieve the different control objectives. The integration of the four control objectives makes the control approach a multi-objective flight control design.

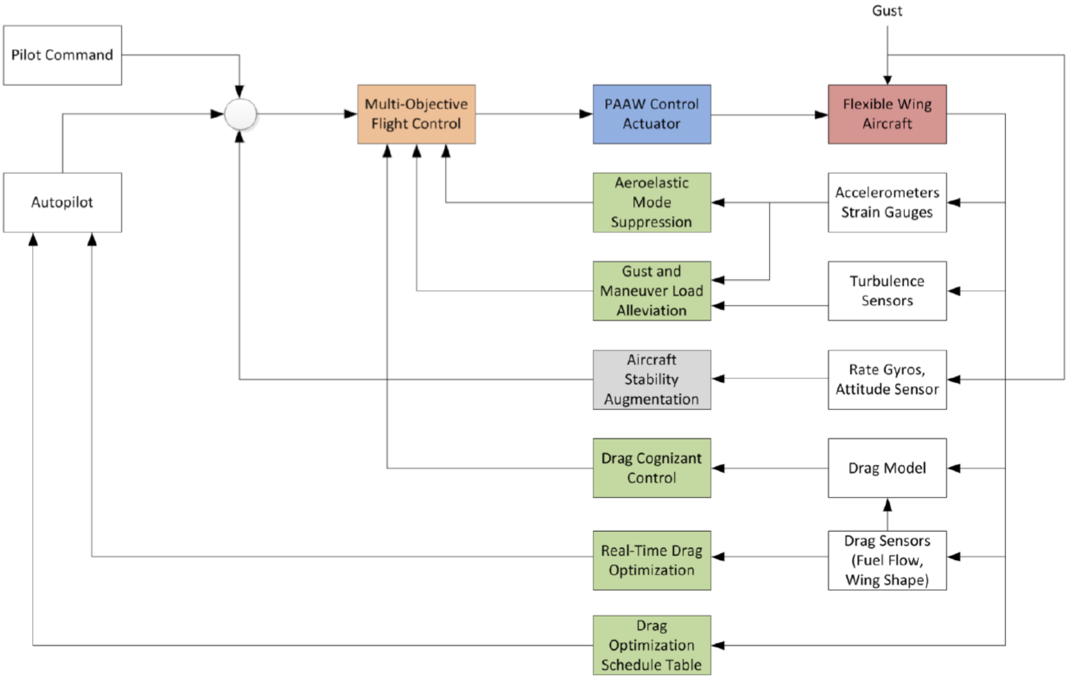

Figure 3.1: Multi-objective flight control architecture [15]

3.3. Previous research implementations

Previous research on multi-objective flight control for a flexible wing aircraft embodied with the VCCTEF has been done on various objectives of the multi-objective flight control framework. A few of the studies will be shortly introduced below.

Nguyen and Tal present a multi-objective flight control approach for aeroelastic mode suppression and drag-cognizant optimal control in 2015 [2]. A simulation shows the ability of the VCCTEF to suppress the aeroelastic modes and reduce drag for a flight path angle command controller. A drag penalty was included in the optimal control cost function to enforce the drag minimization objective.

In 2017, Nguyen et al. study maneuver load alleviation combined with drag minimization in a multi-objective flight control design for a flexible wing aircraft [7]. Maneuver load alleviation is included in the control design by adding a penalty for the wing root bending moment in the optimal control cost function. The study demonstrates the effectiveness of the multi-objective flight control in achieving aeroelastic mode suppression, drag minimization, and maneuver load alleviation while tracking a pilot command.

Furthermore, Ferrier et al. designed a system identification and real-time drag minimization approach using the VCCTEF for a flexible wing aircraft in 2016 [6]. The real-time drag minimization control uses the identified aircraft parameters to determine the VCCTEF control commands while adhering to a specified lift coefficient.

The studies show the benefit of using the VCCTEF to achieve drag reduction while simultaneously addressing operational constraints and meeting multiple control objectives. The next step will be to analyze the effectiveness of the VCCTEF in providing gust load alleviation within a multi-objective flight control framework.

4

Gust Load Alleviation

Gusts and turbulence negatively affect the passenger comfort and can create significant aircraft loads. These loads can result in a reduction of the structural lifetime of the aircraft. Furthermore, due to the coupling of the rigid body and elastic energy of flexible wing aircraft, gusts and turbulence can harm the flying qualities [16].

Gust load alleviation (GLA) aims to mitigate the detrimental effects caused by gusts and turbulence. In the past, this was done by strengthening the wing root joint, since the wing root bending moment induces the maximum load on the aircraft structure. The obvious disadvantage of this approach is the increase in the aircraft structural weight. Nowadays, active control action is used to provide gust load alleviation. Active control action can not only increase the passenger comfort and improve the flying qualities but also enables the reduction of weight by decreasing the loads on the aircraft.

The principle of gust load alleviation using active control action is illustrated in Figure 4.1. The controller activates the control surfaces to change the lift distribution along the wing. The lift distribution directly affects the load distribution.

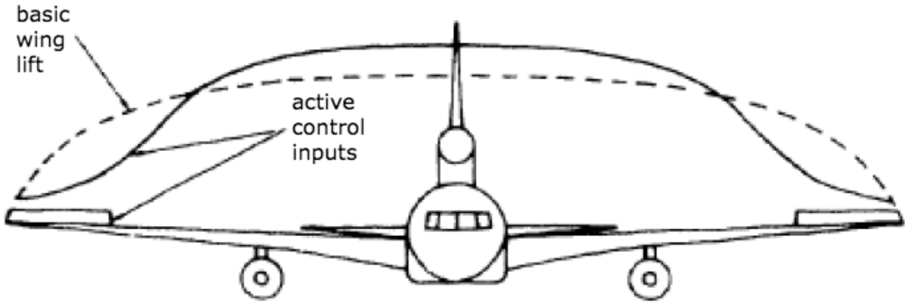

Figure 4.1: Load alleviation using active control inputs [17]

Because of the importance of gust load alleviation, extensive research has been conducted on the topic. In this literature review, the following questions on gust load alleviation are answered for different studies:

- What control surfaces are used for gust load alleviation?
- How is the effect of gust load alleviation evaluated?
- Which control methods are used? What is the conclusion on the performance of this control approach?
- What gust model is used?

4.1. Historical survey of GLA systems in operational aircraft

In 2012, Regan and Jutte present a historical survey and state-of-the-art assessment of active control in gust load alleviation [18]. This report focuses on active control technologies that are evaluated in wind tunnel and flight experiments. From this report, one can conclude that sensor-based robust control methods are applied most frequently in wind tunnel and in-flight studies. The report also emphasizes the importance of sensor technology in the development of gust load alleviation techniques. The switch from old sensor technologies (air data system, inertial sensors) to new sensor technologies (leading edge stagnation points, light detecting and ranging) allows for more real-time and predictive control techniques. The report concludes that no control methodology has been proven to be superior.

In Table 4.1 a summary is given of documented gust load alleviation control systems in operational aircraft.

Table 4.1: Summary of operational aircraft with documented active control systems to mitigate gust response [18]

Aircraft	Principle objective	Sensors	Actuation	Critical improvement metric
C-5A	Load alleviation and fatigue life extension	Inertial	Symmetric aileron	Empty weight reduction 5.5%
L-1011-500	Load alleviation for wing span extension	Inertial	Symmetric aileron and outboard spoilers	Empty weight reduction 1.25% Drag reduction 3%
B-1	Ride quality	Inertial	Canard-like vanes on nose	Empty weight reduction 4.7%
B-2	Load alleviation and ride quality	Aerodynamic and inertial	Inboard elevons and dedicated surface	Gust load reduced 50%
A320	Load alleviation	Inertial	Ailerons, spoilers, and elevators	N\A
A330 and A340	Load alleviation and ride quality	Inertial	Rudders and elevators	N\A
A380	Load alleviation and ride quality	N\A	N\A	N\A
B787	Load alleviation and ride quality	Aerodynamic	Ailerons, spoilers, and elevators	N\A

4.2. Simulation studies of new GLA control methods

Simulation studies have demonstrated the application of modern control techniques for gust load alleviation of flexible wing aircraft. The studies mentioned in this literature review are just a small collection of the extensive research on gust load alleviation. Nevertheless, these studies provide a good overview of the state-of-the-art.

Lucas et al. (2009) compare a linear proportional-integral controller and a nonlinear Lyapunov-based controller for gust load alleviation of a nonlinear flexible aircraft model [19]. The gust is modeled as a 1-cos idealization and the control effectors are the elevators and flaperons. The performance metrics are the horizontal and vertical accelerations of the center of mass and the fuselage and wing pitch angles. The study concludes that the nonlinear controller is able to stabilize the system in response to a gust while the linear controller fails to stabilize the true nonlinear system.

In 2012, Frost et al. use optimal control allocation for gust load alleviation of a generic transport model aircraft [20]. The control framework uses real-time structural load feedback and structural load constraints in the control allocator. The advance in sensor technology makes the use of real-time structural load feedback possible. A 1-cos gust model is simulated and the ailerons are used as control effectors. Gust load alleviation is measured by looking at the bending moments and the rigid-body states. The optimal control allocation framework reduced the bending moments during the gust and the rigid-body states were able to follow the commanded inputs.

In 2012, both Gieseller [21] and Haghighat [22] researched gust load alleviation using model predictive control.

Haghihat considers a 1-cos gust simulation for a simplified flexible aircraft model. Elevators and ailerons are used to provide gust load alleviation. The bending and torsional moments, as well as the vertical load factor, rigid-body states, and mid and root stresses, are analyzed to determine the performance of the gust load alleviation. The study showed that model predictive control can significantly decrease aircraft loads and therefore provide gust load alleviation.

Giesseller extends the approach of model predictive control for gust load alleviation for a full flexible aircraft model. He includes look ahead measurements of incoming gust disturbances to provide active disturbance rejection. These measurements should be made by possible in practice with the use of Light Detection and Ranging (LIDAR). The study analyzes the responses to 3 types of gusts: discrete gusts, sweep gusts, and continuous turbulence. The ailerons, spoilers, and elevator are used as control effectors. The performance metrics are the shear, bending and torsion moments, the vertical load factor, and the rigid-body responses. The study concludes that the predictive nature of model predictive control allows to reduce the dynamic loads and that the active disturbance rejection further improves the gust load alleviation.

Gangsaas analyzed Linear-Quadratic Gaussian (LQG) control for gust load alleviation and flutter suppression in 1981 [23]. The study considers a discrete gust simulation for a flexible airplane. The control effectors are the elevators and the ailerons. The performance metrics are the bending and torsion moments at the wing. The study concludes that LQG provides excellent gust load and flutter mode control.

The last control method that was analyzed in this literature review is H_∞ robust control. Wildschek and Cook implemented this control law in 2009 [24] and 2013 [25], respectively.

Wildschek implements a feedback loop for active wing bending damping together with a feedforward controller for active turbulence rejection. The feedforward controller uses angle of attack measurements from an alpha probe mounted on the nose of the fuselage. A von Kármán turbulence model is simulated for a large airliner aircraft and the control effectors are the elevators, ailerons, and direct-lift-control flaps. The bending moments, vertical load factor and accelerations of the center of gravity are measured to determine the performance of the gust load alleviation. Furthermore, an IS02631 comfort filter is used to determine the improved ride quality. The control solution reduces the loads on the aircraft and improves the ride quality.

Cook implements the H_∞ robust controller for a slender, long endurance, high-aspect ratio very flexible wing aircraft. A discrete gust is modeled and the control effectors are the elevators and the ailerons. The root bending moments are analyzed. The study concludes that the proposed gust load alleviation control works well for short gusts, including a predefined critical gust length, but that the performance decreases for longer gust lengths.

Summarizing, this literature review shows that:

- All high-bandwidth control surfaces can be used for gust load alleviation.
- The performance metrics for gust load alleviation varies in different studies, however the main performance metrics are the wing root bending moment, vertical accelerations at the wing, and the rigid-body state responses.
- A lot of different control methods have been studied for gust load alleviation. In practice, mainly robust sensor-based control methods are used. Although each control method has its advantages and specific applications, it has not been proven that one control method is superior with respect to gust load alleviation.
- Both a discrete 1-cos gust model and a continuous turbulence model can be used to evaluate the gust load alleviation control method.

II

Aircraft and Turbulence Model

5

Elastically Shaped Aircraft Concept with VCCTEF

This chapter describes the aircraft model and dynamics. The full coupled flight dynamic and aeroservoelastic model is presented, as well as a reduced-order version. Furthermore, the actuator dynamics and a virtual control for the VCCTEF are discussed.

5.1. Generic transport model

This study makes use of the NASA Generic Transport Model (GTM). The GTM is a hypothetical aircraft that represents a twin-engine short to medium range transport aircraft. The shape and size are similar to that of a Boeing 757 [26]. A remotely piloted version of the GTM is built and operated at NASA Langley Research Center. This prototype is a 5.5% scaled-down version of the GTM. Figure 5.1 shows the remotely piloted version of the GTM next to a Boeing 757.

Figure 5.1: Boeing 757 and GTM remotely piloted vehicle

Extensive experimental and simulation research on the GTM created a high-fidelity model and database. This makes the GTM an excellent platform for research. The aircraft characteristics of the GTM are summarized in Table 5.1.

Table 5.1: Generic transport model characteristics [1]

Characteristic	**Unit**
Weight	200,000 lbs
Span width	124 ft
Wing reference area	1952 ft^2
Aspect ratio	7.82
Taper ratio	0.212
Mean aerodynamic chord	16.64 ft
Leading edge sweep angle	28.43 deg
Wing dihedral angle	5 deg

The GTM is transformed to a flexible wing aircraft by changing the bending and torsion stiffness. This flexible wing version is called the Elastically Shaped Aircraft Concept (ESAC). The torsion and bending stiffness are decreased to such an extent that the wing deflections almost double with respect to their original values. The bending and torsion stiffness of the ESAC are similar to that of a Boeing 787, shown in cruise configuration in Figure 5.2.

Figure 5.2: Boeing 787

5.2. Coupled flight dynamic and aeroservoelastic model

An aeroservoelastic (ASE) model of the ESAC equipped with the VCCTEF is developed by the Advanced Control and Evolvable Systems Group at NASA Ames Research Center [7]. The ASE model includes the rigid aircraft flight dynamics, wing dynamic aeroelasticity, flight control actuator dynamics of the flap system, and servo-motor dynamics.

Flexible wing aircraft need a coupled flight dynamic and aeroservoelastic model because the frequency separation between the rigid-body modes and aeroelastic modes is not sufficient to avoid flutter modes. This in contrast with more rigid aircraft for which the effect of aeroelasticity can be neglected in the flight dynamics.

This research focuses on symmetric flight conditions, in which the aircraft is in a wing-level flight and its center of gravity moves only in a vertical plane. For this reason, the longitudinal flight dynamics are presented.

5.2.1. Rigid-body dynamics

The rigid-body flight dynamic model of the GTM is based on the 6 degrees-of-freedom (DOF) flight dynamic and kinematic equations.

In general, the rigid-body dynamics are expressed by

$$\begin{aligned} M_r \dot{x}_r = {} & Q_r \dot{x}_r + P_r x_r + D_r \delta_r + V_{rn} \ddot{q} + \left(T_{rn} + 0.5 T_{rc}\right) \dot{q} + \left[S_{rn} + 0.5 S_{rc} + a_4 \left(\frac{2V_\infty}{c}\right) T_{rc}\right] q + S_{rc} y + \left(\frac{2V_\infty}{c}\right) T_{rc} z \\ & + F_{rn} \ddot{\delta} + \left(E_{rn} + 0.5 E_{rc}\right) \dot{\delta} + \left[D_{rn} + 0.5 D_{rc} + a_4 \left(\frac{2V_\infty}{c}\right) E_{rc}\right] \delta + D_{rc} v + \left(\frac{2V_\infty}{c}\right) E_{rc} w \qquad (5.1) \end{aligned}$$

where x_r is the rigid aircraft state vector, q is the generalized displacement vector of the wing, y and z are the aerodynamic lag state vectors for the wing structural dynamics, δ_r is the rigid aircraft flight control surface deflection vector, δ is the VCCTEF deflection vector, v and w are the aerodynamic lag state vectors for the VCCTEF actuator dynamics, the upper case variables are matrices, the subscript r denotes a rigid quantity, and the subscript n and c denote non-circulatory and circulatory quantities according to the Theodorsen's theory.

For symmetric flight conditions, the rigid aircraft state vector x_r includes the altitude h, airspeed V, angle of attack α, pitch rate q, and pitch angle θ. The rigid aircraft flight control surface deflection vector δ_r includes the thrust δ_T and elevator deflection δ_e.

5.2.2. Unsteady aerodynamics

The aerodynamic lag states in Equation 5.1 account for unsteady aerodynamic effects. In general, unsteady aerodynamics are included to a steady-state aerodynamic model by adding an unsteady aerodynamic correction factor. This unsteady aerodynamic correction is provided by Theodorsen's function. Theodorsen's function describes the effect of phase lag and decrease in magnitude of circulatory lift caused by the interaction between the wake and the flow around the airfoil [27]. For incompressible flow this effect is expressed as function of the reduced frequency k of a harmoniously oscillating airfoil

$$C(k) = F(k) + iG(k) \qquad (5.2)$$

where $F(k) \geq 0.5$, $G(k) \leq 0$, and

$$k = \frac{\omega c}{2V} \qquad (5.3)$$

where ω is the oscillation frequency of the airfoil, c is the airfoil chord, and V is the free stream airspeed.

Theodorsen's function can create issues in flight dynamic modeling because of its dependency on specific frequencies of the harmonious oscillations. Because of this, the R.T. Jones approximation is used to convert the Theordorsen's function into a time-domain representation [28, 29].

The R.T. Jones approximation of Theodorsen's equation is as follows

$$C(k) \approx \hat{C}(\bar{s}) = \frac{0.5\bar{s}^2 + a_1 \bar{s} + a_2}{\bar{s}^2 + a_3 \bar{s} + a_2} \qquad (5.4)$$

where $\bar{s} = \frac{sc}{2V_\infty}$ is a dimensionless Laplace transform and $a_1 = 0.2808$, $a_2 = 0.0165$, and $a_3 = 0.3455$.

The R.T. Jones approximation makes the system frequency-independent. Furthermore, it introduces two aerodynamic lag states for every single aeroelastic state variable to approximate the effect of unsteady aerodynamics. For more information on the use of Theodorsen's function and the R.T. Jones approximation the reader is referred to the work of Tal and Nguyen on unsteady aeroservoelastic modeling for flexible wing aircraft [29].

5.2.3. Aeroelastic model

The aeroelastic model of the ESAC describes the aeroelastic modes. These aeroelastic modes describe the bending and torsion of the wing. The mode shapes of the first three symmetric aeroelastic modes are illustrated in Figure 5.3.

These modes are described using generalized coordinates q. In this model, the generalized coordinates are modal coordinates which are the orthogonal mode shapes corresponding to the eigenvalues of the system.

The aeroelastic model of the GTM flexible wing aircraft is formulated using finite-element modeling.

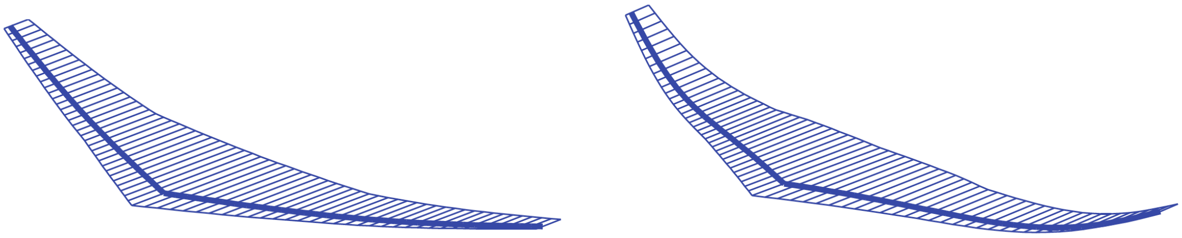

(a) First symmetric bending mode (q_1)

(b) Second symmetric bending mode (q_2)

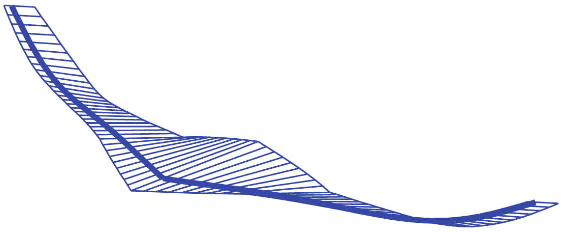

(c) First symmetric torsion mode (q_3)

Figure 5.3: First three symmetric elastic wing modes of the ESAC [28]

The aeroelastic equation of the wing structure is discretized as

$$(M_s + M_{an})\,\ddot{q} + (C_s + C_{an} + 0.5C_{ac})\,\dot{q} + \left[K_s + 0.5K_{ac} + a_4\left(\frac{2V_\infty}{c}\right)C_{ac}\right]q + K_{ac}y + \left(\frac{2V_\infty}{c}\right)C_{ac}z = Q_e\dot{x}_r + P_e x_r$$
$$+ F_{en}\ddot{\delta} + (E_{en} + 0.5E_{ec})\,\dot{\delta} + \left[D_{en} + 0.5D_{ec} + a_4\left(\frac{2V_\infty}{c}\right)E_{ec}\right]\delta + D_{ec}v + \left(\frac{2V_\infty}{c}\right)E_{ec}w \quad (5.5)$$

where the subscript s denotes a structural dynamic quantity, the subscript a denotes an aerodynamic quantity due to the unsteady aerodynamic effect, and the subscript e denotes an aeroelastic quantity associated with the wing aeroelasticity.

As mentioned, the R.T. Jones approximation introduces two aerodynamic lag state equations for each aeroelastic state equation. The lag state are defined as

$$\ddot{y} + a_3\left(\frac{2V_\infty}{c}\right)\dot{y} + a_2\left(\frac{2V_\infty}{c}\right)^2 y = a_4\left(\frac{2V_\infty}{c}\right)\dot{q} + 0.5a_2\left(\frac{2V_\infty}{c}\right)^2 q \quad (5.6)$$

$$\ddot{z} + a_3\left(\frac{2V_\infty}{c}\right)\dot{z} + a_2\left(\frac{2V_\infty}{c}\right)^2 z = a_5\left(\frac{2V_\infty}{c}\right)\dot{q} + a_6\left(\frac{2V_\infty}{c}\right)^2 q \quad (5.7)$$

5.2.4. Actuator dynamics

The ESAC contains the thrust, elevator, and VCCTEF as control inputs for the longitudinal motions. The thrust and elevator are categorized under the rigid aircraft flight control.

The actuator dynamic equation of the VCCTEF is expressed as

$$M_\delta\ddot{\delta} + C_\delta\dot{\delta} + K_\delta\delta = Q_\delta\dot{x}_r + P_\delta x_r + V_{\delta n}\ddot{q} + (T_{\delta n} + 0.5T_{\delta c})\,\dot{q} + \left[S_{\delta n} + 0.5S_{\delta c} + a_4\left(\frac{2V_\infty}{c}\right)T_{\delta c}\right]q$$
$$+ S_{\delta c}y + \left(\frac{2V_\infty}{c}\right)T_{\delta c}z + F_{\delta n}\ddot{\delta} + (E_{\delta n} + 0.5E_{\delta c})\,\dot{\delta} + \left[D_{\delta n} + 0.5D_{\delta c} + a_4\left(\frac{2V_\infty}{c}\right)E_{\delta c}\right]\delta_{+}D_{\delta c}v + \left(\frac{2V_\infty}{c}\right)E_{\delta c}w + \tau_\delta \quad (5.8)$$

where τ_δ is the motor torque.

Each VCCTEF state δ is accompanied with two aerodynamic lag state equations to approximate the effect of unsteady aerodynamics on the actuator dynamics. The lag states are expressed as

$$\ddot{v} + a_3 \left(\frac{2V_\infty}{c} \right) \dot{v} + a_2 \left(\frac{2V_\infty}{c} \right)^2 v = a_4 \left(\frac{2V_\infty}{c} \right) \dot{\delta} + 0.5 a_2 \left(\frac{2V_\infty}{c} \right)^2 \delta \tag{5.9}$$

$$\ddot{w} + a_3 \left(\frac{2V_\infty}{c} \right) \dot{w} + a_2 \left(\frac{2V_\infty}{c} \right)^2 w = a_5 \left(\frac{2V_\infty}{c} \right) \dot{\delta} + 0.5 a_6 \left(\frac{2V_\infty}{c} \right)^2 \delta \tag{5.10}$$

The actuator dynamics of the thrust and elevator are included in the rigid aircraft flight control. Their dynamics is described by a first-order model as

$$\dot{\delta}_r = -\lambda \left(\delta_r - \delta_{rc} \right) \tag{5.11}$$

where $\lambda > 0$ is the actuator rate vector and δ_{rc} is the command vector of the rigid-body aircraft control.

The servo-motor dynamics for the VCCTEF are formed by a PI+D feedback control law

$$\dot{e} = \delta - \delta_c \tag{5.12}$$

$$\tau_\delta = k_p \left(\delta - \delta_c \right) + k_i e + k_d \dot{\delta} \tag{5.13}$$

where e is the integral error of the VCCTEF deflection command δ_c.

5.2.5. Flight dynamic coupling

All the above equations are integrated into a fully coupled aeroservoelastic flight dynamic model described by Equation 5.14 [7].

$$\left[\begin{array}{c|cccccc|cccccc|cc}
M_r - Q_r & 0 & 0 & 0 & -V_{rn} & 0 & 0 & 0 & 0 & 0 & -F_{rn} & 0 & 0 & 0 & 0 \\
\hline
0 & I & 0 & 0 & 0 & 0 & 0 & 0 & 0 & 0 & 0 & 0 & 0 & 0 & 0 \\
0 & 0 & I & 0 & 0 & 0 & 0 & 0 & 0 & 0 & 0 & 0 & 0 & 0 & 0 \\
0 & 0 & 0 & I & 0 & 0 & 0 & 0 & 0 & 0 & 0 & 0 & 0 & 0 & 0 \\
-Q_e & 0 & 0 & 0 & M_s + M_{an} & 0 & 0 & 0 & 0 & 0 & -F_{en} & 0 & 0 & 0 & 0 \\
0 & 0 & 0 & 0 & 0 & I & 0 & 0 & 0 & 0 & 0 & 0 & 0 & 0 & 0 \\
0 & 0 & 0 & 0 & 0 & 0 & I & 0 & 0 & 0 & 0 & 0 & 0 & 0 & 0 \\
\hline
0 & 0 & 0 & 0 & 0 & 0 & 0 & I & 0 & 0 & 0 & 0 & 0 & 0 & 0 \\
0 & 0 & 0 & 0 & 0 & 0 & 0 & 0 & I & 0 & 0 & 0 & 0 & 0 & 0 \\
0 & 0 & 0 & 0 & 0 & 0 & 0 & 0 & 0 & I & 0 & 0 & 0 & 0 & 0 \\
-Q_\delta & 0 & 0 & 0 & -V_{\delta n} & 0 & 0 & 0 & 0 & 0 & M_\delta - F_{\delta n} & 0 & 0 & 0 & 0 \\
0 & 0 & 0 & 0 & 0 & 0 & 0 & 0 & 0 & 0 & 0 & I & 0 & 0 & 0 \\
0 & 0 & 0 & 0 & 0 & 0 & 0 & 0 & 0 & 0 & 0 & 0 & I & 0 & 0 \\
\hline
0 & 0 & 0 & 0 & 0 & 0 & 0 & 0 & 0 & 0 & 0 & 0 & 0 & I & 0 \\
0 & 0 & 0 & 0 & 0 & 0 & 0 & 0 & 0 & 0 & 0 & 0 & 0 & 0 & I
\end{array}\right]
\left[\begin{array}{c}
\dot{x}_r \\
\hline
\dot{q} \\
\dot{y} \\
\dot{z} \\
\ddot{q} \\
\ddot{y} \\
\ddot{z} \\
\hline
\dot{\delta} \\
\dot{v} \\
\dot{w} \\
\ddot{\delta} \\
\ddot{v} \\
\ddot{w} \\
\hline
\dot{\delta}_r \\
\dot{e}
\end{array}\right] =$$

$$
\left[\begin{array}{c|cccccc}
P_r & S_{rn}+0.5S_{rc}+a_4\left(\frac{2V_\infty}{c}\right)T_{rc} & S_{rc} & \left(\frac{2V_\infty}{c}\right)T_{rc} & T_{rn}+0.5T_{rc} & 0 & 0 \\
\hline
0 & 0 & 0 & 0 & I & 0 & 0 \\
0 & 0 & 0 & 0 & 0 & I & 0 \\
0 & 0 & 0 & 0 & 0 & 0 & I \\
P_e & -\left[K_s+0.5K_{ac}+a_4\left(\frac{2V_\infty}{c}\right)C_{ac}\right] & -K_{ac} & -\left(\frac{2V_\infty}{c}\right)C_{ac} & -\left(C_s+C_{an}+0.5C_{ac}\right) & 0 & 0 \\
0 & 0.5a_2\left(\frac{2V_\infty}{c}\right)^2 & -a_2\left(\frac{2V_\infty}{c}\right)^2 & 0 & a_4\left(\frac{2V_\infty}{c}\right) & -a_3\left(\frac{2V_\infty}{c}\right) & 0 \\
0 & a_6\left(\frac{2V_\infty}{c}\right)^2 & 0 & -a_2\left(\frac{2V_\infty}{c}\right)^2 & a_5\left(\frac{2V_\infty}{c}\right) & 0 & -a_3\left(\frac{2V_\infty}{c}\right) \\
\hline
0 & 0 & 0 & 0 & 0 & 0 & 0 \\
0 & 0 & 0 & 0 & 0 & 0 & 0 \\
0 & 0 & 0 & 0 & 0 & 0 & 0 \\
P_\delta & S_{\delta n}+0.5S_{\delta c}+a_4\left(\frac{2V_\infty}{c}\right)T_{\delta c} & S_{\delta c} & \left(\frac{2V_\infty}{c}\right)T_{\delta c} & T_{\delta n}+0.5T_{\delta c} & 0 & 0 \\
0 & 0 & 0 & 0 & 0 & 0 & 0 \\
0 & 0 & 0 & 0 & 0 & 0 & 0 \\
\hline
0 & 0 & 0 & 0 & 0 & 0 & 0 \\
0 & 0 & 0 & 0 & 0 & 0 & 0
\end{array}\right|
$$

$$
\left|\begin{array}{cccc|cc}
D_{rn}+0.5D_{rc}+a_4\left(\frac{2V_\infty}{c}\right)E_{rc} & D_{rc} & \left(\frac{2V_\infty}{c}\right)E_{rc} & E_{rn}+0.5E_{rc} & 0 & 0 \\
\hline
0 & 0 & 0 & 0 & 0 & 0 \\
0 & 0 & 0 & 0 & 0 & 0 \\
0 & 0 & 0 & 0 & 0 & 0 \\
D_{en}+0.5D_{ec}+a_4\left(\frac{2V_\infty}{c}\right)E_{ec} & D_{ec} & \left(\frac{2V_\infty}{c}\right)E_{rc} & E_{rn}+0.5E_{ec} & 0 & 0 \\
0 & 0 & 0 & 0 & 0 & 0 \\
0 & 0 & 0 & 0 & 0 & 0 \\
\hline
0 & 0 & 0 & I & 0 & 0 \\
0 & 0 & 0 & 0 & I & 0 \\
0 & 0 & 0 & 0 & 0 & I \\
-K_\delta+D_{\delta n}+0.5D_{\delta c}+a_4\left(\frac{2V_\infty}{c}\right)E_{\delta c}+k_p & D_{\delta c} & \left(\frac{2V_\infty}{c}\right)E_{ec} & -C_\delta+E_{\delta n}+0.5E_{\delta c}+k_d & 0 & 0 \\
0.5a_2\left(\frac{2V_\infty}{c}\right)^2 & -a_2\left(\frac{2V_\infty}{c}\right)^2 & 0 & a_4\left(\frac{2V_\infty}{c}\right) & -a3\left(\frac{2V_\infty}{c}\right) & 0 \\
a_6\left(\frac{2V_\infty}{c}\right)^2 & 0 & -a_2\left(\frac{2V_\infty}{c}\right)^2 & a_5\left(\frac{2V_\infty}{c}\right) & 0 & -a_3\left(\frac{2V_\infty}{c}\right) \\
\hline
0 & 0 & 0 & 0 & 0 & 0 \\
I & 0 & 0 & 0 & 0 & 0
\end{array}\right|
$$

$$
\left|\begin{array}{cc}
D_r & 0 \\
\hline
0 & 0 \\
0 & 0 \\
0 & 0 \\
0 & 0 \\
0 & 0 \\
0 & 0 \\
\hline
0 & 0 \\
0 & 0 \\
0 & 0 \\
0 & k_i \\
0 & 0 \\
0 & 0 \\
\hline
-\lambda & 0 \\
0 & 0
\end{array}\right]
\left[\begin{array}{c}
x_r \\
\hline
q \\
y \\
z \\
\dot{q} \\
\dot{y} \\
\dot{z} \\
\hline
\delta \\
v \\
w \\
\dot{\delta} \\
\dot{v} \\
\dot{w} \\
\hline
\delta_r \\
e
\end{array}\right]
+
\left[\begin{array}{cc}
0 & 0 \\
\hline
0 & 0 \\
0 & 0 \\
0 & 0 \\
0 & 0 \\
0 & 0 \\
0 & 0 \\
\hline
0 & 0 \\
0 & 0 \\
0 & 0 \\
0 & -k_p \\
0 & 0 \\
0 & 0 \\
\hline
\lambda & 0 \\
0 & -I
\end{array}\right]
\left[\begin{array}{c}
\delta_{rc} \\
\delta_c
\end{array}\right]
\quad (5.14)
$$

Now, let $x_r = \begin{bmatrix} h & V & \alpha & q & \theta \end{bmatrix}^T$, $x_e = \begin{bmatrix} q & y & z & \dot{q} & \dot{y} & \dot{z} \end{bmatrix}^T$, $x_\delta = \begin{bmatrix} \delta & v & w & \dot{\delta} & \dot{v} & \dot{w} \end{bmatrix}^T$, $x_s = \begin{bmatrix} \delta_r & e \end{bmatrix}^T$, and $u = \begin{bmatrix} \delta_{rc} & \delta_c \end{bmatrix}^T$. Then, Equation 5.14 can be written as

$$\begin{bmatrix} M_{rr} & M_{re} & M_{r\delta} & M_{rs} \\ M_{er} & M_{ee} & M_{e\delta} & M_{es} \\ M_{\delta r} & M_{\delta e} & M_{\delta\delta} & M_{\delta s} \\ M_{sr} & M_{se} & M_{s\delta} & M_{ss} \end{bmatrix} \begin{bmatrix} \dot{x}_r \\ \dot{x}_e \\ \dot{x}_\delta \\ \dot{x}_s \end{bmatrix} = \begin{bmatrix} S_{rr} & S_{re} & S_{r\delta} & S_{rs} \\ S_{er} & S_{ee} & S_{e\delta} & S_{es} \\ S_{\delta r} & S_{\delta e} & S_{\delta\delta} & S_{\delta s} \\ S_{sr} & S_{se} & S_{s\delta} & S_{ss} \end{bmatrix} \begin{bmatrix} x_r \\ x_e \\ x_\delta \\ x_s \end{bmatrix} + \begin{bmatrix} T_r \\ T_e \\ T_\delta \\ T_s \end{bmatrix} u \tag{5.15}$$

This dynamic model under gust excitation can be rewritten as

$$\dot{x} = Ax + Bu + w_g \tag{5.16}$$

where $x = \begin{bmatrix} x_r & x_e & x_\delta & x_s \end{bmatrix}^T$ and

$$A = \begin{bmatrix} M_{rr} & M_{re} & M_{r\delta} & M_{rs} \\ M_{er} & M_{ee} & M_{e\delta} & M_{es} \\ M_{\delta r} & M_{\delta e} & M_{\delta\delta} & M_{\delta s} \\ M_{sr} & M_{se} & M_{s\delta} & M_{ss} \end{bmatrix}^{-1} \begin{bmatrix} S_{rr} & S_{re} & S_{r\delta} & S_{rs} \\ S_{er} & S_{ee} & S_{e\delta} & S_{es} \\ S_{\delta r} & S_{\delta e} & S_{\delta\delta} & S_{\delta s} \\ S_{sr} & S_{se} & S_{s\delta} & S_{ss} \end{bmatrix} \tag{5.17}$$

$$B = \begin{bmatrix} M_{rr} & M_{re} & M_{r\delta} & M_{rs} \\ M_{er} & M_{ee} & M_{e\delta} & M_{es} \\ M_{\delta r} & M_{\delta e} & M_{\delta\delta} & M_{\delta s} \\ M_{sr} & M_{se} & M_{s\delta} & M_{ss} \end{bmatrix}^{-1} \begin{bmatrix} T_r \\ T_e \\ T_\delta \\ T_s \end{bmatrix} \tag{5.18}$$

The definitions of the mass M, stiffness S, and control T matrices in Equations 5.17 and 5.18 can be found in Appendix A.

The aeroservoelastic state-space model contains five rigid-body states in longitudinal direction, 198 aeroelastic modes with two elastic states and four aerodynamic lag states per mode, two rigid aircraft flight inputs; namely the engine throttle and elevator each with one actuator state, and 16 VCCTEF inputs to the outermost chordwise flap segments with two actuator states and four aerodynamic lag states per flap segment. Thus, the model has 1307 states and 18 control variables.

5.3. Model reduction

A reduced-order model is built for the convenience of controller design. In general, an ASE state-space model contains rigid-body modes which usually have low frequencies and aeroelastic modes which are at higher frequencies than the rigid-body modes. In control design it is sufficient to only consider the aeroelastic modes that are at the lower frequency range. This is because the high-frequency modes attenuate fast, and therefore have small response magnitudes. A reduced-order model is designed for control design purposes by only considering the low-frequency aeroelastic modes. For this reduced-order model, the first lowest 10 frequency modes including their lag states are retained. This results in a reduced-order model with 178 states and 18 control variables.

5.4. Actuator characteristics & VCCTEF virtual control

Normally, the Generic Transport Model would include all conventional control surfaces, namely the elevators, ailerons, and rudder. With the integration of the VCCTEF on the wings, the ailerons are omitted and replaced by the VCCTEF. An overview of the actuator characteristics is given in Table 5.2.

Table 5.2: Thrust and control surface characteristics

Control	Minimum Limit	Maximum Limit	Bandwidth
δ	-20 deg	20 deg	50 Hz
δ_e	-25 deg	25 deg	5 Hz
δ_r	-30 deg	30 deg	5Hz
δ_T	1000 lbs	40000 lbs	-

The elastomer material between the spanwise flap sections of the VCCTEF limits the relative motion between these sections. The elastomer material has certain displacement and rate limits, and consequently the flap sections are also constrained by relative displacement and rate limits. The relative constraints between the spanwise flap sections need to be included in the control design.

The constraints can be expressed as

$$|\delta_{i+1} - \delta_i| \leq \dot{\delta} \tag{5.19}$$

$$\left|\dot{\delta}_{i+1} - \dot{\delta}_i\right| \leq \Delta\dot{\delta} \tag{5.20}$$

where $i = 1, 2, \ldots, m$ is the index of each flap section and m is the number of spanwise flap sections of the VCCTEF per wing.

The displacement constraint between each adjacent spanwise flap section for the VCCTEF is 2°. The rate constraint is not defined and therefore not considered in this study.

The relative deflection limit is addressed in the control design by implementing virtual control [30]. The deflections of the flap sections are constrained to a mathematical shape function. The actual flap deflections can now be described by a set of virtual control variables. In this study, the spanwise flap sections are constrained to a shape function of a cubic Chebyshev polynomial of the first kind, as

$$\delta_i = c_0 + c_1 k + c_2\left(2k^2 - 1\right) + c_3\left(4k^3 - 3k\right) \tag{5.21}$$

where $k = \frac{i-1}{n-1}$, $i = 1, 2, \ldots, n$, $n = 16$, and c_j, $j = 0, 1, 2, 3$ are the virtual control variables.

The control design determines the commands for the virtual control variables with the implementation of this shape function. Since the shape function in Equation 5.21 is linear with respect to the virtual control variables, a transformation matrix can be constructed that relates the physical control variables to the virtual control variables with the use of partial derivation.

5.5. Aerodynamic, structural and dynamic model parameters

In this study, the aircraft drag, wing root bending moment and vertical acceleration at the center of gravity are used in the multi-objective control formulation or to assess the controller performance.

The drag minimization control is evaluated by comparing the results of different controllers with respect to the incremental drag. The aircraft drag coefficient can be estimated via a drag polar model, as

$$C_D = C_{D_0} + \left(C_{L_0} + C_{L_{\dot{x}}}\dot{x} + C_{L_x}x + C_{L_u}u\right)^T K \left(C_{L_0} + C_{L_{\dot{x}}}\dot{x} + C_{L_x}x + C_{L_u}u\right) \tag{5.22}$$

where K contains the drag polar parameters, C_{D_0} is the zero-lift drag coefficient, C_{L_0} is the trim state lift coefficient, C_{L_x} and $C_{L_{\dot{x}}}$ contain the lift stability and control derivatives and C_{L_u} contains the lift derivatives with respect to the control inputs.

This results in a definition for the incremental drag as

$$\Delta C_D = C_{D_x}x + C_{D_u}u + x^T C_{D_{x^2}}x + x^T C_{D_{xu}}u + u^T C_{D_{u^2}}u \tag{5.23}$$

The wing root bending moment is used to evaluate the active gust load alleviation control. The wing root bending moment is expressed in general as

$$M_y = M_x x + M_u u + M_w w_g \tag{5.24}$$

where $M_w w_g$ is a bending moment component due to the gust disturbance.

A performance metric based on the vertical acceleration at the aircraft center of gravity is also used to evaluate the active gust load alleviation control. The vertical acceleration at the aircraft center of gravity A_z is defined as

$$A_z = \frac{-Z}{m} \tag{5.25}$$

where Z is the downward vertical force and m is the aircraft mass. This definition can be expressed as

$$A_z = -V\dot{\alpha} - \dot{V}\alpha + qV + g\cos\theta \tag{5.26}$$

where V is the aircraft velocity, α is the angle of attack, q is the pitch rate, g is the local gravitational field of the Earth, and θ is the pitch angle. Because the term corresponding to the gravitational constants is approximately constant ($g\cos\theta \approx 0$), the incremental vertical acceleration of the aircraft center of gravity ΔA_z is used as a performance metric to evaluate the gust load alleviation controller

$$\Delta A_z = -V\dot{\alpha} - \dot{V}\alpha + qV \tag{5.27}$$

6

Turbulence Model

The active gust load alleviation control method will be evaluated and validated using turbulence models.

The turbulence model will produce a local turbulence velocity. This local turbulence velocity affects the local angle of attack and therefore also the lift distribution along the wing. The lift distribution directly impacts the aeroelastic response of the aircraft.

The most used continuous turbulence models are the von Kármán and Dryden spectra. Both models define the linear and angular velocity components of the continuous gusts as spatially varying stochastic processes. The main difference between the models is that the von Kármán model uses irrational power spectral densities to define the linear and angular velocity components while the Dryden model uses rational power spectral densities.

The von Kármán model contains a large share of high-frequency turbulence and therefore is an excellent model for the simulations of aeroelastic phenomena. In this study, we use a severe 1D von Kármán turbulence model, illustrated in Figure 6.1.

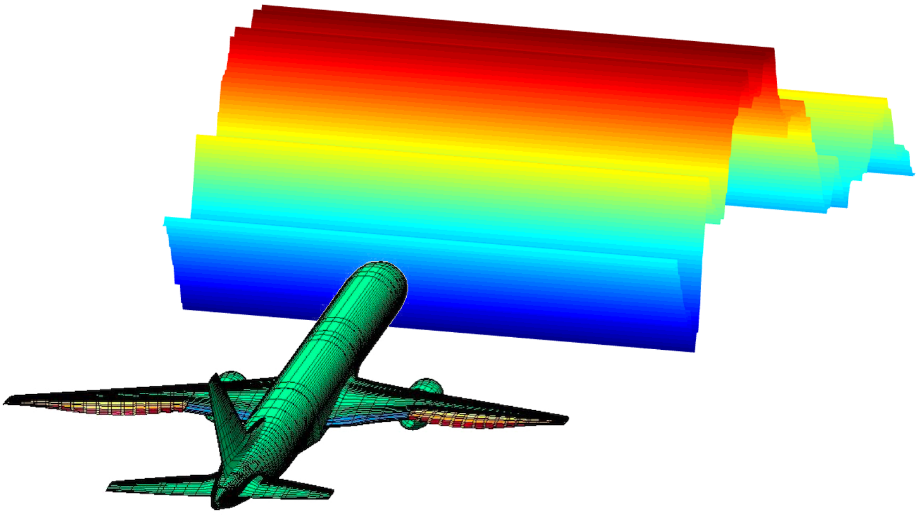

Figure 6.1: 1D severe von Kármán turbulence field

In addition to the evaluation of the controller for this severe 1D von Kármán turbulence model, the active gust load alleviation controller will be validated for several Dryden and von Kármán turbulence models with various severity.

The differential equations of the vertical gust velocity for the von Kármán and Dryden turbulence models are presented below. Furthermore, the effect of turbulence on the aerodynamic loads is discussed. The theory that is presented below is based on the work of the Advanced Control and Evolvable Systems group at NASA Ames Research Center.

6.1. von Kármán turbulence model

The von Kármán turbulence transfer function for the vertical gust velocity w_g is given by

$$H(s) = \sigma \frac{L}{\pi V_\infty} \frac{1 + 2.7478 \frac{L}{V_\infty} s + 0.3398 \frac{L^2}{V_\infty^2} s^2}{1 + 2.9968 \frac{L}{V_\infty} s + 1.97545 \frac{L^2}{V_\infty^2} s^2 + 0.1539 \frac{L^3}{V_\infty^3} s^3} \tag{6.1}$$

where σ is the turbulence intensity, L is the characteristic length, and V is the airspeed.

The turbulence intensity is given by

$$\sigma = 0.1 w_{20} \tag{6.2}$$

where w_{20} is the wind speed at an altitude of 20 ft and is equal to 15 knots for light turbulence, 30 knots for moderate turbulence, and 45 knots for severe turbulence. The characteristic length at an altitude above 2000ft is equal to $L = 1750 ft$.

The differential equation for the von Kármán turbulence model is

$$\ddot{w}_g + 12.8356 \frac{V_\infty}{L} \ddot{w}_g + 19.4659 \frac{V_\infty^2}{L^2} \dot{w}_g + 6.4977 \frac{V_\infty^3}{L^3} w_g = 6.4977 \sigma \frac{V_\infty^2}{L^2} w_{in} + 17.85445 \sigma \frac{V_\infty}{L} \sqrt{\frac{V_\infty}{\pi L}} \dot{w}_{in} + 2.2079 \sqrt{\frac{V_\infty}{\pi L}} \ddot{w}_{in} \tag{6.3}$$

where w_{in} is a white noise signal which can be scaled to give a desired amplitude for the turbulence case.

6.2. Dryden turbulence model

The Dryden turbulence model for the vertical velocity component is given by the power spectrum density function according to MIL-F-8785C

$$\Phi(\omega) = |H(\omega)|^2 = \sigma^2 \frac{L}{\pi V_\infty} \frac{1 + 3\left(\frac{L\omega}{V_\infty}\right)^2}{\left[1 + \left(\frac{L\omega}{V_\infty}\right)^2\right]^2} \tag{6.4}$$

where ω is the frequency of the spectrum.

The response of the vertical gust velocity to a white noise signal is computed from the transfer function $H(\omega)$ as follows

$$\frac{w_g}{w_{in}} = \sigma \sqrt{\frac{L}{\pi V_\infty}} \frac{1 + \sqrt{3}\left(\frac{L}{V_\infty}\right) j\omega}{\left[1 + \left(\left(\frac{Lj\omega}{V_\infty}\right)\right)\right]^2} \tag{6.5}$$

Now let $s = j\omega$. Then

$$\frac{w_g}{w_{in}} = \sigma \sqrt{\frac{L}{\pi V_\infty}} \frac{1 + \sqrt{3}\left(\frac{L}{V_\infty}\right) s}{\left[1 + \left(\left(\frac{L}{V_\infty}\right) s\right)\right]^2} \tag{6.6}$$

The differential equation for the Dryden turbulence model is given by

$$\ddot{w}_g + 2\frac{V_\infty}{L} \dot{w}_g + \frac{V_\infty^2}{L^2} w_g = \sigma \frac{V_\infty}{L} \sqrt{\frac{V_\infty}{\pi L}} w_{in} + \sigma \sqrt{\frac{3V_\infty}{\pi L}} \dot{w}_{in} \tag{6.7}$$

6.3. Incompressible unsteady turbulence response

The effect of the vertical gust velocity w_g, calculated by Equations 6.3 or 6.7, on the aerodynamic forces and moments can be calculated using Küssner's unsteady gust response function [31] .

The R.T. Jones' approximation of the incompressible Küssner's function is given in the time-domain as [32]

$$\psi(\tau) = 1 - 0.500e^{-0.130\tau} - 0.500e^{-\tau} \tag{6.8}$$

Let $\bar{s} = \frac{sc}{2V_\infty}$, then the frequency domain representation of R.T. Jones' approximation is expressed as

$$\psi(\bar{s}) = 1 - \frac{0.500\bar{s}}{\bar{s} + 0.130} - \frac{0.500\bar{s}}{\bar{s} + 1} \tag{6.9}$$

This expression can be rewritten as

$$\psi(\bar{s}) = 1 - \frac{a_1\bar{s} + a_2}{\bar{s}^2 + a_3\bar{s} + a_2} \tag{6.10}$$

where $a_1 = 0.565$, $a_2 = 0.130$, and $a_3 = 1.13$.

The asymptotic values of the Küssner's function are $\psi(\tau = 0) = \psi(\bar{s} \to \infty) = 0$ and $\psi(\tau = \infty) = \psi(\bar{s} = 0) = 1$. Let $y = \alpha_g(t)\psi(\bar{s})$. Then y is computed from the following differential equation

$$\ddot{y} + a_3\left(\frac{2V_\infty}{c}\right)\dot{y} + a_2\left(\frac{2V_\infty}{c}\right)^2 y = a_1\left(\frac{2V_\infty}{c}\right)\dot{\alpha}_g + a_2\left(\frac{2V_\infty}{c}\right)^2 \alpha_g \tag{6.11}$$

The instantaneous angle of attack due to gust on a wing section is approximated with linear potential flow theory as

$$\alpha_g(t) = \frac{1}{\pi}\int_0^\pi \frac{w_g}{V_\infty}\left(t - \frac{x_p}{V_\infty}\right)(1 - \cos\theta)\, d\theta \tag{6.12}$$

where $\theta = \cos^{-1}\left(1 - 2\frac{x}{c}\right)$.

Then, the unsteady sectional lift, drag, and pitching moment coefficients can be computed as

$$c_{L_g}(t) = c_{L_\alpha} y(t) \tag{6.13}$$

$$c_{D_g}(t) = K\left(c_{L_\alpha} y(t)\right)^2 \tag{6.14}$$

$$c_{m_g}(t) = \frac{e}{c}\left(c_{L_\alpha} y(t)\right) \tag{6.15}$$

where

$$K = \frac{c_{D_\alpha}/c_{L_\alpha}}{2C_L} \tag{6.16}$$

The sectional loads of each wing can then be integrated across the half-span to compute the gust induced loads on the left wing as

$$L_{g_{wl}}(t) = q_\infty \int_0^{\frac{b}{2}} c_{L_g}(t) c\, dX \tag{6.17}$$

$$D_{g_{wl}}(t) = q_\infty \int_0^{\frac{b}{2}} c_{D_g}(t) c\, dX \tag{6.18}$$

$$m_{g_{wl}}(t) = q_\infty \int_0^{\frac{b}{2}} \left(-x_{ac} c_{L_g}(t) + z_{ac} c_{D_g}(t)\right) c\, dx \tag{6.19}$$

Finally, the total instantaneous gust load for the aircraft is the sum of the gust induced loads for the wings and horizontal tailplane.

$$L_g = L_{g_{wl}} + L_{g_{wr}} + L_{g_{hl}} + L_{g_{hr}} \tag{6.20}$$

$$D_g = D_{g_{wl}} + D_{g_{wr}} + D_{g_{hl}} + D_{g_{hr}} \tag{6.21}$$

$$m_g = m_{g_{wl}} + m_{g_{wr}} + m_{g_{hl}} + m_{g_{hr}} \tag{6.22}$$

III

Control Design

7

Multi-Objective Optimal Control

This chapter describes the multi-objective flight control design. First, an altitude-hold control mode will be designed by using flight path angle control. Secondly, a nominal rigid controller will be designed. The nominal rigid controller is built for the evaluation of the multi-objective flight controller with active gust load alleviation. The performance of the two controllers will be compared. Next, the multi-objective flight control design will be derived. The multi-objective flight controller will contain the aeroelastic mode suppression and drag reduction objectives. Finally, the topic of aeroelastic state estimation will be discussed.

7.1. Linear-Quadratic Gaussian control

The nominal rigid controller and multi-objective flight controller are built using Linear-Quadratic Gaussian (LQG) control. LQG control is widely used for optimal control problems and provides a unique solution for specified weight matrices. Advantages of LQG are the easy computation and implementation of this control method. The LQG controller is a combination of a state observer and a Linear-Quadratic Regulator (LQR). The separation principle guarantees that these elements can be designed and computed independently.

Optimal control design strives to minimize a cost function for a dynamic system. In the case of Linear-Quadratic control the cost function is quadratic and the system dynamics are described by linear differential equations.

An overview of the LQG control method is illustrated in Figure 7.1. The controller is an LQ Regulator. The rigid-body x_r, VCCTEF x_δ, and servo x_s states are measured by the Inertial Measurement Unit (IMU) and gyros. The accelerometers measure the vertical accelerations at specific wing locations. The accelerometers output is used for the Kalman Filter state estimation which estimates the aeroelastic states.

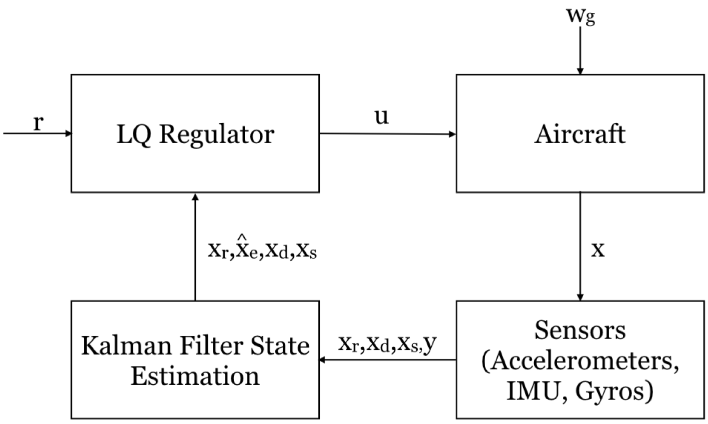

Figure 7.1: Linear-Quadratic Gaussian control

7.2. Flight path angle control

The flight controller is designed to provide an altitude-hold mode by following a flight path angle command. The altitude-hold mode is included in the control system by defining an augmented state x_a in the state-space system of the reduced-order model. The augmented state is defined as an integral error state of the flight path angle

$$x_a = \int_0^t \Delta\gamma d\tau \tag{7.1}$$

where the error between the flight path angle and the command signal is expressed as

$$\Delta\gamma = \theta - \alpha - \gamma_c = A_a x_r - \gamma_c \tag{7.2}$$

in which γ_c is the commanded flight path angle.

Including the flight path angle command into the reduced-order version of the state-space system in Equation 5.16 results in

$$\dot{x} = Ax + Bu + z + w_g \tag{7.3}$$

where

$$x = \begin{bmatrix} x_r \\ x_e \\ x_\delta \\ x_s \\ x_a \end{bmatrix} \quad A = \begin{bmatrix} A_{rr} & A_{re} & A_{r\delta} & A_{rs} & 0 \\ A_{er} & A_{ee} & A_{e\delta} & A_{es} & 0 \\ A_{\delta r} & A_{\delta e} & A_{\delta\delta} & A_{\delta s} & 0 \\ A_{sr} & A_{se} & A_{s\delta} & A_{ss} & 0 \\ A_a & 0 & 0 & 0 & 0 \end{bmatrix}, B = \begin{bmatrix} B_{rr} & B_{re} \\ B_{er} & B_{ee} \\ B_{\delta r} & B_{\delta e} \\ B_{sr} & B_{se} \\ 0 & 0 \end{bmatrix} \quad z = \begin{bmatrix} 0 \\ 0 \\ 0 \\ 0 \\ -\gamma_c \end{bmatrix} \tag{7.4}$$

This ASE state-space model can be rewritten as

$$\dot{x}_r = A_{rr}x_r + A_{re}x_e + B_{rr}u_r + B_{re}u_e + z_r + w_r \tag{7.5}$$

$$\dot{x}_e = A_{er}x_r + A_{ee}x_e + B_{er}u_r + B_{ee}u_e + z_e + w_e \tag{7.6}$$

where x_r is the rigid-body state vector that includes the actuator state vector of the VCCTEF and the servo-motor state vector, x_e is the elastic state vector including aerodynamic lag states, u_r is the rigid aircraft control input vector, u_e is the VCCTEF control input vector, z_r is the command vector to the rigid aircraft state, z_e is the command vector to the elastic state, w_r is the disturbance to the rigid aircraft state, and w_e is the disturbance to the elastic state.

7.3. Optimal cost function formulation

A quadratic cost function for the optimal control problem of the nominal rigid controller and the multi-objective flight controller can be defined in two segments

$$J = J_r + J_e \tag{7.7}$$

where

$$J_r = \lim_{t_f \to \infty} \frac{1}{2} \int_0^{t_f} \left[x_r^T Q_r x_r + u_r^T R_r u_r \right] dt \tag{7.8}$$

$$J_e = \lim_{t_f \to \infty} \frac{1}{2} \int_0^{t_f} \left[x_e^T Q_e x_e + u_e^T R_e u_e + q_D \Delta C_D \right] dt \tag{7.9}$$

The rigid aircraft controller u_r can be designed based on the cost function J_r to enable a rigid aircraft state $x_a = Fx_r$ to track a command signal z. In this study, the VCCTEF controller u_e is designed based on the total cost function J to provide drag minimization and aeroelastic mode suppression.

7.4. Nominal rigid control

A nominal rigid aircraft controller is designed to validate the performance of the multi-objective flight controller with active gust load alleviation.

The design of the nominal rigid aircraft controller (NRC) is derived by formulating the Hamiltonian function of the cost function for the nominal rigid aircraft dynamics in Equation 7.8

$$H = \frac{1}{2}\left(x_r^T Q_r x_r + u_r R_r u_r\right) + \lambda^T \left(A_{rr} x_r + B_r u_r\right) \tag{7.10}$$

where λ is the adjoint variable.

The adjoint equation and optimal control are obtained as

$$\dot{\lambda} = -\frac{\partial H^T}{\partial x_r} = -Q_r x_r - A_{rr}^T \lambda \tag{7.11}$$

$$\frac{\partial H^T}{\partial u_r} = R_r u_r + B_r^T \lambda = 0 \Rightarrow u_r = -R_r B_r^T \lambda \tag{7.12}$$

The adjoint variable is assumed to be defined as $\lambda = P x_r + S z_r$. Inserting this definition into the adjoint equation gives

$$\dot{P} x_r + P \dot{x}_r + \dot{S} z_r + S \dot{z}_r = -Q_r x_r - A_{rr}^T \left(P x_r + S z_r\right) \tag{7.13}$$

For the infinite time-horizon optimal control, the solution will approach a steady-state solution. Therefore, $\dot{P} = 0$ and $\dot{S} = 0$. Separating the terms of Equation 7.13 gives

$$P A_{rr} + A_{rr}^T P - P B_r R_r^{-1} B_r^T P + Q_r = 0 \tag{7.14}$$

$$S = -\left(A_{rr}^T - P B_r R_r^{-1} B_r^T\right)^{-1} P \tag{7.15}$$

where Equation 7.14 is the algebraic Ricatti equation.

Finally, the nominal rigid aircraft controller is given by

$$u_r = K_{x_r} x_r + K_z z_r \tag{7.16}$$

where

$$K_{x_r} = -R_r B_r^T P \tag{7.17}$$

$$K_{z_r} = -R_r B_r^T S \tag{7.18}$$

7.5. Multi-objective flight control

The multi-objective flight controller is designed to not only provide pilot command-following control but also include aeroelastic mode suppression and drag minimization. The controller is build using the quadratic optimal control cost function of Equation 7.7. Inserting the individual elements of the state-vector x gives

$$J = \frac{1}{2}\int_0^{t_f} \left(x_r^T Q_r x_r + x_e^T Q_e x_e + x_\delta^T Q_\delta x_\delta + x_s^T Q_s x_s + x_a^T Q_a x_a + u^T R u + q_D \Delta C_D\right) dt \tag{7.19}$$

7.5.1. Control objectives within optimal control cost function

The aeroelastic mode suppression objective is implemented in the quadratic cost function of Equation 7.19 by defining the gain matrix Q_e with respect to the aeroelastic states x_e.

Drag minimization is included in the cost function by the term $q_D \Delta C_D$. The selection of the drag penalty q_D weights the influence the drag minimization objective has on the total control.

7.5.2. Control implementation

To build the multi-objective flight control, the cost function J in Equation 7.19 is used. We formulate the Hamiltonian of the total cost function J as

$$H = \frac{1}{2}\left(x^T Q x + u^T R u + q_D \Delta C_D\right) + \lambda^T (Ax + Bu + z) \tag{7.20}$$

Inserting the definition of the incremental drag described by Equation 5.23 in the Hamiltonian gives

$$H = \frac{1}{2} x^T Q x + \frac{1}{2} u^T R u + \frac{1}{2} q_D \left(C_{D_x} x + C_{D_u} u + x^T C_{D_{x^2}} x + x^T C_{D_{xu}} u + u^T C_{D_{u^2}} u \right) + \lambda^T (Ax + Bu + z) \tag{7.21}$$

The adjoint equation and optimal control are obtained as

$$\dot{\lambda} = -\frac{\partial H^T}{\partial x} = -Qx - \frac{1}{2} q_D \left(C_{D_x}^T + 2 C_{D_{x^2}}^T x + C_{D_{xu}}^T u \right) - A^T \lambda \tag{7.22}$$

$$\begin{aligned} \frac{\partial H^T}{\partial u} &= Ru + \frac{1}{2} q_D \left(C_{D_u}^T + C_{D_{xu}}^T x + 2 C_{D_{u^2}}^T u \right) + B^T \lambda = 0 \Rightarrow \\ u &= -\left(R + q_D C_{D_{u^2}}^T \right)^{-1} \left(B^T \lambda + \frac{1}{2} q_D C_{D_u}^T + \frac{1}{2} q_D C_{D_{xu}}^T x \right) \end{aligned} \tag{7.23}$$

The adjoint, state, and optimal control equations need to be solved simultaneously. Let $\lambda = Wx + Vz + \lambda_0$ be a solution of the adjoint vector. Then, Equation 7.22 becomes

$$\dot{W} x + W \dot{x} + \dot{V} z + V \dot{z} = -Qx - \frac{1}{2} q_D \left(C_{D_x}^T + 2 C_{D_{x^2}}^T x + C_{D_{xu}}^T u \right) - A^T (Wx + Vz + \lambda_0) \tag{7.24}$$

Let γ_c be constant so that $\dot{\gamma}_c = 0$. Let $t_f \to \infty$, then the optimal solution approaches a steady-state solution. Therefore, $\dot{W}(t_f) = 0$ and $\dot{V}(t_f) = 0$.

The state-space system without gust excitation is defined as

$$\dot{x} = Ax + Bu + z \tag{7.25}$$

Inserting this definition into Equation 7.24 and separating terms yields the following expressions

$$W \bar{A} + \bar{A}^T W - W B \bar{R}^{-1} B^T W + \bar{Q} = 0 \tag{7.26}$$

$$V = -\left(\bar{A}^T - W B \bar{R}^{-1} B^T \right)^{-1} W \tag{7.27}$$

$$\lambda_0 = -\left(\bar{A}^T - W B \bar{R}^{-1} B^T \right)^{-1} \left(\frac{1}{2} q_D C_{D_x} \right) \tag{7.28}$$

where

$$\bar{R} = R + q_D C_{D_{u^2}}^T \tag{7.29}$$

$$\bar{A} = A - \frac{1}{2} q_D B \bar{R}^{-1} C_{D_{xu}}^T \tag{7.30}$$

$$\bar{Q} = Q + q_D C_{D_{x^2}}^T - \left(\frac{1}{2} q_D C_{D_{xu}}^T \right)^T \bar{R}^{-1} \left(\frac{1}{2} q_D C_{D_{xu}}^T \right) \tag{7.31}$$

Since $Q > 0, q_D > 0, C_{D_{x^2}} > 0$, and $C_{D_{xu}} > 0$ it follows that $\bar{Q} > 0$. Note that Equation 7.26 is a Ricatti equation and thus can be solved algebraically.

The multi-objective flight controller is expressed as

$$u = K_x x + K_z z + \Lambda_0 \tag{7.32}$$

where

$$K_x = -\bar{R}^{-1}\left(B^T W + \frac{1}{2} q_D C_{D_{xu}}^T\right) \tag{7.33}$$

$$K_z = -\bar{R}^{-1} B^T V \tag{7.34}$$

$$\Lambda_0 = -\bar{R}^{-1}\left(B^T \lambda_0 + \frac{1}{2} q_D C_{D_u}^T\right) \tag{7.35}$$

7.6. Aeroelastic state estimation

The multi-objective flight controller with active gust load alleviation is a feedback control design. This means that the control design needs information about the states. In this study, it is assumed that the rigid-body states x_r, VCCTEF states x_δ, and servo-motor states x_s can be measured. The aeroelastic state vector x_e cannot be measured and therefore needs to be estimated with an observer design.

The inclusion of an observer in the optimal control framework of the multi-objective flight controller transforms the Linear-Quadratic Regulator (LQR) control to Linear-Quadratic Gaussian (LQG) control. The state observer is designed using the Kalman filter optimal estimation method.

7.6.1. Sensing

The state observer uses the measurements from 4 accelerometers that are placed in pairs at mid-span and near the wing tip of each wing. The accelerometer pairs are located forward and aft of the elastic axis at the same spanwise location, illustrated by the red dots in Figure 7.2. This relative positioning of the accelerometer pairs with respect to the elastic axis allows the measurement of both the vertical and angular acceleration of the wing section.

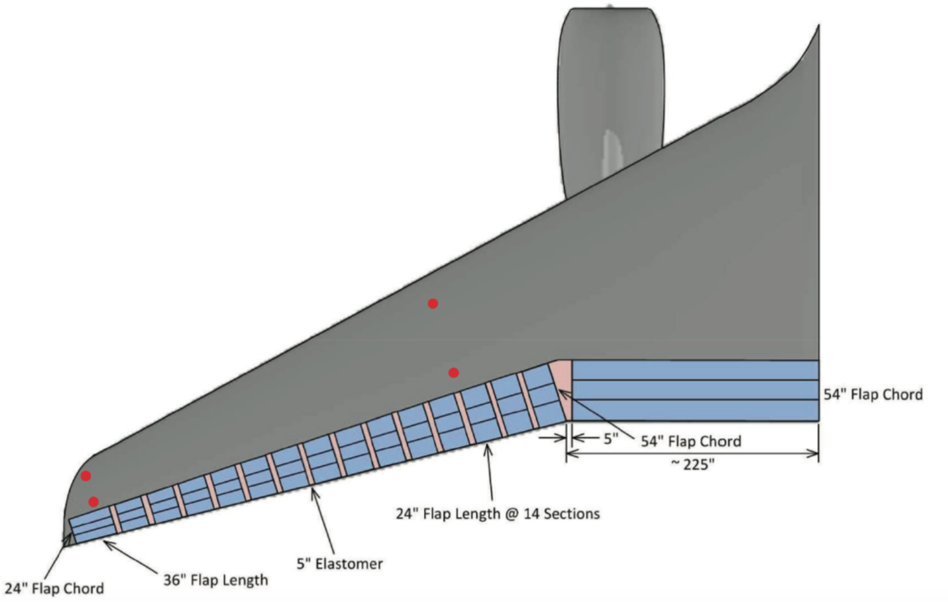

Figure 7.2: Accelerometer locations

7.6.2. Filtering

The accelerometer measurements need to be filtered before they can be used in the Kalman filter estimation. This is because of two reasons: 1) measurement noise needs to diminished, and 2) the effect of the high-frequency modes that are removed in the reduced-order model needs to be attenuated. The high-frequency modes can significantly affect the accelerometer output, but this effect is not taken into account in the predicted output of the Kalman filter. The disparity between the measured and predicted output can negatively influence the state estimation. A low-pass filter provides a solution to both problems. The cut-off frequency of the filter should be selected based on the maximum frequency of the aeroelastic modes in the reduced-order model. A Bessel filter is selected since this filter has a limited phase shift and therefore a smaller delay with respect to the accelerometer measurements [2].

7.6.3. State estimation implementation

For simulation purposes, the output of the four accelerometers is modeled. The accelerometers measure the accelerations of the aeroelastic modes. This model is computed as

$$\ddot{v} = \Phi \ddot{q} = \Phi E \dot{x}_e \tag{7.36}$$

where Φ is a matrix that contains the eigenvectors of the aeroelastic modes and $E = \begin{bmatrix} 0 & 0 & 0 & I & 0 & 0 \end{bmatrix}$ such that $\ddot{q} = E\dot{x}_e$.

Inserting the state-space system of Equation 7.3 gives

$$\ddot{v} = \Phi E G \left(A x + B u + z + w_g \right) \tag{7.37}$$

where $G = \begin{bmatrix} 0 & I & 0 & 0 & 0 \end{bmatrix}$ such that $\dot{x}_e = G\dot{x}$

For a given acceleration location, then

$$\ddot{v}_c = F \ddot{u} = F \Phi E G \left(A x + B u + z + w_g \right) \tag{7.38}$$

where F is determined from the location of the accelerometers.

Let $y = \ddot{v}_c$ be the output, then

$$y = C x + D u + I z + H w_g \tag{7.39}$$

where

$$C = F \Phi E G A \tag{7.40}$$

$$D = F \Phi E G B \tag{7.41}$$

$$I = F \varPhi E G \tag{7.42}$$

$$H = F \varPhi E G \tag{7.43}$$

The Kalman filter estimates the aeroelastic states with the use of the Kalman filter gain L. Let $\hat{x}_e = \begin{bmatrix} \hat{q} & \hat{y} & \hat{z} & \hat{\dot{q}} & \hat{\dot{y}} & \hat{\dot{z}} \end{bmatrix}^T$ be the estimation of the aeroelastic states. The estimation equation is given by

$$\dot{\hat{x}}_e = A_{er} x_r + A_{ee} \hat{x}_e + A_{e\delta} x_\delta + A_{es} x_s + B_e u + z_e + L \left(y_K - \hat{y} \right) \tag{7.44}$$

where $\hat{y}$ is the estimated output, given by

$$\hat{y} = C \begin{bmatrix} x_r^T & \hat{x}_e^T & x_\delta^T & x_s^T & x_a \end{bmatrix}^T + D u \tag{7.45}$$

and y_K is the measured accelerometer output given by

$$y_K = F(s) \left(y + v \right) \tag{7.46}$$

where $F(s)$ is the transfer function of the Bessel filter and v is the measurement noise. The measurement noise is modeled as white noise.

By implementing the state estimates into the multi-objective flight controller, Equation 7.32 transforms to

$$u = K_x \hat{x} + K_z z + \Lambda_0 \tag{7.47}$$

where $\hat{x} = \begin{bmatrix} x_r^T & \hat{x_e}^T & x_\delta^T & x_s^T & x_a \end{bmatrix}^T$.

8

Active Gust Load Alleviation Control

This chapter presents the active gust load alleviation control design. The active gust load alleviation control design will be integrated with the multi-objective flight controller. In this chapter, first the concept of active disturbance rejection control is briefly mentioned. Secondly, disturbance estimation, which is an important asset of active disturbance rejection is discussed. The last section describes the development of the active gust load alleviation control method.

8.1. Active disturbance rejection control

Active disturbance rejection control was introduced by Han in 2009 [33]. The control approach was presented as an alternative to classical PID controllers but with the performance of modern model-based control methods. The idea of active disturbance rejection control is to simultaneously suppress model uncertainties and external disturbances.

In general, the control method augments the actual system model with additional states that represent the unknown disturbances. These additional states are estimated online with a state observer. The active disturbance rejection is provided by a proportional controller.

The advantage of active disturbance rejection control is that a basic model of the system is sufficient to design the control loop. Because of this, active disturbance rejection is praised for its excellent robustness properties with respect to real-time adaptations in the system.

8.2. Disturbance estimation

Active Gust Load Alleviation is a form of active disturbance rejection control. This method requires the measurement or estimation of the disturbances. Today, new sensor techniques, such as Light Detection and Ranging, are developing rapidly and could be used for the prediction or measurement of turbulence. However, at the moment, the performance of these techniques are still substandard, and therefore this study uses disturbance estimation.

8.2.1. Extended state observer

The disturbance estimation is done using an Extended State Observer (ESO), introduced by Han in 1995 [34]. The ESO is the extended version of a Luenberger observer. This observer is selected for the disturbance estimation because of its low dependence on model accuracy and good robustness properties. The ESO estimates disturbances by extending the system of the observer states with the disturbance states. The disturbances are then estimated with the use of the error between the real states and the observed states.

8.2.2. ESO implementation

The general ESO principles are described in the following. Consider a nonlinear system of order n:

$$\begin{aligned}
\dot{x}_1 &= f_1(x_1) + g_1(x_1)\,x_2 \\
\dot{x}_2 &= f_2(x_1, x_2) + g_2\left(x_1, x_2\right) x_3 \\
&\vdots \\
\dot{x}_n &= f_n(x_1, x_2, \dots, x_n) + g_n(x_1, x_2, \dots, x_n)\,u
\end{aligned} \tag{8.1}$$

A nonlinear extended state observer of order $2n$, where the states from $\dot{x}_{n+1}$ forward are the extended states, for this system can be expressed in the general form as

$$\begin{aligned}
\dot{\hat{x}}_1 &= f_1(\hat{x}_1) + g_1(\hat{x}_1)\,\hat{x}_2 + \hat{x}_{n+1} - \beta_1^T e_1 \\
\dot{\hat{x}}_2 &= f_2(\hat{x}_1, \hat{x}_2) + g_2(\hat{x}_1, \hat{x}_2)\,\hat{x}_3 + \hat{x}_{n+2} - \beta_2^T e_2 \\
&\vdots \\
\dot{\hat{x}}_n &= f_n(\hat{x}_1, \hat{x}_2, \dots, \hat{x}_n) + g_n(\hat{x}_1, \hat{x}_2\hat{x}_2, \dots, \hat{x}_n)\,u + \hat{x}_{2n} - \beta_n^T e_n \\
\dot{\hat{x}}_{n+1} &= -\beta_{n+1}^T e_1 \\
\dot{\hat{x}}_{n+2} &= -\beta_{n+2}^T e_2 \\
&\vdots \\
\dot{\hat{x}}_{2n} &= -\beta_{2n}^T e_n
\end{aligned} \tag{8.2}$$

where $\underline{e}$ is the vector containing the estimation errors for each of the measurements

$$e_i = \hat{x}_i - x_i \qquad i = 1, \dots, n \tag{8.3}$$

The observer gains β_i of the NESO can be chosen by pole placement of the error dynamics to provide stable error dynamics [35]. The error dynamics are described by

$$\begin{aligned}
\dot{e}_1 &= e_1 - \beta_1^T e_1 \\
\dot{e}_2 &= e_1 - \beta_2^T e_2 \\
&\vdots \\
\dot{e}_n &= e_n - \beta_n^T e_n
\end{aligned} \tag{8.4}$$

For this study, Equation 8.2 can be rewritten as

$$\begin{aligned}
\dot{\hat{x}}_{1\dots n} &= Ax + Bu + z_{1\dots n} + \hat{w}_{g_{1\dots n}} - \beta_{1\dots n}^T e_{1\dots n} \\
\dot{\hat{w}}_{g_{1\dots n}} &= -\beta_{n+1\dots n}^T e_{1\dots n} \\
e_{1\dots n} &= \hat{x}_{i\dots n} - x_{i\dots n}
\end{aligned} \tag{8.5}$$

where $\hat{x}_{1\dots n}$ are the observed states, $\hat{w}_g$ are the extended states and represent the estimates of the gust contribution w_g to the system states $x_{1\dots n}$.

Once the disturbance is estimated, we can proceed with the design of active gust load alleviation.

8.3. Active gust load alleviation

Active gust load alleviation uses an augmentation of the Linear-Quadratic Gaussian controller with Model Reference Adaptive Control (MRAC) to actively suppress the effect of turbulence. An adaptive increment, calculated by MRAC laws, is added to the baseline controller. The calculation of this adaptive increment requires the estimation of the turbulence. This estimation is provided by the ESO.

An illustration of Active Gust Load Alleviation within a multi-objective flight control framework is given in Figure 8.1.

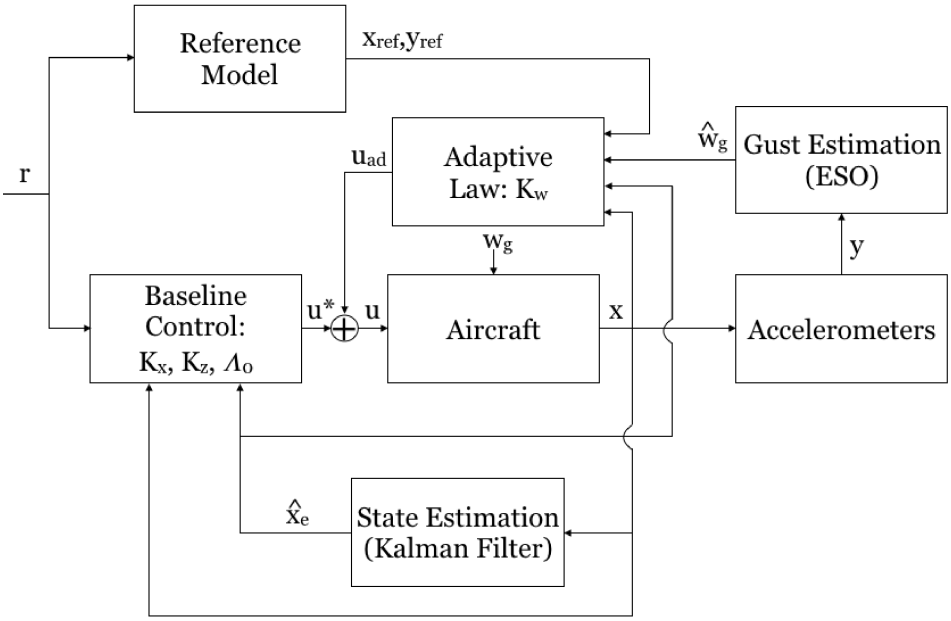

Figure 8.1: Active gust load alleviation control architecture

8.3.1. Model reference adaptive control

Model reference adaptive control creates a closed-loop controller with parameters that are updated to change the response of the system. The output of the system is compared to a reference model which represents the ideal closed-loop behavior of the system. The error between the system and the reference model is used to update the control parameters. Previous implementations of MRAC usually use the adaptive control to make a system more robust in the presence of matched uncertainties.

In this thesis, MRAC is not only used to provide more robustness but also actively counteract the effect of an unmatched uncertainty, namely turbulence. This is done by defining a reference model that specifies the desired closed-loop tracking performance in the absence of turbulence. The adaptation law is used to minimize the error between the system affected by turbulence and the reference model.

8.3.2. AGLA implementation

The adaptive disturbance rejection is designed to cancel out the disturbance w_g as follows.

The total control is defined as

$$u(x, r, t) = u^*(x, r) + u_{ad}(t) \tag{8.6}$$

where u^* is the multi-objective flight controller without disturbance estimation

$$u^* = K_x \hat{x} + K_z z + \Lambda_0 \tag{8.7}$$

and u_{ad} is the time-varying adaptive element.

The closed-loop dynamics are then obtained as

$$x = (A + BK_x)x + BK_z z + \Lambda_0 + Bu_{ad} + z + w_g \tag{8.8}$$

We define the reference model as

$$x_{ref} = A_{ref} x_{ref} + B_{ref} z + \Lambda_0 + z \tag{8.9}$$

where $A_{ref} = A + BKx$ is Hurwitz and $B_{ref} = BK_z$. The reference model represents the ideal closed-loop behavior in the absence of turbulence.

Then, the tracking error equation is obtained as

$$\dot{e} = \dot{x}_{ref} - \dot{x} = A_{ref} e - Bu_{ad} - w_g \tag{8.10}$$

If u_{ad} perfectly cancels out w_g, then the tracking error will tend to zero asymptotically, i.e., $e \to 0$ as $t_f \to \infty$. In practice, there will always be a small residual error. The adaptive signal is defined as

$$u_{ad} = \hat{K}_w \hat{w}_g \tag{8.11}$$

where $\hat{K}_w$ is the adaptive disturbance gain and $\hat{w}_g$ is the disturbance estimation. The definition of the adaptive signal as in Equation 8.11 is inspired by optimal control theory. The adaptive disturbance gain $\hat{K}_w$ can be seen as an estimate of the optimal disturbance gain K_w. This optimal disturbance gain can be derived in theory using optimal control theory and the differential Lyapunov equation. See Appendix B for the derivation of the optimal disturbance gain.

This paper introduces the estimation of the optimal disturbance gain $\hat{K}_w$ as an alternative approach in order to avoid the use of the differential Lyapunov equation.

Inserting the definition of the adaptive signal of Equation 8.11 into the tracking error equation of Equation 8.10 gives

$$\dot{e} = \dot{x}_{ref} - \dot{x} = A_{ref} e - B\hat{K}_w \hat{w}_g - w_g \tag{8.12}$$

The adaptive disturbance gain $\hat{K}_w$ is computed by the standard MRAC update law

$$\dot{\hat{K}}_w^T = \mathit{\Gamma} \hat{w}_g e^T PB \tag{8.13}$$

where Γ is the MRAC gain matrix and P is the solution to the algebraic Lyapunov equation

$$PA_{ref} + A_{ref}^T P = -Q \tag{8.14}$$

with $Q > 0$ [36]. The stability of the MRAC update law can be demonstrated with Lyapunov stability theorem.

Proof: Choose a Lyapunov candidate function

$$V = e^T Pe + \text{trace}\left(\hat{K}_w \Gamma^{-1} \hat{K}_w^T\right) \tag{8.15}$$

Then, $\dot{V}$ is evaluated as

$$\begin{aligned}\dot{V} &= -e^T Qe + 2e^T P\left(-B\hat{K}_w \hat{w}_g - w_g\right) + 2\text{trace}\left(\hat{K}_w \Gamma^{-1} \dot{\hat{K}}_w^T\right)\\ &= -e^T Qe - 2\text{trace}\left(\hat{K}_w \hat{w}_g e^T PB\right) - 2e^T Pw_g + 2\text{trace}\left(\hat{K}_w \Gamma^{-1} \dot{\hat{K}}_w^T\right)\\ &= -e^T Qe - 2e^T Pw_g + 2\text{trace}\left(\hat{K}_w\left(-\hat{w}_g e^T PB + \Gamma^{-1}\dot{\hat{K}}_w^T\right)\right)\end{aligned} \tag{8.16}$$

The definition of the update law becomes

$$-\hat{w}_g e^T PB + \Gamma^{-1}\dot{\hat{K}}_w^T = 0 \Rightarrow \dot{\hat{K}}_w^T = \Gamma \hat{w}_g e^T PB \tag{8.17}$$

Therefore $\dot{V}$ becomes

$$\dot{V} = -e^T Qe - 2e^T Pw_g \le -\lambda_{min}(Q)\, \|e\|^2 + 2\lambda_{max}(P)\, \|e\| \left\|w_g\right\| \tag{8.18}$$

Thus, $\dot{V} \le 0$ implies

$$\|e\| \ge \frac{2\lambda_{max}(P)\left\|w_g\right\|}{\lambda_{min}(Q)} \tag{8.19}$$

This implies e is bounded as $t \to \infty$. One cannot assume that $e \to 0$ because w_g is unknown.

The total control includes the linear-quadratic optimal control and the active gust load alleviation control

$$u = K_x \hat{x} + K_z z + \Lambda_0 + \hat{K}_w \hat{w}_g \tag{8.20}$$

IV

Simulations and Validation

9

Simulations

This chapter presents and discusses the simulation results. The performance of the multi-objective flight controller with active gust load alleviation is evaluated against the nominal rigid controller. The comparison looks at different performance metrics that are introduced in this chapter.

9.1. Performance metrics

The goal of the simulations is to assess the performance of the active gust load alleviation control method. Several performance metrics have been used in previous research on gust load alleviation to analyze the controller performance, as discussed in chapter 4. In this study, five performance metrics will be analyzed

1. The sum of the Euclidean norm of the rigid-body states

$$\sum_{i=1}^{m_r} \left\| x_r - x_{ref,r} \right\| = \sum_{i=1}^{m_r} \left(\sum_{j=1}^{n} \left| x_{r,ij} \right|^2 \right)^{1/2} \tag{9.1}$$

   where n is the number of samples and m_r is the number of rigid-states.

2. The sum of the Euclidean norm of the aeroelastic states

$$\sum_{i=1}^{m_e} \left\| x_e - x_{ref,e} \right\| = \sum_{i=1}^{m_e} \left(\sum_{j=1}^{n} \left| x_{e,ij} \right|^2 \right)^{1/2} \tag{9.2}$$

   where m_e is the number of elastic states.

3. The Euclidean norm of the flight path angle γ

$$\left\| \gamma - \gamma_{ref} \right\| = \left(\sum_{j=1}^{n} \left| \gamma_j \right|^2 \right)^{1/2} \tag{9.3}$$

4. The root-mean-square incremental vertical acceleration at the center of gravity of the aircraft

$$A_{z,rms} = \sqrt{\frac{1}{n} \sum_{i=1}^{n} \Delta A_{z,i}^2} \tag{9.4}$$

5. The root-mean-square bending moment at the wing root

$$M_{y,rms} = \sqrt{\frac{1}{n} \sum_{i=1}^{n} M_{y,i}^2} \tag{9.5}$$

Furthermore, the drag minimization control feature is also analyzed by evaluating the incremental drag that is calculated according to Equation 5.23.

9.2. Simulation results

Simulations are done to assess the performance of the active gust load alleviation control method in combination with the multi-objective flight controller. The simulations use the coupled ASE longitudinal dynamic model of the ESAC with VCCTEF. The controller is build using the reduced-order model that contains 10 aeroelastic modes.

The flight path angle control is designed with aeroelastic mode suppression, drag minimization, and active gust load alleviation. The flight path angle command γ_c is kept equal to 0, so normal cruise condition in the presence of turbulence is considered. Cruise conditions are at Mach 0.797 at an altitude of 36,000ft. The aeroelastic mode suppression uses a weighting matrix $Q_e = 50$ and the drag minimization uses a weighting coefficient $q_D = 5 \times 10^4$.

The simulations consider symmetric cruise conditions ($\gamma_c = 0$) and a 1-dimensional severe von Kármán turbulence model with a turbulence intensity σ of 4.5 and a characteristic length L of 1750ft.

9.2.1. Controller comparison

The performance of 7 different controllers is analyzed and compared:

1. Nominal Rigid Controller (NRC)
2. Linear-Quadratic Regulator Control (LQR)
3. Linear-Quadratic Regulator Control with Drag Minimization (LQR + DM)
4. Linear-Quadratic Regulator Control with Drag Minimization and Active Gust Load Alleviation (LQR + DM + GLA)
5. Linear-Quadratic Gaussian Control (LQG)
6. Linear-Quadratic Gaussian Control with Drag Minimization (LQG + DM)
7. Linear-Quadratic Gaussian Control with Drag Minimization and Active Gust Load Alleviation (LQG + DM + GLA)

The difference between LQR and LQG is that the LQR controller assumes that all the states can be measured, while the LQG controller uses the Kalman filter to estimate the aeroelastic states. The LQR and LQG controller both include the aeroelastic mode suppression objective ($Q_e = 50$). Drag minimization is added to the controller by switching the drag weighting coefficient q_D from 0 to 5×10^4.

9.2.2. Performance metric results

Tables 9.1 and 9.2 show the performance metric results of the flight dynamic, structural and aerodynamic responses. In these tables both the LQR and LQG simulations are shown. The LQG simulations represent the most realistic scenario's, in which the aeroelastic states cannot be measured but need to be estimated with the use of a Kalman filter. This state estimation introduces errors in the control method. For this reason, the LQR simulations are also shown. The LQR simulations show the performance of the aeroelastic mode suppression, drag minimization, and active gust load alleviation without the interference of state estimation errors.

Tables 9.1 and 9.2 show the performance difference in percentage with respect to the nominal rigid controller. A negative value indicates an increase in performance while a positive value indicates a decrease in performance.

Table 9.1: Performance metrics results: flight dynamics responses

	$\sum\|\|x_r - x_{ref,r}\|\|$	%	$\sum\|\|x_e - x_{ref,e}\|\|$	%	$\|\|y - y_{ref}\|\|$	%
NRC	0.395	0	20.355	0	1.169	0
LQR	0.368	-7	11.735	-42	1.521	30
LQR + DM	0.289	- 27	9.755	-52	0.876	-25
LQR + DM + GLA	0.114	-71	4.078	-80	0.665	-43
LQG	0.461	17	17.886	-12	0.366	-69
LQG + DM	0.321	-19	11.732	-42	0.604	-48
LQG + DM + GLA	0.175	-56	6.078	-70	0.724	-38

First of all, the Euclidean norm of the aeroelastic states $\|x_e - x_{ref,e}\|$ shows that the aeroelastic mode suppression objective is achieved. The LQR and LQG controllers substantially suppress the aeroelastic responses. Furthermore, the Euclidean norms of the rigid-body states $\|x_r - x_{ref,r}\|$ and aeroelastic states $\|x_e - x_{ref,e}\|$ show the ability of the AGLA to significantly counteract the effects of the turbulence by suppressing these state vectors. The drag minimization objective also shows a positive side effect in suppressing the rigid-body and aeroelastic states. The performance metric related to the flight path angle $\|\gamma - \gamma_{ref}\|$ shows an increase in performance for the LQR controllers when adding drag minimization and active gust load alleviation. The LQG controller, however, shows the opposite effect with respect to this flight path angle performance metric. These contrary results could be caused by errors in the aeroelastic state estimation.

Table 9.2: Performance metrics results: structural and aerodynamic responses

	A_z [ft/s^2]	%	$M_{y,rms}$ [ft-lb]	%	ΔC_D [dragcount]	%
NRC	0.482	0	63598	0	18	0
LQR	0.296	-39	26352	-59	23	28
LQR + DM	0.241	-50	15374	-76	21	17
LQR + DM + GLA	0.268	-44	10584	-83	18	0
LQG	0.187	-61	46289	-27	21	17
LQG + D.M.	0.235	-51	29781	-53	19	6
LQG + DM + GLA	0.269	-44	10533	-83	19	6

The results in Table 9.2 show the ability of active gust load alleviation to significantly decrease the root-mean-square of the wing root bending moment $M_{y,rms}$. As mentioned in chapter 4, the wing root bending moment is a main criterion in the analysis of gust load alleviation controls. The vertical acceleration of the center of gravity $A_{z,rms}$ decreases when including aeroelastic mode suppression, but further does not show a coherent relation with the controller type. The incremental drag ΔC_D is lowest for the nominal rigid controller. However, the effect of drag minimization control is certainly noticeable when comparing the LQR and LQG controllers with the LQR and LQG controller with drag minimization.

9.2.3. Rigid-body response

Figures 9.1-9.4 show the incremental rigid-body response of the aircraft to the severe von Kármán turbulence. The plots compare the responses of the nominal rigid controller, the LQG controller with aeroelastic mode suppression, the LQG controller with aeroelastic mode suppression and drag minimization and the LQG controller with aeroelastic mode suppression, drag minimization, and active gust load alleviation. The angle of attack $\Delta\alpha$ and pitch angle $\Delta\theta$ illustrate the improvements gained by including drag minimization and the significant improvement when including active gust load alleviation. The pitch rate Δq shows a clear improvement of all the LQG controllers with respect to the nominal rigid controller. Furthermore, active gust load alleviation shows the largest improvement in suppressing the response of the pitch rate. The flight path angle γ response benefits the most from aeroelastic mode suppression and the LQG controllers perform better than the nominal rigid controller.

9.2.4. Aeroelastic response

Figures 9.5 - 9.7 show the response of the first three aeroelastic modes. The effect of active gust load alleviation is clearly visible. The LQG controller with mode suppression, drag minimization, and active gust load alleviation performs best in suppressing the aeroelastic states.

9.2.5. Control surface commands

Figures 9.8 - 9.12 show the control surface deflections of the elevator and the VCCTEF. The VCCTEF sections are numbered from 1 at the wing root to 16 at the wing tip. The elevator deflections are well within the standard elevator deflection limit of 25° and the deflection rates are well-behaved. The VCCTEF deflections are illustrated separately for the four different controllers. For all control methods the VCCTEF deflections are well-behaved and within the deflection limit of 20°. Furthermore, the deflection limit constraint of 2° between each adjacent flap section is obeyed. The inclusion of the aeroelastic mode suppression objective

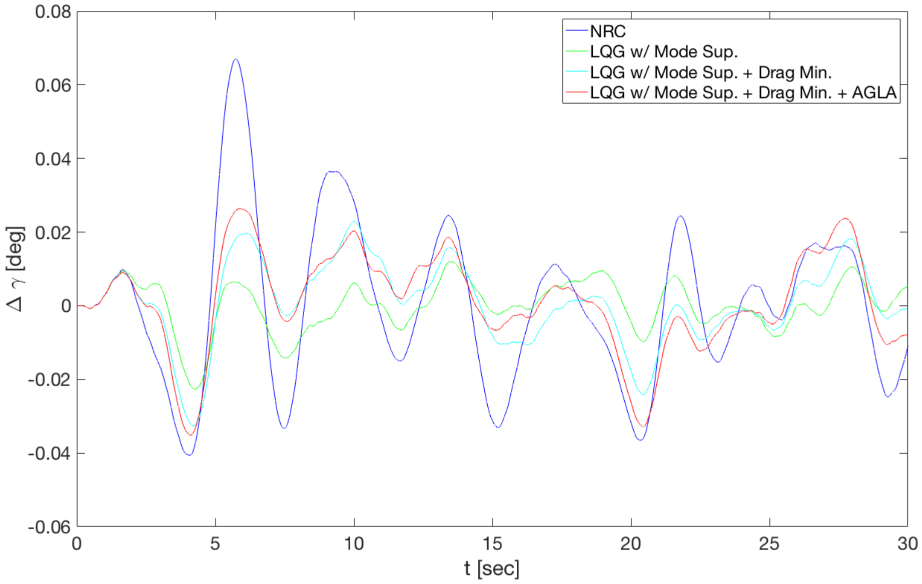

Figure 9.1: Flight path angle response to multi-objective flight control with mode suppression, drag minimization and active gust load alleviation

results in higher control surface deflections.

9.2.6. Structural, acceleration, and aerodynamic response

Figures 9.13 - 9.15 show the wing root bending moment response ΔM_y, vertical acceleration at the center of gravity response ΔA_z, and the incremental drag response ΔC_D. The wing root bending moment is significantly decreased with the use of active gust load alleviation. The vertical acceleration at the center of gravity is mainly suppressed by the aeroelastic mode suppression objective. The incremental drag is lowest for the nominal rigid controller. However, the drag minimization objective decreases the incremental drag with respect to the LQG controller.

9.2.7. Kalman filter state estimation

The Kalman filter estimation of the first three aeroelastic modes is shown in Figures 9.16 - 9.18. The figures show that the state estimation captures to a large extent the response of the aeroelastic states. The estimations, however, have a clear off-set to real values. This estimation error is caused by the omission of the turbulence effect in the Kalman filter state estimation.

The Kalman filter estimation plots of the remaining first 10 aeroelastic modes are given in Appendix C.

9.2.8. ESO disturbance estimation

The performance of the ESO disturbance estimation is evaluated by analyzing Figures 9.19 - 9.22. In these figures, the estimation of the disturbance to the angle of attack w_{g_α} and the disturbance to the first aeroelastic mode $w_{g_{q1}}$ are compared for the LQR and LQG simulations. First of all, for both the LQR and LQG simulations the estimation of the disturbance to the angle of attack is reasonably accurate. Secondly, the estimation of the disturbance to the first aeroelastic mode is again accurate for the LQR simulation, but far off for the LQG simulation. This means that the errors between the actual and estimated aeroelastic states significantly impact the ESO estimation of the disturbances related to the aeroelastic states.

Further turbulence estimation plots are given in Appendix D.

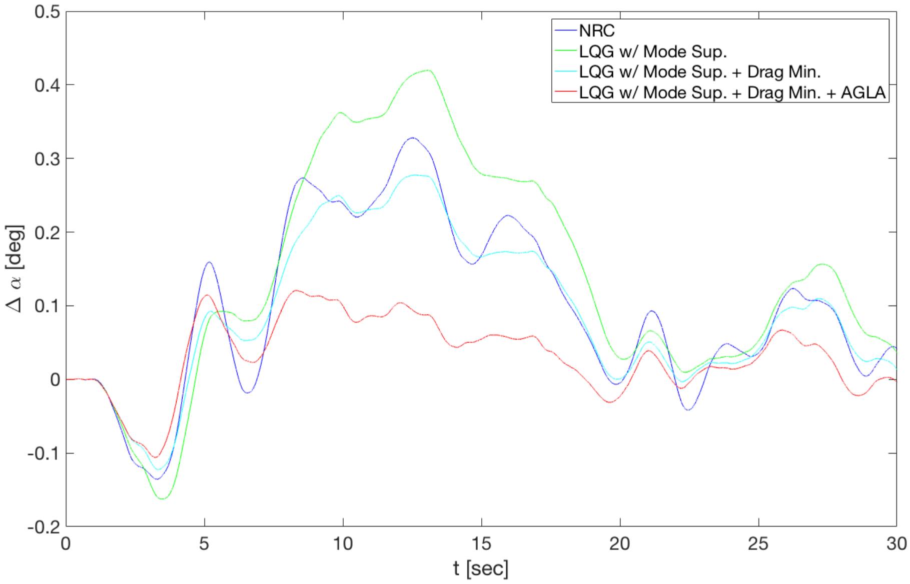

Figure 9.2: Angle of attack response to multi-objective flight control with mode suppression, drag minimization and active gust load alleviation

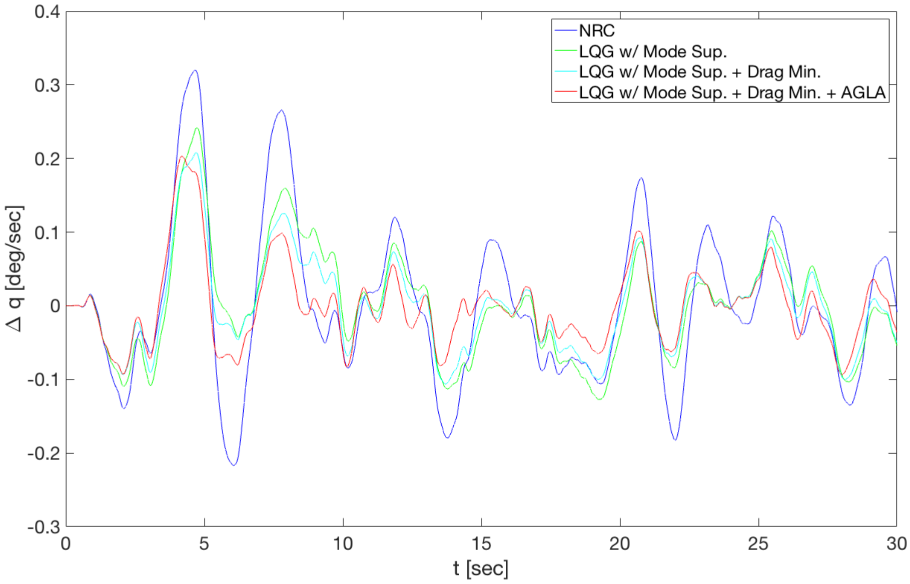

Figure 9.3: Pitch rate response to multi-objective flight control with mode suppression, drag minimization and active gust load alleviation

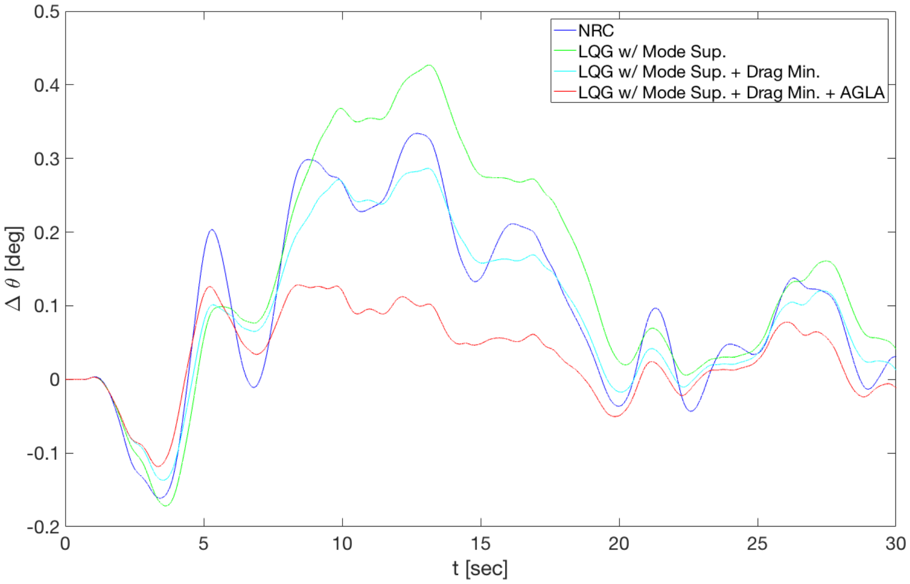

Figure 9.4: Pitch angle response to multi-objective flight control with mode suppression, drag minimization and active gust load alleviation

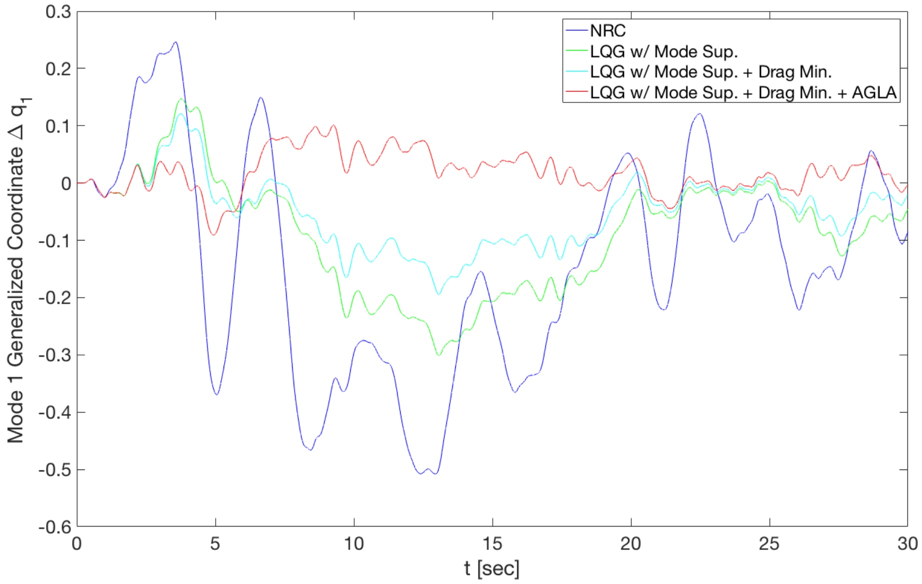

Figure 9.5: First symmetric aeroelastic response to multi-objective flight control with mode suppression, drag minimization and active gust load alleviation

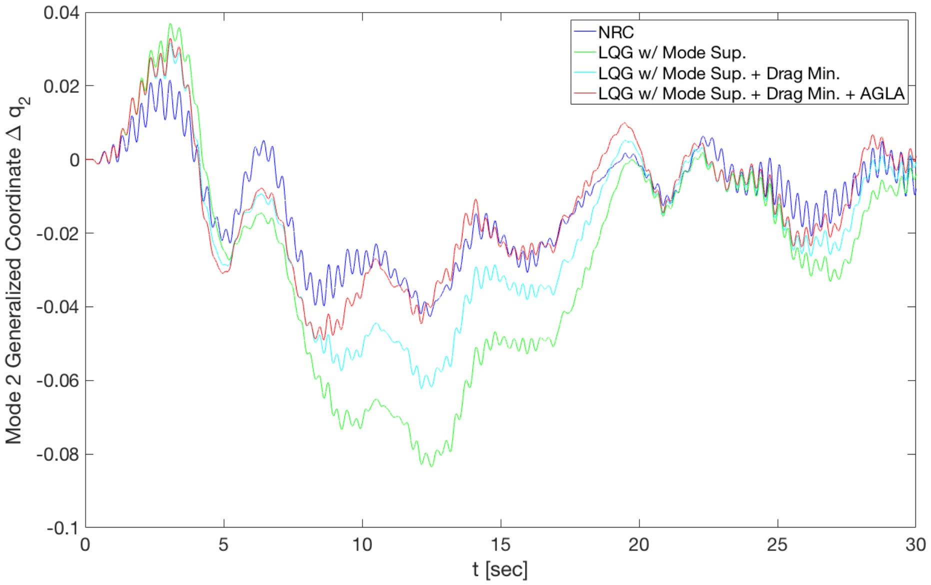

Figure 9.6: Second symmetric aeroelastic to multi-objective flight control with mode suppression, drag minimization and active gust load alleviation

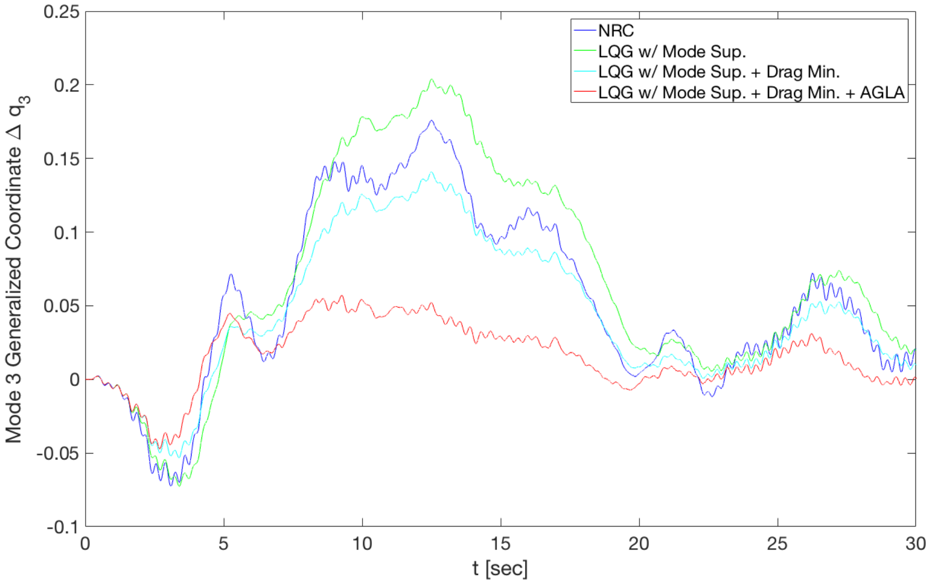

Figure 9.7: Third symmetric aeroelastic to multi-objective flight control with mode suppression, drag minimization and active gust load alleviation

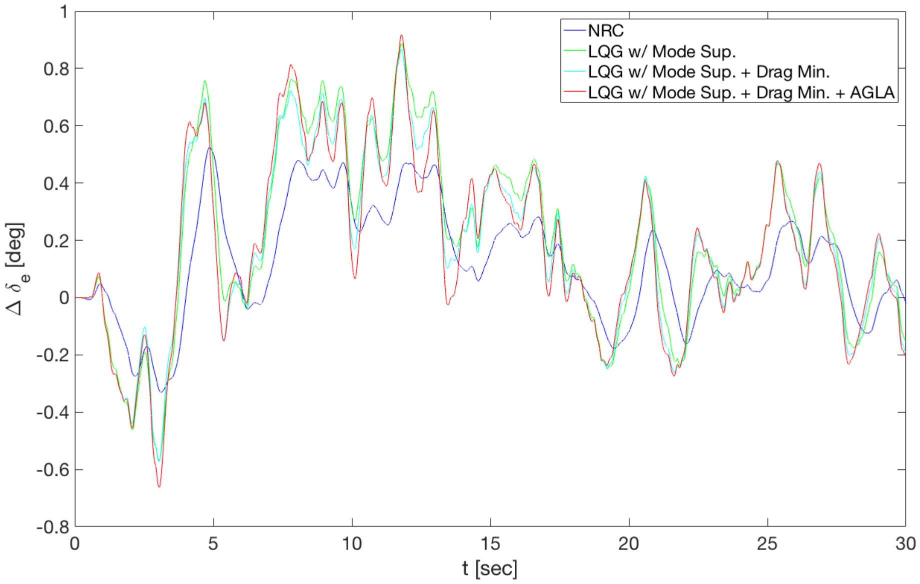

Figure 9.8: Elevator input to multi-objective flight control with mode suppression, drag minimization and active gust load alleviation

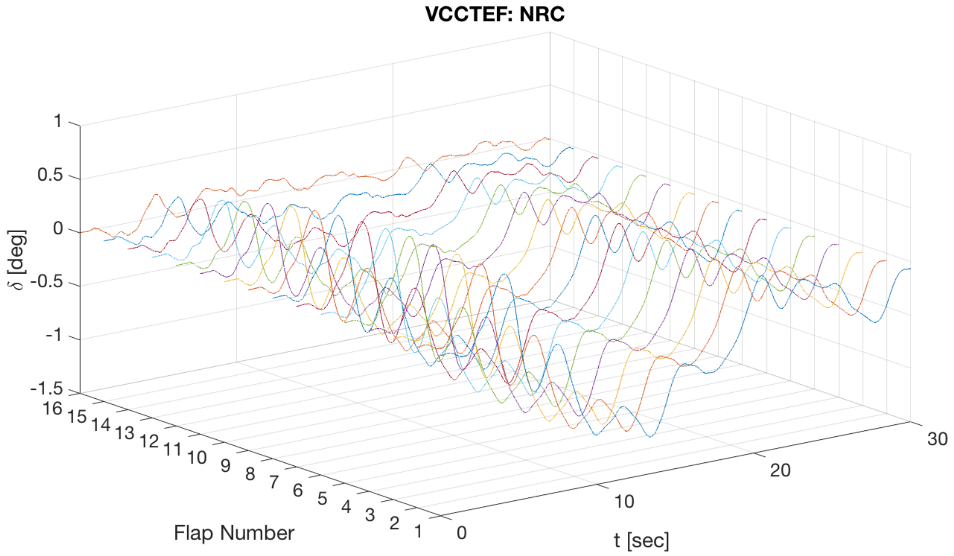

Figure 9.9: VCCTEF input for nominal rigid controller

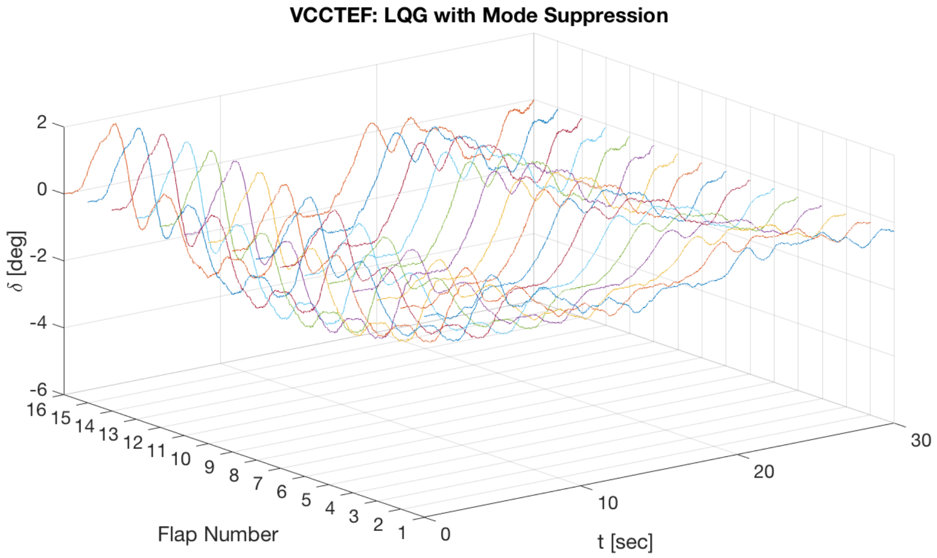

Figure 9.10: VCCTEF input for Linear-Quadratic Gaussian control with aeroelastic mode suppresion

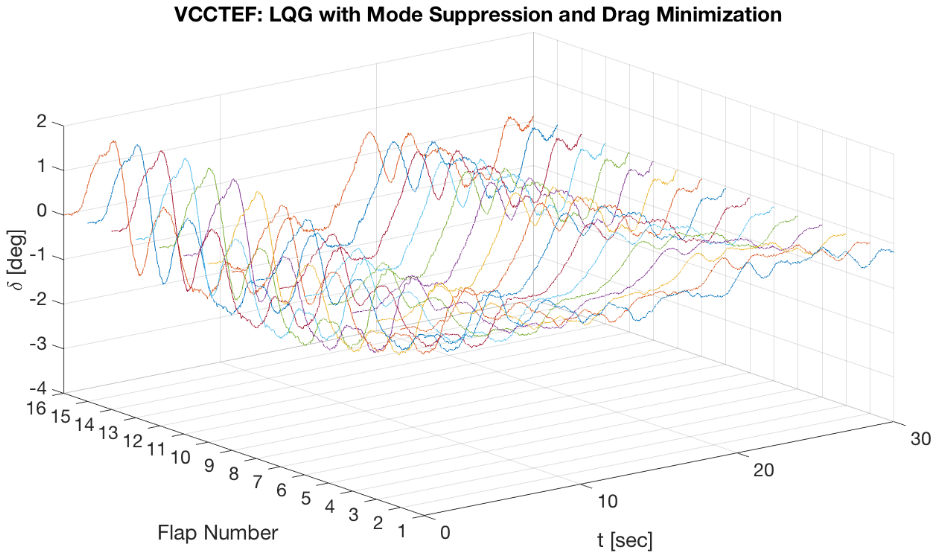

Figure 9.11: VCCTEF input for Linear-Quadratic Gaussian control with aeroelastic mode suppresion and drag minimization

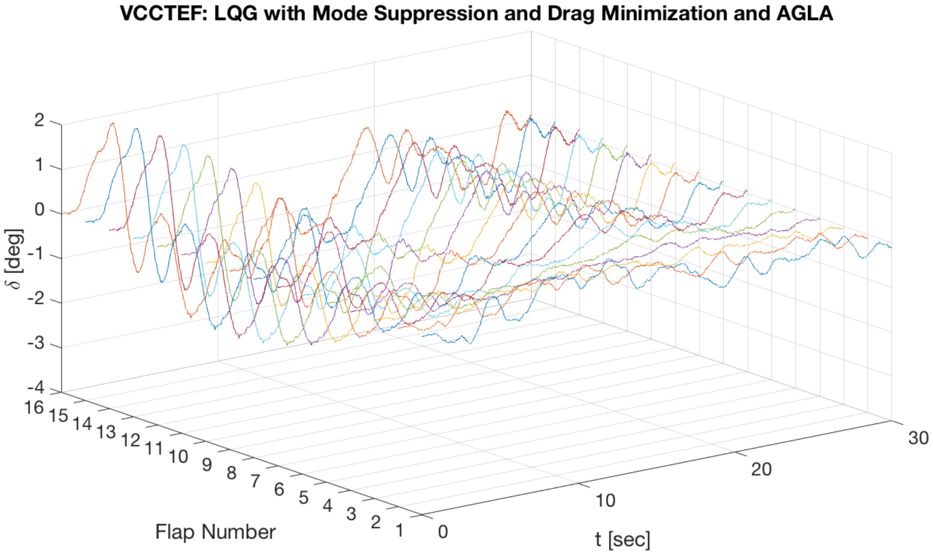

Figure 9.12: VCCTEF input for Linear-Quadratic Gaussian control with aeroelastic mode suppresion, drag minimization and active gust load alleviation

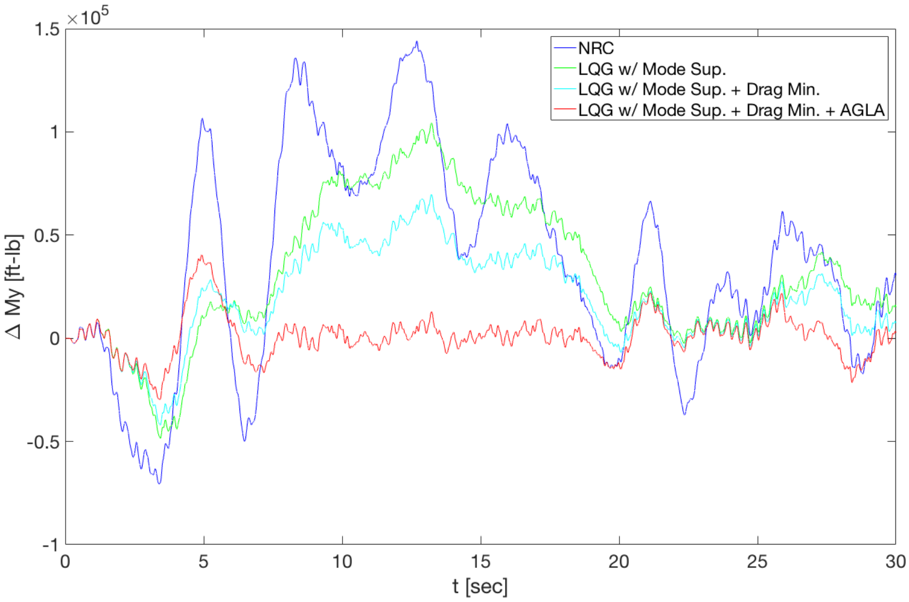

Figure 9.13: Wing root bending moment response to multi-objective flight control with mode suppression, drag minimization and active gust load alleviation

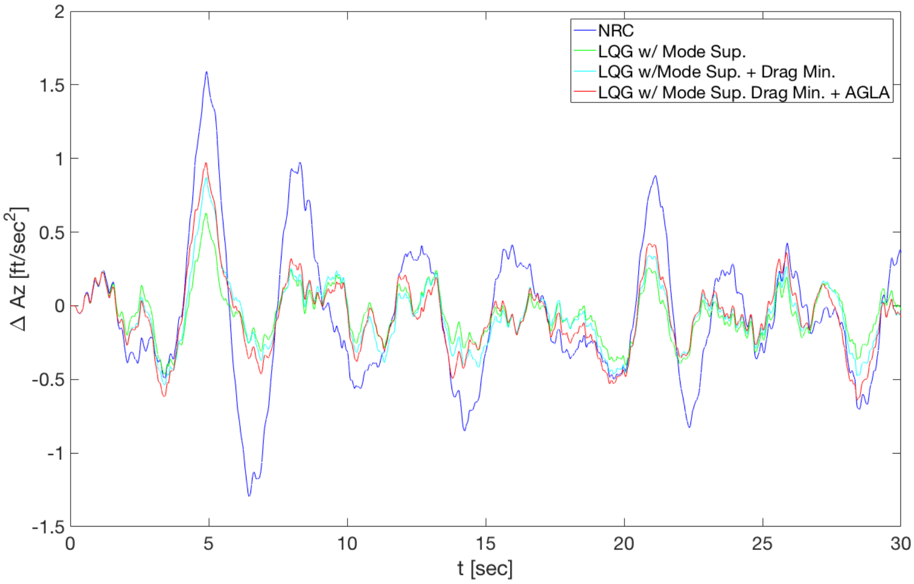

Figure 9.14: Vertical acceleration of the aircraft center of gravity response to multi-objective flight control with mode suppression, drag minimization and active gust load alleviation

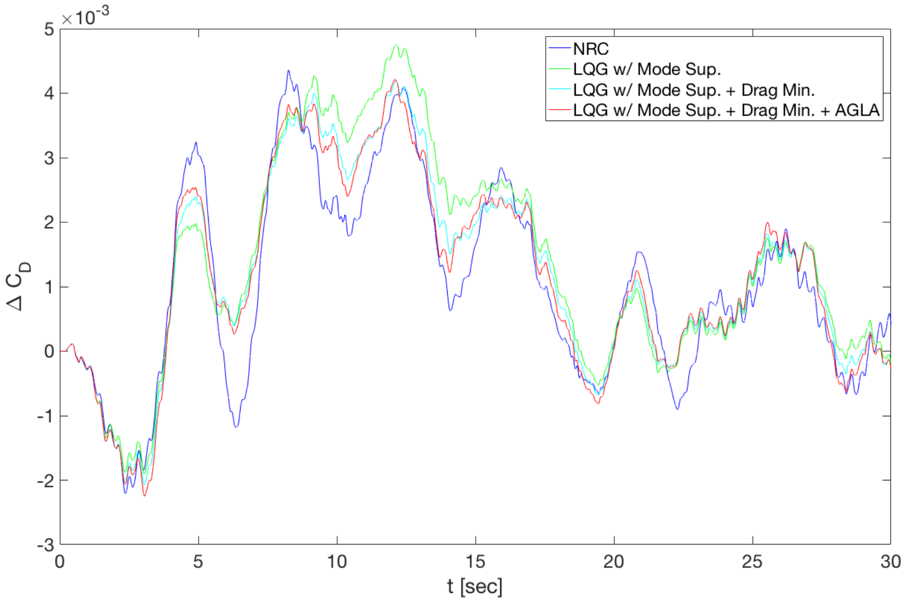

Figure 9.15: Incremental drag response to multi-objective flight control with mode suppression, drag minimization and active gust load alleviation

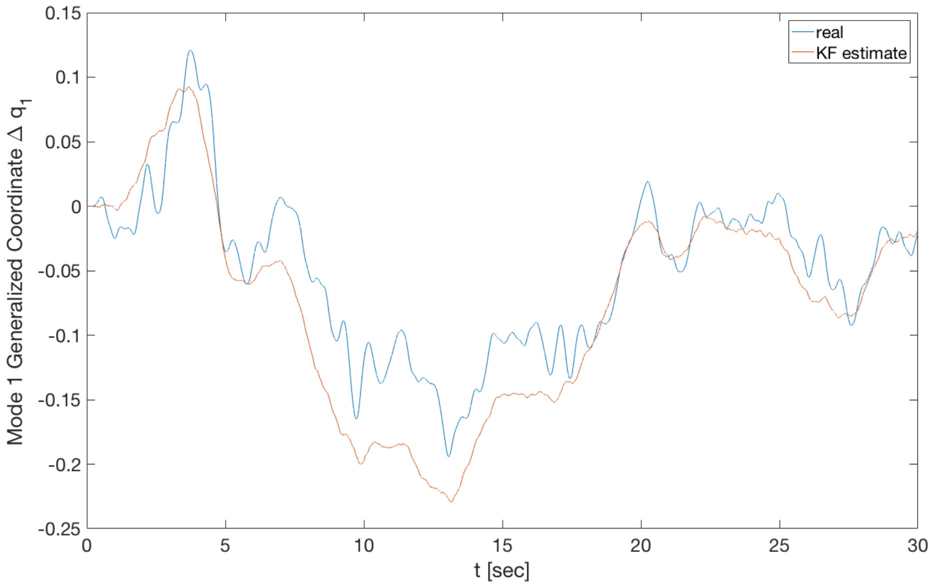

Figure 9.16: Kalman filter estimation of the first aeroelastic mode

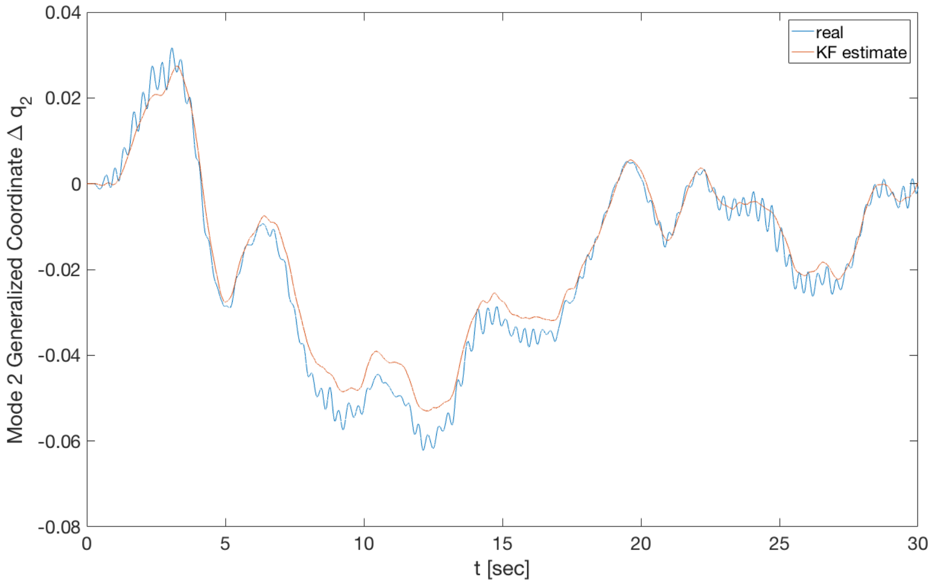

Figure 9.17: Kalman filter estimation of the first aeroelastic mode

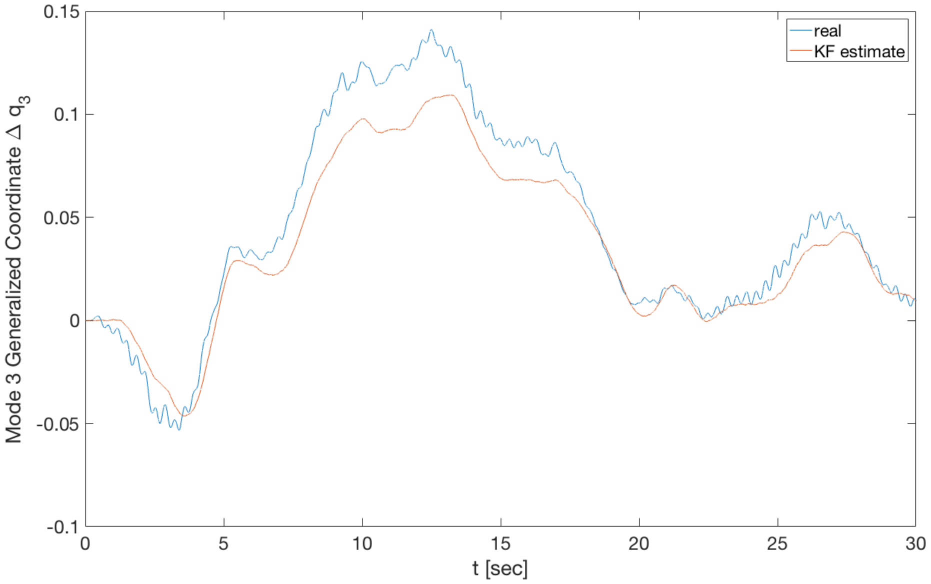

Figure 9.18: Kalman filter estimation of the first aeroelastic mode

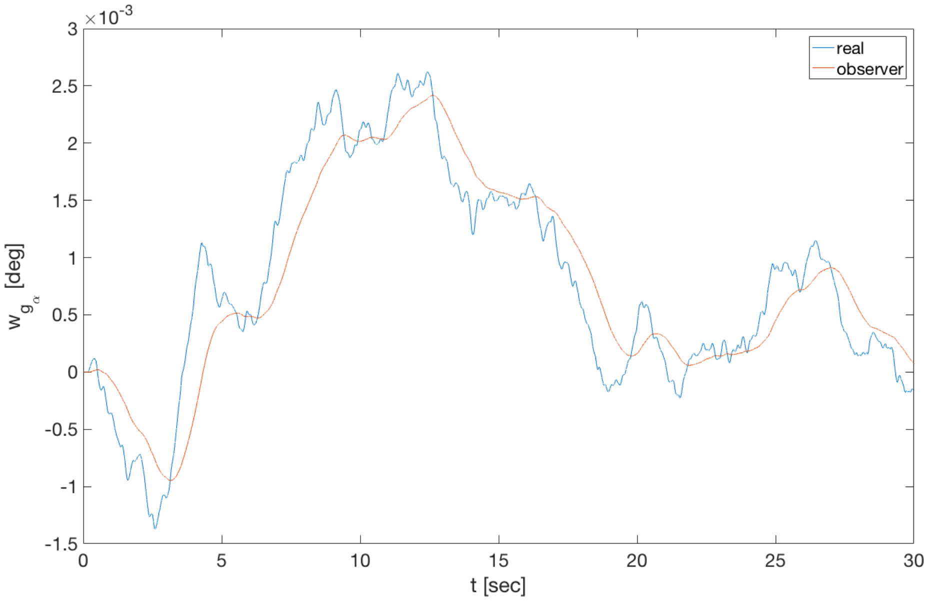

Figure 9.19: ESO disturbance estimation of disturbance to the angle of attack for LQR controller

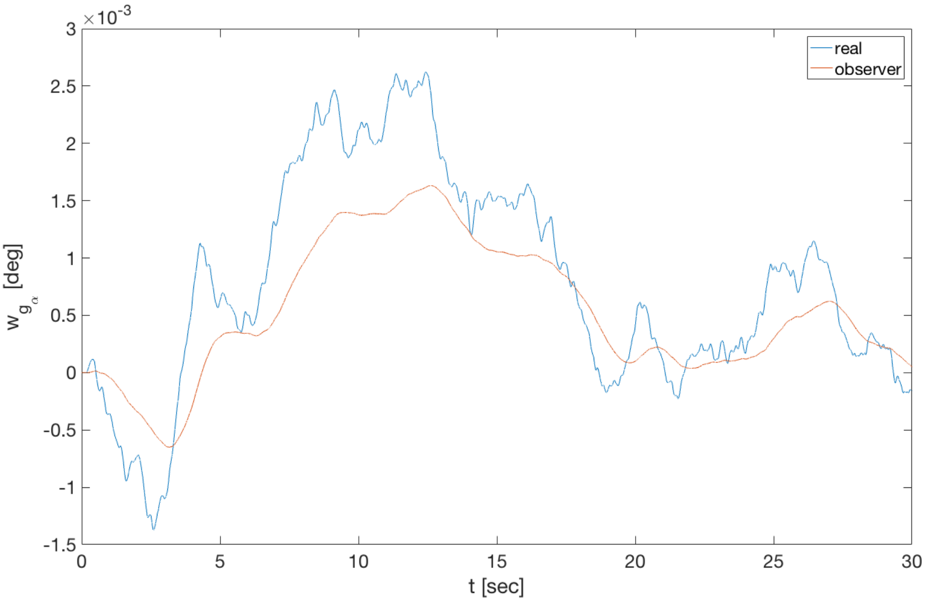

Figure 9.20: ESO disturbance estimation of disturbance to the angle of attack for LQG controller

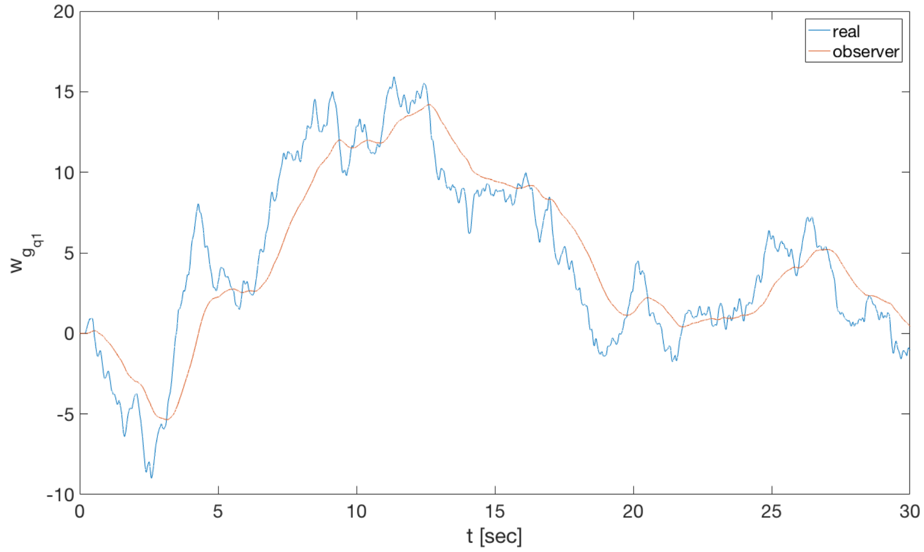

Figure 9.21: ESO disturbance estimation of disturbance to the first symmetric aeroelastic mode for LQR controller

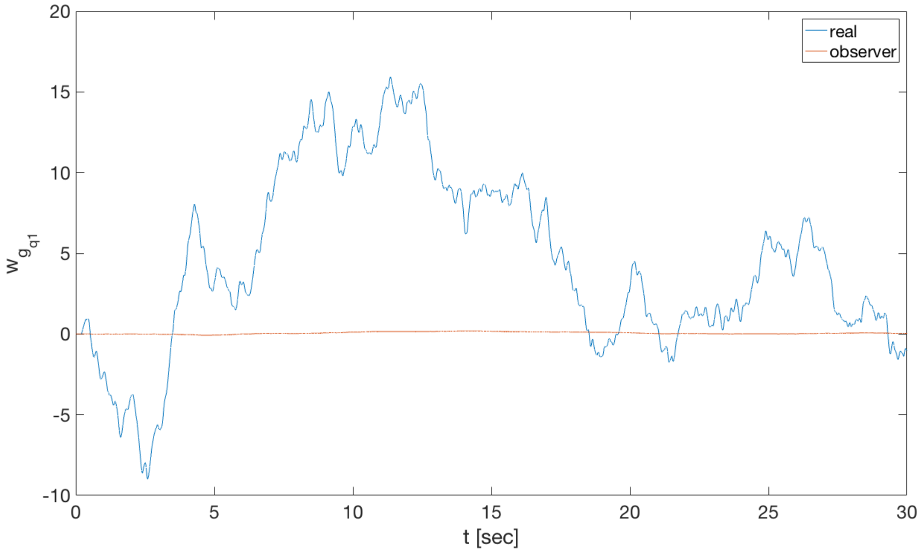

Figure 9.22: ESO disturbance estimation of disturbance to the first symmetric aeroelastic mode for LQG controller

10

Validation

In scientific research, validations are of utmost importance in order to conclude if a causal relation can be generalized to other cases. In this study, the active gust load alleviation control is validated for six additional turbulence models.

1. Dryden Light with intensity $\sigma = 1.5$ and characteristic length $L = 1750 ft$
2. Dryden Moderate with intensity $\sigma = 1.5$ and characteristic length $L = 1750 ft$
3. Dryden Severe with intensity $\sigma = 3.0$ and characteristic length $L = 1750 ft$
4. von Kármán Light with intensity $\sigma = 3.0$ and characteristic length $L = 1750 ft$
5. von Kármán Moderate with intensity $\sigma = 5.0$ and characteristic length $L = 1750 ft$
6. von Kármán Severe with intensity $\sigma = 5.0$ and characteristic length $L = 1750 ft$

The validation results are summarized in Table 10.1. Table 10.1 shows the difference in performance metrics in percentage when comparing an LQG controller with and without active gust load alleviation. A negative value indicates an increase in performance while a positive value indicates a decrease in performance. For all six turbulence models, active gust load alleviation increases the performance with respect to the rigid-body states $\left\| x_r - x_{ref,r} \right\|$, aeroelastic states $\left\| x_e - x_{ref,e} \right\|$, and wing root bending moment $M_{y,rms}$. However, it decreases the performance with respect to the flight path angle $\left\| \gamma - \gamma_{ref} \right\|$ and does not show any coherent relation with respect to the vertical acceleration at the center of gravity $A_{z,rms}$.

Table 10.1: Validation results for active gust load alleviation

	$\sum\|\|x_r - x_{ref,r}\|\|$ [%]	$\sum\|\|x_e - x_{ref,e}\|\|$ [%]	$\|\|\gamma - \gamma_{ref}\|\|$ [%]	A_z [%]	$M_{y,rms}$ [%]
Dryden Light	-21	-17	5	-6	-18
Dryden Moderate	-45	-42	23	2	-43
Dryden Severe	-49	-47	21	-1	-38
Von Kármán Light	-31	-40	29	3	-29
Von Kármán Moderate	-53	-57	35	1	-59
Von Kármán Severe	-38	-43	0	2	-45

The flight dynamic and structural response plots of the validation simulations are illustrated in Appendix E. Furthermore, Appendix E shows the performance metric results for the validation simulations for the seven controllers mentioned in chapter 9.

V

Conclusion and Recommendations

11

Conclusion

This report presents the design of an Active Gust Load Alleviation controller within a Multi-Objective Flight Controller design framework for a flexible wing aircraft.

The increased flexibility of novel aircraft structures asks for the compensation of negative aeroelastic effects. Performance Adaptive Aeroelastic Wing (PAAW) technology provides aeroelastic compensation by using wing shaping to maximize the aerodynamic performance, while simultaneously addressing operational constraints. PAAW technology uses a multi-disciplinary approach to ensure control effectiveness and aerodynamic efficiency throughout the flight envelope. The Variable Camber Continuous Trailing Edge Flap (VCCTEF) is a novel multi-segment trailing-edge control system that can provide aeroelastic wing shaping by changing the camber of the flexible wing aircraft for various flight conditions.

The VCCTEF can be used as an active aeroelastic effector to improve the aerodynamic efficiency for different flight phases as well as a high-bandwidth control device that provides flight maneuvering, load alleviation, and aeroelastic mode damping.

The ability of the VCCTEF to provide aeroelastic wing shaping can be used to simultaneously fulfill multiple control objectives. This approach can be seen as a multi-objective flight control framework that consists of the following control objectives: pilot command-following control, aeroelastic mode suppression, drag minimization and, load alleviation.

The objective of this thesis is to design a multi-objective flight controller that includes aeroelastic mode suppression, drag minimization, and gust load alleviation. The main contribution to the scientific body is the design of an active gust load alleviation approach.

Active gust load alleviation attempts to directly suppress the effects of external disturbances. The controller consists of a baseline Linear-Quadratic Gaussian controller and an adaptive increment that provides the active gust load alleviation control. The baseline controller provides the control for a flight path angle control mode together with aeroelastic mode suppression and drag minimization objectives based on optimal control theory. The adaptive increment is designed using Model Reference Adaptive Control. The adaptive increment tries to minimize the error between the real system and a reference model that represents the ideal closed-loop behavior of the system in the absence of turbulence. The design of the adaptive increment requires the estimation of the turbulence disturbances. This estimation is done using an Extended State Observer.

Simulations are done to evaluate the performance of the multi-objective flight controller with active gust load alleviation against a nominal rigid controller. The simulations use an aeroservoelastic model of the NASA Generic Transport Model (GTM). The stiffness and torsion properties of the GTM are reduced to have a flexible wing aircraft called the Elastically Shaped Aircraft Concept (ESAC). The aeroservoelastic model of the ESAC has the VCCTEF integrated on the wings. The aeroelastic states cannot be measured but need to be estimated to be used in the feedback controller design. The estimation is done using Kalman filter optimal state estimation.

The active gust load alleviation control is validated using various von Kármán and Dryden turbulence models.

The performance of the controllers are based on five performance metrics that look at the rigid-body response, the aeroelastic response, the response of the flight path angle, the wing root bending moment, and the vertical acceleration at the aircraft center of gravity.

The simulation results show that the active gust load alleviation control approach is able to significantly suppresses the rigid-body and aeroelastic flight dynamic responses. Furthermore, active gust load alleviation significantly decreases the wing root bending moment. The flight path angle response shows substantial improvements for the Linear-Quadratic Regulator control with active gust load alleviation, but contradictory results for the Linear-Quadratic Gaussian control. This inconsistency could be appointed to errors in the aeroelastic state estimation. The vertical acceleration of the aircraft center of gravity does not show any coherent relation with the controller types. Next to evaluating the active gust load alleviation approach, the aeroelastic mode suppression and drag minimization objectives in the multi-objective flight control framework also show improvements in the performance of their incentives.

Validation of the active gust load alleviation control approach is done for six different Dryden and von Kármán turbulence models. The validation results agree with the simulation results. Active gust load alleviation significantly improves the performance of the rigid-body, aeroelastic and wing root bending moment responses. The performance with respect to the flight path angle decreases when comparing the LQG controller with the LQG controller with active gust load alleviation. The vertical acceleration of the aircraft center of gravity shows no consistent trend.

The goal of this thesis was to answer the main research question on the application of a gust load alleviation control approach within a multi-objective flight control framework for a flexible wing aircraft embodied with the VCCTEF. The simulation and validation results show that an active gust load alleviation control method was successfully applied within a multi-objective control design for the Elastically Shaped Aircraft Concept.

12

Discussion and Future Research

The active gust load alleviation control within the multi-objective flight control framework has provided satisfactory results. However, as inherent to research, improvements can be made on the control and simulation design.

First of all, the Kalman filter optimal state estimation could be improved. In this study, the estimation error between the system states and the estimated aeroelastic states degrades the performance of the baseline controller and the active gust load alleviation control. The more the estimated states resemble the system states, the better the baseline optimal controller performs. Furthermore, improving the aeroelastic state estimation will benefit the ESO disturbance estimation, which results in more effective gust load alleviation control. Improvements in the aeroelastic state estimation can be made in the filter design and/or estimation gains. Additionally, an idea would be to include the ESO disturbance estimations in the Kalman filter optimal state estimation.

Secondly, in the presence of a bounded disturbance, such as turbulence, the Lyapunov stability theorem shows that only bounded tracking can be accomplished. Additionally, the robustness of the active gust load alleviation adaptive law can be increased by implementing a robust modification scheme such as optimal control modification [37].

Thirdly, this study does not include any relative deflection rate limits for the spanwise flap sections of the VCCTEF in the control design. In reality, the elastomer transition material will impose a constraint on the relative deflection rates. Future research should address the relative deflection rates of the elastomer material and implement the accompanied constraints in the control design.

Furthermore, the deflection of the VCCTEF is constrained to a cubic Chebyshev polynomial shape function in this study. It is plausible that a higher order or more flexible shape function can improve the controller performance by allowing more degrees of freedom. Further research should look into the effect of the shape constraint on the multi-objective flight control and active gust load alleviation control performance.

Finally, stability margins of the controllers should be analyzed to determine how robust they are. This can be done by injecting a time delay at the input to assess the time delay margin of the controllers. The LQR is expected to be the most robustly stable among all the controllers but it is not realizable. On the other hand, the LQG can be designed with a Loop Transfer Recovery (LTR) method to provide a stability margin close to that of the LQR [36, 38] .

Bibliography

[1] Nguyen. N, *Elastically Shaped Future Air Vehicle Concept*, NASA Innovation Fund Award 2010 Report, October 2010, submitted to NASA Innovative Partnerships Program, http://ntrs.nasa.gov/archive/nasa/casi.ntrs.nasa.gov/20110023698.pdf.

[2] Nguyen, N., and Tal, E., *A Multi-Objective Flight Control Approach for Performance Adaptive Aeroelastic Wing*, 65th AIAA/ASCE/AHS/ASC Structures, Structural Dynamics, and Materials Conference AIAA 2015-1843, January 2015.

[3] Lebofksy, S., Ting, E., and Nguyen, N., *Aeroelastic Modeling and Drag Optimization of Aircraft Wing with Variable Camber Continuous Trailing Edge Flap*, 32nd AIAA Applied Aerodynamics, AIAA 2014-2443, June 2014.

[4] Ippolito, C., Nguyen, N., Totah, J., Trinh, K., and Ting, E., *Initial Assessment of a Variable-Camber Continuous Trailing-Edge Flap System on a Rigid Wing for Drag Reduction in Subsonic Cruise*, AIAA Infotech@Aerospace, AIAA 2013-5143, August 2013.

[5] Lebofksy, S., Ting, E., and Nguyen, N., *Multidisciplinary Drag Optimization of Reduced Stiffness Flexible Wing Aircraft With Variable Camber Continuous Trailing Edge Flap*, 56th AIAA/ASCE/AHS/ASC Structures, Structural Dynamics, and Materials Conference, AIAA 2015-1408, January 2015.

[6] Ferrier, Y., Nguyen, N., and Ting, E., *Real-time Adaptive Least-Squares Drag Minimization for Performance Adaptive Aeroelastic Wing*, 34th AIAA Applied Aerodynamics, AIAA 2016-3567, June 2016.

[7] Nguyen, N., Ting, E., Chaparro, D., Drew, M., and Swei, S., *Multi-Objective Flight Control for Drag Minimization and Load Alleviation of High-Aspect Ratio Flexible Wing Aircraft*, 58th AIAA/ASCE/AHS/ASC Structures, Structural Dynamics, and Materials Conference, AIAA 2017-1589, January 2017.

[8] Nguyen, N., *A Framework for Adaptive Aeroelastic Wing Shaping Control*, Applied Modeling & Simulation (AMS) Seminar Series, 2014.

[9] Lilienthal, O., *Der Vogelflug als Grundlage der Fliegekunst*, Publishing house R. Görtner, Berlin 1889, reprinting, publishing company Oldenbourg Munich, 1943.

[10] Nguyen, N., *A Framework for Adaptive Aeroelastic Wing Shaping Control*, April 2014.

[11] Nguyen, N., Trinh, K., Reynolds, K., Kless., J., Aftosmis, M., Urnes, J. and Ippolito, C., *Elastically Shaped Wing Optimization and Aircraft Concept for Improved Cruise Efficiency*, 51st AIAA Aerospace Sciences Meeting, AIAA 2013-0141, January 2013.

[12] Nguyen, N., Kaul, U., Lebofsky, S., Ting., E., Chaparro, D. and Urnes, J., *Development of Variable Camber Continous Trailing Edge Flap for Performance Adaptive Aeroelastic Wing*, SAE 2015 AeroTech Congress & Exhibition, 2015-01-2565, September 2015.

[13] Kaul, U. and Nguyen, N., *Drag Optimization Study of Variable Camber Continuous Trailing Edge Flap (VCCTEF) Using OVERFLOW*, 32nd AIAA Applied Aerodynamics, AIAA 2014-2444, June 2014.

[14] Nguyen, N., Precup, N., Urnes, J., Nelson, C., Lebofsky, S., Ting, E., and Livne, E., *Experimental Investigation of a Flexible Wing with a Variable Camber Continous Trailing Edge Flap Design*, 32nd AIAA Applied Aerodynamics, AIAA 2014-2441, June 2014.

[15] Nguyen, N., *NASA Demo of Multi-Objective Flight Control for Drag Minimization and Load Alleviation*, August 2016.

[16] Mushfiqul, A., Hromcik, M., and Hanis, T. *Active gust load alleviation system for flexible aircraft: Mixed feedforward/feedback approach*, Aerospace Science and Technology 41, pp. 122-133, January 2015.

[17] Paletta, N., *Maneuver Load Controls, Analysis and Design for Flexible Aircraft*, November 2011.

[18] Regan, C.D. and Jutte, C.V., *Survey of Applications of Active Control Technology for Gust Alleviation and New Challenges for Lighter-weight Aircraft*, NASA/TM 2012-216008, April 2012.

[19] Lucas, A.M., Valasek, J., and Strganac, W. *Gust Load Alleviation of an Aeroelastic System using Nonlinear Control*, 50th AIAA/ASCE/AHS/ASC Structures, Structural Dynamics, and Materials Conference, AIAA 2009-2536, May 2009.

[20] Frost, S.A., Taylor, B.R., and Bodson, M. *Investigation of Optimal Control Allocation for Gust Load Alleviation in Flight Control*, AIAA Atmospheric Flight Mechanics Conference, AIAA 2012-4858, August 2012.

[21] Giesseler, H.-G., Kopf, M., Varutti, P., Faulwasser, T., Findeisen, R., *Model Predictive Control for Gust Load Alleviation*, 4th IFAC Nonlinear Model Predictive Control Conference, August 2012.

[22] Haghighat, S., Liu, H.H.T., and Martins, J.R.R.A, *Model-Predictive Gust Load Alleviation Controller for a Highly Flexible Aircraft*, Journal of Guidance, Control, and Dynamics, November-December 2012.

[23] Gangsaas, D., Ly, U. and Norman, D.C., *Practical Gust Load Alleviation and Flutter Suppression Control Laws Based on a LQG Methodology*, 19th AIAA Aerospace Sciences Meeting, AIAA 1981-0021, January 1981.

[24] Cook, R.G., and Palacios, R. *Robust Gust Alleviation and Stabilization of Very Flexible Aircraft*, AIAA Journal, Vol. 51, No.2, February 2013.

[25] Wildschek, A., Maier, R., Hromcik, M., Hanis, T., Schirrer, A., Kozek, M., Westermayer, C., and Hemedi, M., *Hybrid Controller for Gust Load Alleviation and Ride Comfort Improvement Using Direct Lift Control Flaps*, 3rd European Conference for Aerospace Sciences (EUCASS), April 2011.

[26] Croft, J., *NASA Airstar: taking the simulator out to play*, Flightglobal, Available from https://www.flightglobal.com/news/articles/nasa-airstar-taking-the-simulator-out-to-play-343714/ 2010.

[27] Theodorsen, T., *General Theory of Aerodynamic Instability and the Mechanism of Flutter*, Technical Report No.496, NACA, 1938.

[28] Tal, E., Nguyen, N., and Ting, E., *Comparison of Unsteady Aerodynamics Approximations for Time-Domain Representation of Frequency-Independent Aeroelastic State-Space Models*, 56th AIAA/ASME/ASCE/AHS/ASC Structures, Structural Dynamics, and Materials Conference, January 2015.

[29] Tal, E. and Nguyen, N., *Unsteady Aeroservoelastic Modeling of Flexible Wing Generic Transport Aircraft with Variable Camber Continuous Trailing Edge Flap*, 33rd AIAA Applied Aerodynamics Conference, AIAA 2015-2722, June 2015.

[30] Nguyen, N. and Urnes, J., *Aeroelastic Modeling of Elastically Shaped Aircraft Concept via Wing Shaping Control for Drag Reduction*, AIAA Atmospheric Flight Mechanics Conference, AIAA-2012-4642, August 2012.

[31] Küssner, H.G., *Zusammenfassender Bericht über den instationären Autrieb von Flügeln*, Luftfahrtforschung, 13 (12), pp. 410-424, 1937.

[32] Bisplinghoff, R. L., Ashley, H., and Halfman, R.L., *Aeroelasticity*, Addison-Wesley Publishing Company, Inc., 1996.

[33] Han, J., *From PID to active disturbance rejection control*, IEEE Trans. Ind. Electron, 56, pp. 900-906, 2009.

[34] Han, J., *Control and Decision* ***138***, Vol. 85, 1995.

[35] Erazo, C., Angulo, F., and Olivar, G., *Stability analysis of the extended state observers by Popov criterion*, Theoretical & Applied Mechanics Letters **2**, 043006, 2012.

[36] Lavretsky, E., and Wise, K.A., *Robust and Adaptive Control with Aerospace Applications*, Springer-Verlag, London, 2013.

[37] Nguyen, N., *Optimal control modification for robust adaptive control with large adaptive gain*, Systems and Control Letters 61, March 2012.

[38] Stengel, R., *Optimal Control and Estimation*, Dover Publications, New York, 1994.

[39] Huang, Y., Xu, K., Han, J., and Lam, J., *Flight Control Design using Extended State Observer and Non-Smooth Feedback*, 40th IEEE Conference on Decision and Control, 2001.

[40] Nguyen, N., Swei, S., and Ting, E., *Adaptive Linear Quadratic Gaussian Optimal Control Modification for Flutter Suppression of Adaptive Wing*, AIAA Infotech@Aerospace, AIAA 2015-0118, January 2015.

[41] Lebofsky, S., Ting, E., Nguyen, N., and Trinh, K., *Optimization for Load Alleviation of Truss-Braced Wing Aircraft With Variable Camber Continuous Trailing Edge Flap*, 33rd AIAA Applied Aerodynamics Conference, AIAA 2015-2723, June 2015.

[42] Lebofsky, S., Ting, E., and Nguyen, N., *Aeroelastic Modeling and Drag Optimization of Flexible Wing Aircraft with Variable Camber Continuous Trailing Edge Flap*, 32nd AIAA Applied Aerodynamics, AIAA 2014-2443, June 2014.

[43] Woods-Vedeler, J.A., Pototzky A.S., and Hoadley, S.T., *Active Load Control During Rolling Maneuvers*, NASA Technical Paper 3455, October 1994.

[44] White, R.J., *Improving the Airplane Efficiency by Use of Wing Maneuver Load Alleviation*, Journal of Aircraft, Vol. 8, No.10, October 1971.

[45] Woods-Vedeler, J.A., Pototzky A.S., and Hoadley, S.T., *Rolling Maneuver Load Alleviation Using Active Controls*, Journal of Aircraft, Vol. 32, No.1, January-February 1995.

[46] Gaulocher, S.L., Roos, C., and Cumer, C., *Aircraft Load Alleviation During Maneuvers Using Optimal Control Surface Combinations*, Journal of Guidance, Control and Dynamics, Vol. 30, No.2, March-April 2007.

[47] Paletta, N., *Maneuver Load Controls, Analysis and Design for Flexible Aircraft*, November 2011.

[48] Yang, Y., Wu, Z., and Yang, C., *Control Surface Efficiency Analysis and Utilization of an Elastic Airplane for Maneuver Loads Alleviation*, 54th AIAA/ASME/ASCE/AHS/ASC Structures, Structural Dynamics, and Materials Conference, April 2013.

[49] Burlion, L.,Poussot-Vassal, C., Vuillemin, P., Leitner, M., and Kier, T., *Longitudinal Manouvre Load Control of a Flexible Large-Scale Aircraft*, 19th World Congress of the International Federation of Automatic Control, August 2014.

[50] Nguyen, N., Ting, E., and Trinh, K., *Flight Dynamic Modeling and Stability Analysis of Flexible Wing Generic Transport Aircraft*, 55th AIAA/ASME/ASCE/AHS/SC Structures, Structural Dynamics, and Materials Conference and Exhibit, 2014.

[51] Butler, H., *Model Reference Adaptive Control: Bridging the gap between theory and practice*, November 1990.

[52] Misra, P., *A Computational Algorithm for Squaring-Up Part I: Zero Input-Output Matrix*, 31st Conference on Decision and Control, December 1992.

[53] Misra, P., *Numerical Algorithms for Squaring-Up Non-Square Systems Part II: General Case*, American Control Conference, January 1993.

[54] Lavretsky, E., Gibson, T.E., and Annaswamy, A.M., *Projection Operator in Adaptive Systems*, arXiv:1112.4232v6, October 2012.

[55] Lu, P., *Fault Diagnosis and Fault-Tolerant Control for Aircraft Subjected to Sensor and Actuator Faults*, PhD thesis at Delft University of Technology, September 2016.

[56] Viitala, M., *Obsever Incremental Backstepping*, Master thesis at Delft University of Technology, 2013.

[57] Whitaker, H.P., Yamron, J., and Kezer, A., *Design of Model Reference Adaptive Control Systems for Aircraft*, Report R-164, Instrumentation Laboratory, M. I. T. Press, Cambridge, Massachusetts, 1958.

[58] Anderson, B.D.O. and Moore, J.B., *Optimal Control, Linear Quadratic Methods*, Prentice-Hall, Inc., 1989.

[59] Kreisselmeier, G., and Narendram, K.S., *Stable model reference adaptive control in the presence of bounded disturbances*, IEEE Transaction on Automatic Control 27, December 1982.

VI

Appendices

A

Mass, Stiffness, and Control Matrices of Aeroservoelastic State-Space Model

This appendix presents the mass, stiffness and control matrices of the aeroservoelastic state-space model of the GTM aircraft embodied with the VCCTEF.

The mass matrices in Equation 5.16 are defined as:

$$M_{rr} = M_r - Q_r \tag{A.1}$$

$$M_{re} = \begin{bmatrix} 0 & 0 & 0 & -V_{rn} & 0 & 0 \end{bmatrix} \tag{A.2}$$

$$M_{r\delta} = \begin{bmatrix} 0 & 0 & 0 & -F_{rn} & 0 & 0 \end{bmatrix} \tag{A.3}$$

$$M_{rs} = \begin{bmatrix} 0 & 0 \end{bmatrix} \tag{A.4}$$

$$M_{er} = \begin{bmatrix} 0 \\ 0 \\ 0 \\ -Q_e \\ 0 \\ 0 \end{bmatrix} \tag{A.5}$$

$$M_{ee} = \begin{bmatrix} I & 0 & 0 & 0 & 0 & 0 \\ 0 & I & 0 & 0 & 0 & 0 \\ 0 & 0 & I & 0 & 0 & 0 \\ 0 & 0 & 0 & M_s + M_{an} & 0 & 0 \\ 0 & 0 & 0 & 0 & I & 0 \\ 0 & 0 & 0 & 0 & 0 & I \end{bmatrix} \tag{A.6}$$

$$M_{e\delta} = \begin{bmatrix} 0 & 0 & 0 & 0 & 0 & 0 \\ 0 & 0 & 0 & 0 & 0 & 0 \\ 0 & 0 & 0 & 0 & 0 & 0 \\ 0 & 0 & 0 & -F_{en} & 0 & 0 \\ 0 & 0 & 0 & 0 & 0 & 0 \\ 0 & 0 & 0 & 0 & 0 & 0 \end{bmatrix} \tag{A.7}$$

$$M_{es} = \begin{bmatrix} 0 & 0 \\ 0 & 0 \\ 0 & 0 \\ 0 & 0 \\ 0 & 0 \\ 0 & 0 \end{bmatrix} \tag{A.8}$$

$$M_{\delta r} = \begin{bmatrix} 0 \\ 0 \\ 0 \\ -Q_\delta \\ 0 \\ 0 \end{bmatrix} \tag{A.9}$$

$$M_{\delta e} = \begin{bmatrix} 0 & 0 & 0 & 0 & 0 & 0 \\ 0 & 0 & 0 & 0 & 0 & 0 \\ 0 & 0 & 0 & 0 & 0 & 0 \\ 0 & 0 & 0 & -V_{\delta n} & 0 & 0 \\ 0 & 0 & 0 & 0 & 0 & 0 \\ 0 & 0 & 0 & 0 & 0 & 0 \end{bmatrix} \tag{A.10}$$

$$M_{\delta\delta} = \begin{bmatrix} I & 0 & 0 & 0 & 0 & 0 \\ 0 & I & 0 & 0 & 0 & 0 \\ 0 & 0 & I & 0 & 0 & 0 \\ 0 & 0 & 0 & M_\delta - F_{\delta n} & 0 & 0 \\ 0 & 0 & 0 & 0 & I & 0 \\ 0 & 0 & 0 & 0 & 0 & I \end{bmatrix} \tag{A.11}$$

$$M_{\delta s} = \begin{bmatrix} 0 & 0 \\ 0 & 0 \\ 0 & 0 \\ 0 & 0 \\ 0 & 0 \\ 0 & 0 \end{bmatrix} \tag{A.12}$$

$$M_{sr} = \begin{bmatrix} 0 \\ 0 \end{bmatrix} \tag{A.13}$$

$$M_{se} = \begin{bmatrix} 0 & 0 & 0 & 0 & 0 & 0 \\ 0 & 0 & 0 & 0 & 0 & 0 \end{bmatrix} \tag{A.14}$$

$$M_{s\delta} = \begin{bmatrix} 0 & 0 & 0 & 0 & 0 & 0 \\ 0 & 0 & 0 & 0 & 0 & 0 \end{bmatrix} \tag{A.15}$$

$$M_{ss} = \begin{bmatrix} I & 0 \\ 0 & I \end{bmatrix} \tag{A.16}$$

The stiffness matrices in Equation 5.16 are defined as:

$$S_{rr} = P_r \tag{A.17}$$

$$S_{re} = \begin{bmatrix} S_{rn} + 0.5S_{rc} + a_4\left(\frac{2V_\infty}{c}\right)T_{rc} & S_{rc} & \left(\frac{2V_\infty}{c}\right)T_{rc} & T_{rn} + 0.5T_{rc} & 0 & 0 \end{bmatrix} \tag{A.18}$$

$$S_{r\delta} = \begin{bmatrix} D_{rn} + 0.5D_{rc} + a_4\left(\frac{2V_\infty}{c}\right)E_{rc} & D_{rc} & \left(\frac{2V_\infty}{c}\right)E_{rc} & E_{rn} + 0.5E_{rc} & 0 & 0 \end{bmatrix} \tag{A.19}$$

$$S_{rs} = \begin{bmatrix} D_r & 0 \end{bmatrix} \tag{A.20}$$

$$S_{er} = \begin{bmatrix} 0 \\ 0 \\ 0 \\ P_e \\ 0 \\ 0 \end{bmatrix} \tag{A.21}$$

$$S_{ee}=\begin{bmatrix} 0 & 0 & 0 & I & 0 & 0\\ 0 & 0 & 0 & 0 & I & 0\\ 0 & 0 & 0 & 0 & 0 & I\\ -\left[K_s+0.5K_{ac}+a_4\left(\frac{2V_\infty}{c}\right)C_{ac}\right] & -K_{ac} & -\left(\frac{2V_\infty}{c}\right)C_{ac} & -\left(C_s+C_{an}+0.5C_{ac}\right) & 0 & 0\\ 0.5a_2\left(\frac{2V_\infty}{c}\right)^2 & -a_2\left(\frac{2V_\infty}{c}\right)^2 & 0 & a_4\left(\frac{2V_\infty}{c}\right) & -a_3\left(\frac{2V_\infty}{c}\right) & 0\\ a_6\left(\frac{2V_\infty}{c}\right)^2 & 0 & -a_2\left(\frac{2V_\infty}{c}\right)^2 & a_5\left(\frac{2V_\infty}{c}\right) & 0 & -a_3\left(\frac{2V_\infty}{c}\right) \end{bmatrix} \tag{A.22}$$

$$S_{e\delta}=\begin{bmatrix} 0 & 0 & 0 & 0 & 0 & 0\\ 0 & 0 & 0 & 0 & 0 & 0\\ 0 & 0 & 0 & 0 & 0 & 0\\ D_{en}+0.5D_{ec}+a_4\left(\frac{2V_\infty}{c}\right)E_{ec} & D_{ec} & \left(\frac{2V_\infty}{c}\right)E_{ec} & E_{en}+0.5E_{ec} & 0 & 0\\ 0 & 0 & 0 & 0 & 0 & 0\\ 0 & 0 & 0 & 0 & 0 & 0 \end{bmatrix} \tag{A.23}$$

$$S_{es}=\begin{bmatrix} 0 & 0\\ 0 & 0\\ 0 & 0\\ 0 & 0\\ 0 & 0\\ 0 & 0 \end{bmatrix} \tag{A.24}$$

$$S_{\delta r}=\begin{bmatrix} 0\\ 0\\ 0\\ P_\delta\\ 0\\ 0 \end{bmatrix} \tag{A.25}$$

$$S_{\delta e}=\begin{bmatrix} 0 & 0 & 0 & 0 & 0 & 0\\ 0 & 0 & 0 & 0 & 0 & 0\\ 0 & 0 & 0 & 0 & 0 & 0\\ S_{\delta n}+0.5S_{\delta c}+a_4\left(\frac{2V_\infty}{c}\right)T_{\delta c} & S_{\delta c} & \left(\frac{2V_\infty}{c}\right)T_{\delta c} & T_{\delta n}+0.5T_{\delta c} & 0 & 0\\ 0 & 0 & 0 & 0 & 0 & 0\\ 0 & 0 & 0 & 0 & 0 & 0 \end{bmatrix} \tag{A.26}$$

$$S_{\delta\delta}=\begin{bmatrix} 0 & 0 & 0 & I & 0 & 0\\ 0 & 0 & 0 & 0 & I & 0\\ 0 & 0 & 0 & 0 & 0 & I\\ -K_\delta+D_{\delta n}+0.5D_{\delta c}+a_4\left(\frac{2V_\infty}{c}\right)E_{\delta c}+k_p & D_{\delta c} & \left(\frac{2V_\infty}{c}\right)E_{\delta c} & -C_\delta+E_{\delta n}+0.5E_{\delta c}+k_\delta & 0 & 0\\ 0.5a_2\left(\frac{2V_\infty}{c}\right)^2 & -a_2\left(\frac{2V_\infty}{c}\right)^2 & 0 & a_{4\left(\frac{2V_\infty}{c}\right)} & -a_3\left(\frac{2V_\infty}{c}\right) & 0\\ a_6\left(\frac{2V_\infty}{c}\right)^2 & 0 & -a_2\left(\frac{2V_\infty}{c}\right)^2 & a_5\left(\frac{2V_\infty}{c}\right) & 0 & -a_3\left(\frac{2V_\infty}{c}\right) \end{bmatrix} \tag{A.27}$$

$$S_{\delta s}=\begin{bmatrix} 0 & 0\\ 0 & 0\\ 0 & 0\\ 0 & k_i\\ 0 & 0\\ 0 & 0 \end{bmatrix} \tag{A.28}$$

$$S_{sr}=\begin{bmatrix} 0\\ 0 \end{bmatrix} \tag{A.29}$$

$$S_{se} = \begin{bmatrix} 0 & 0 & 0 & 0 & 0 & 0 \\ 0 & 0 & 0 & 0 & 0 & 0 \end{bmatrix} \tag{A.30}$$

$$S_{s\delta} = \begin{bmatrix} 0 & 0 & 0 & 0 & 0 & 0 \\ I & 0 & 0 & 0 & 0 & 0 \end{bmatrix} \tag{A.31}$$

$$S_{ss} = \begin{bmatrix} -\lambda & 0 \\ 0 & 0 \end{bmatrix} \tag{A.32}$$

The control matrices in Equation 5.16 are defined as:

$$T_r = \begin{bmatrix} 0 & 0 \end{bmatrix} \tag{A.33}$$

$$T_e = \begin{bmatrix} 0 & 0 \\ 0 & 0 \\ 0 & 0 \\ 0 & 0 \\ 0 & 0 \\ 0 & 0 \end{bmatrix} \tag{A.34}$$

$$T_\delta = \begin{bmatrix} 0 & 0 \\ 0 & 0 \\ 0 & 0 \\ 0 & -k_p \\ 0 & 0 \\ 0 & 0 \end{bmatrix} \tag{A.35}$$

$$T_s = \begin{bmatrix} \lambda & 0 \\ 0 & -I \end{bmatrix} \tag{A.36}$$

B

Optimal Disturbance Gain

This appendix shows the derivation of the optimal disturbance gain K_w using optimal control. Consider the state-space system of Equation 7.3

$$\dot{x} = Ax + Bu + z + w_g \tag{B.1}$$

An optimal control is designed with the following cost function

$$J = \frac{1}{2}\int_0^{t_f} \left(x^T Q x + u^T R u\right) dt \tag{B.2}$$

where $Q = Q_r \oplus Q_e \oplus Q_\delta \oplus Q_s \oplus Q_a > 0$.

We define the Hamiltonian as

$$H = \frac{1}{2}\left(x^T Q x + u^T R u\right) + \lambda^T \left(Ax + Bu + z + w_g\right) \tag{B.3}$$

The adjoint equation and optimal control are obtained as

$$\dot{\lambda} = -\frac{\partial H^T}{\partial x} = -Qx - A^T \lambda \tag{B.4}$$

$$\frac{\partial H^T}{\partial u} = Ru + B^T \lambda = 0 \Rightarrow u = -R^{-1} B^T \lambda \tag{B.5}$$

Let $\lambda = Wx + Vz + T$. Then

$$\dot{W}x + W\dot{x} + \dot{V}z + V\dot{z} + \dot{T} = -Qx - A^T (Wx + Vz + T) \tag{B.6}$$

In this study, the command flight path angle γ_c is constant and therefore $\dot{\gamma}_c = 0$. Let $t_f \to \infty$, then the optimal solution approaches a steady state solution. Therefore, according to the transversality condition, $\dot{W}\left(t_f\right) = 0$ and $\dot{V}\left(t_f\right) = 0$. Then, separating terms yields the following expressions

$$WA + A^T W - WBR^{-1}B^T W + Q = 0 \tag{B.7}$$

$$V = -\left(A^T - WBR^{-1}B^T\right)^{-1} W \tag{B.8}$$

$$\dot{T} = -\left(A^T - WBR^{-1}B^T\right) T - W\hat{w}_g \tag{B.9}$$

Equation B.9 is a differential Lyapunov equation and needs to be calculated numerically. This is done with the following derivation

$$\dot{T} = \frac{T_{i+1} - T_i}{\Delta t} = -\left(A^T - WBR^{-1}B^T\right) T - W\hat{w}_g \tag{B.10}$$

$$T_{i+1} = T_i - \Delta t \left(A^T - WBR^{-1}B^T\right) T - W\hat{w}_g \tag{B.11}$$

In the presence of state and disturbance estimation, the multi-objective flight controller is expressed as

$$u = K_x\hat{x} + K_z z + K_w \tag{B.12}$$

where

$$K_x = -R^{-1}B^T W \tag{B.13}$$

$$K_z = -R^{-1}B^T V \tag{B.14}$$

$$K_w = -R^{-1}B^T T \tag{B.15}$$

Another approach would be to define λ as $\lambda = Wx + Vz + T\hat{w}_g$. The adjoint equation in Equation B.4 then becomes

$$\dot{W}x + W\dot{x} + \dot{V}z + V\dot{z} + \dot{T}\hat{w}_g + T\dot{\hat{w}}_g = -Qx - A^T\left(Wx + Vz + T\hat{w}_g\right) \tag{B.16}$$

It is invalid to assume that $\dot{\hat{w}}_g = 0$ and therefore Equation B.16 cannot be solved analytically nor numerically.

C

Aeroelastic State Estimation using Kalman Filter

This appendix shows the aeroelastic state estimation of the fourth till tenth aeroelastic modes using the Kalman filter optimal estimation method.

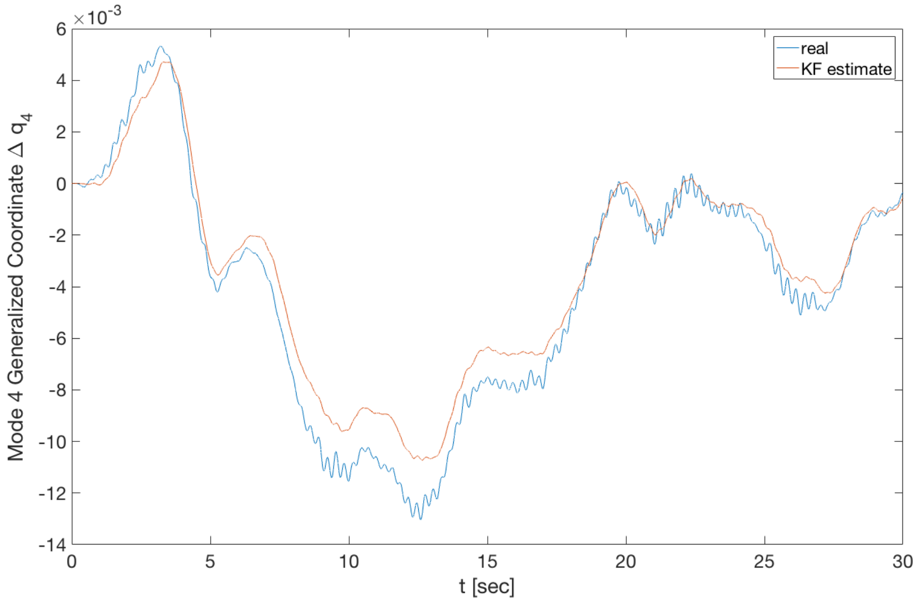

Figure C.1: Kalman filter estimation of the fourth aeroelastic mode

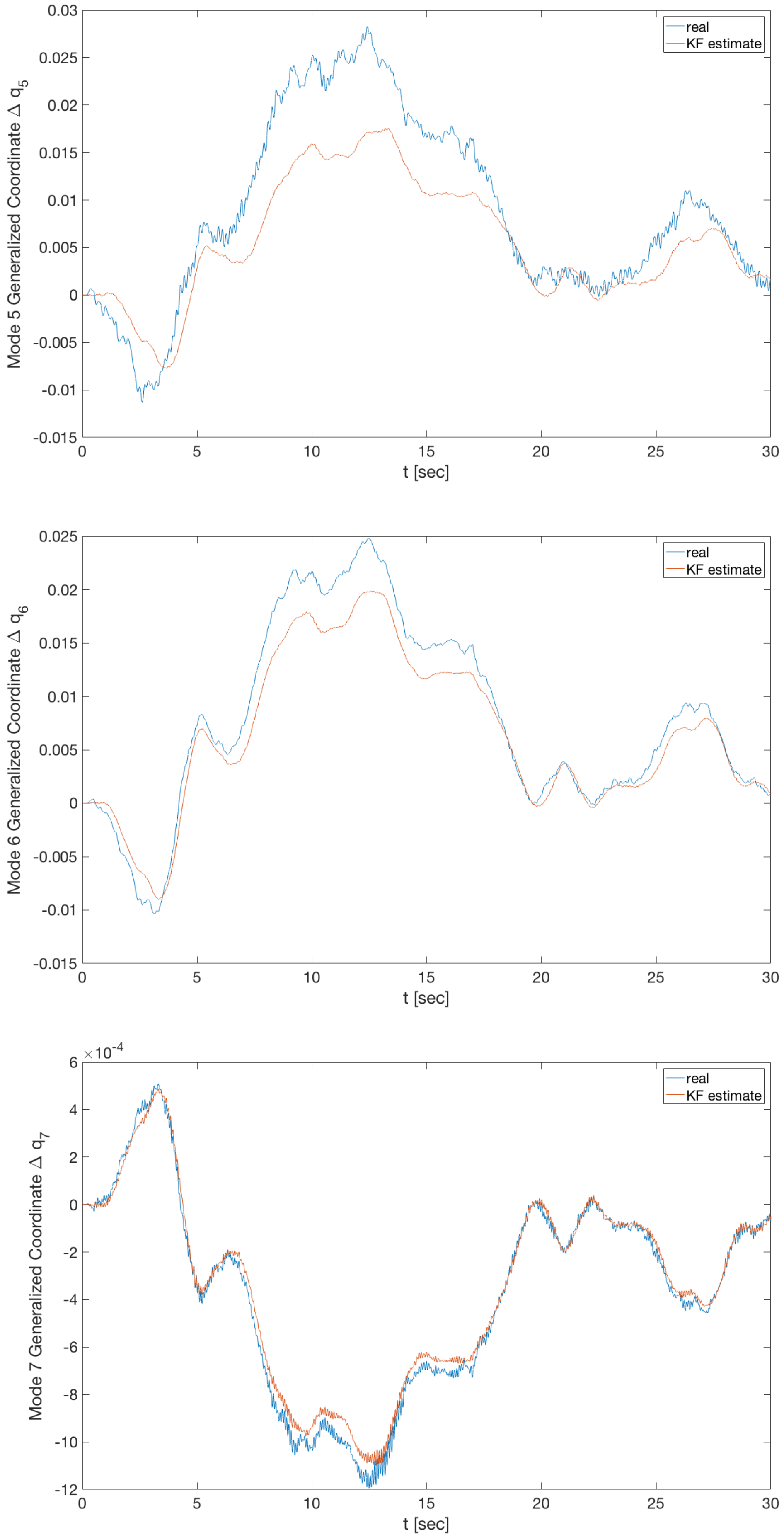

Figure C.2: Kalman filter estimation of the fifth till seventh aeroelastic mode

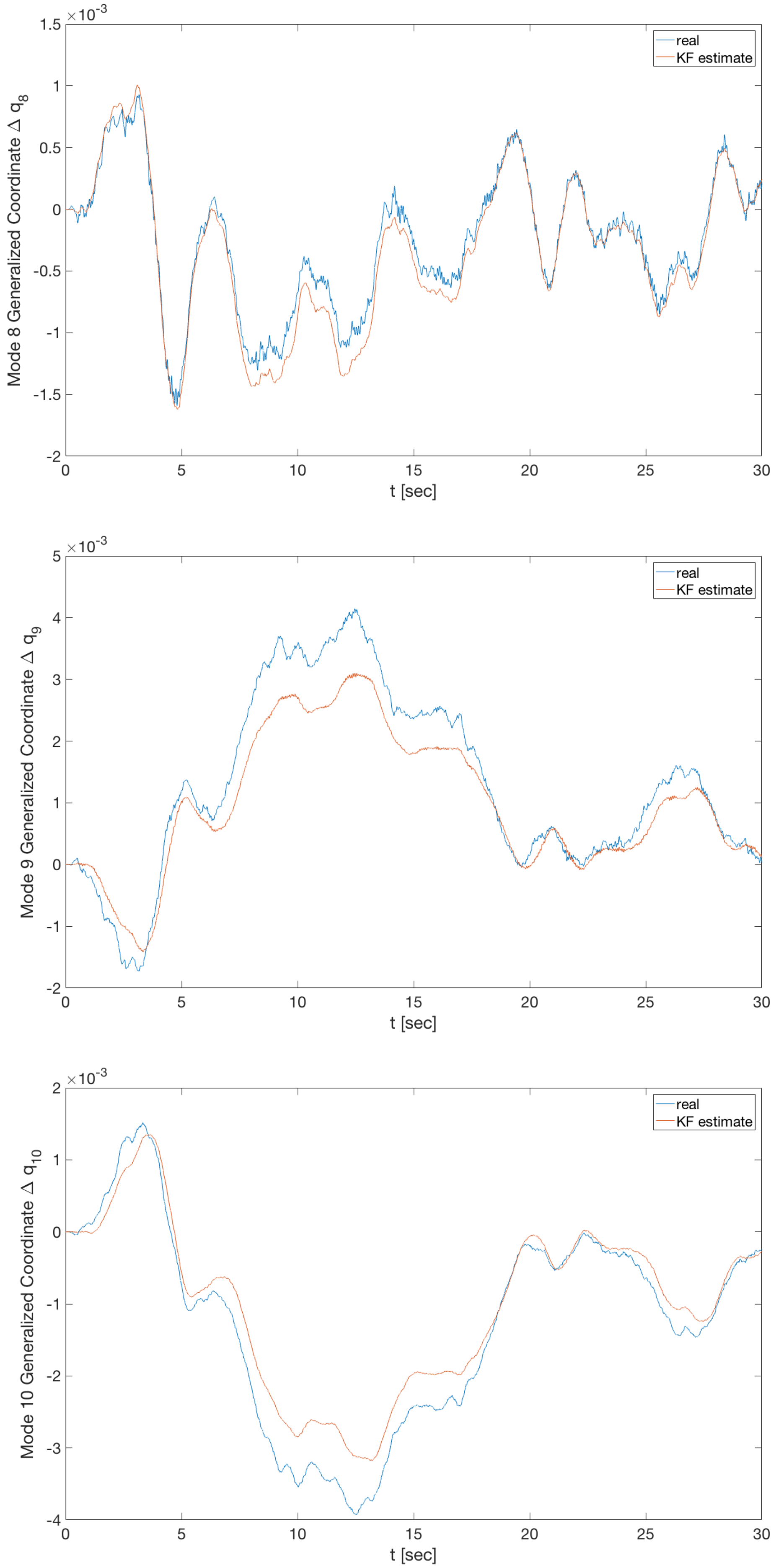

Figure C.3: Kalman filter estimation of the eighth till tenth aeroelastic mode

D

Turbulence Estimation using Extended State Observer

This appendix shows the ESO disturbance estimation results for the turbulence with respect to the pitch rate w_{g_q}, pitch angle w_{g_θ}, second aeroelastic mode $w_{g_{q2}}$, and third aeroelastic mode $w_{g_{q3}}$.

Figures D.1 and D.2 show the results for the LQR controller, which means that the aeroelastic states are assumed to be measured. Figures D.3 and D.4 show the results for the LQG controller, which uses the Kalman filter optimal estimation to estimate the aeroelastic states.

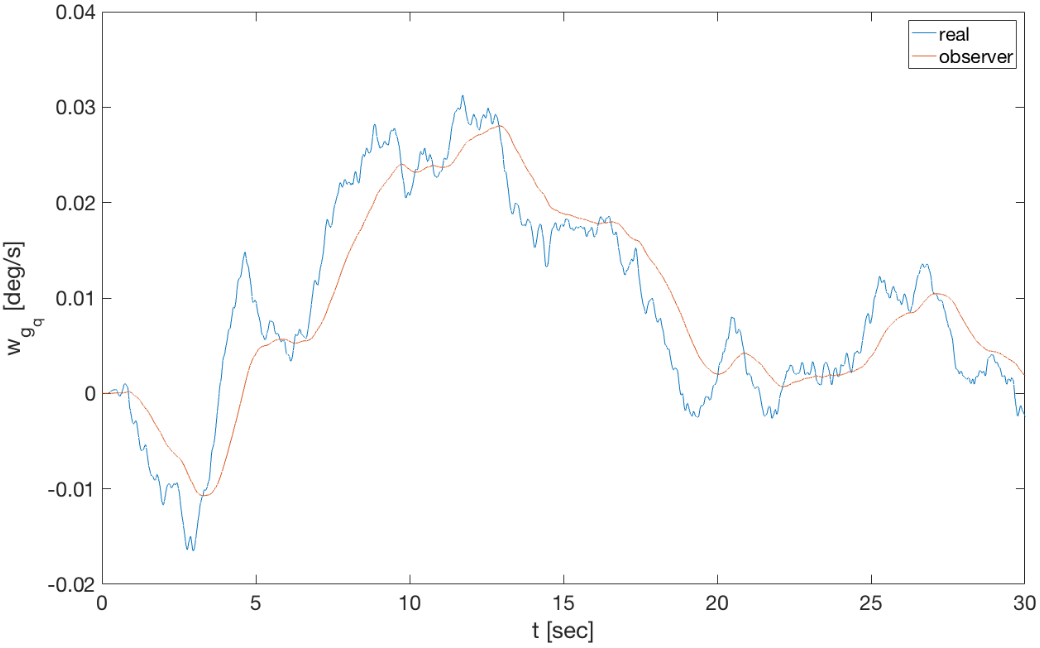

(a) Turbulence effect for pitch rate q

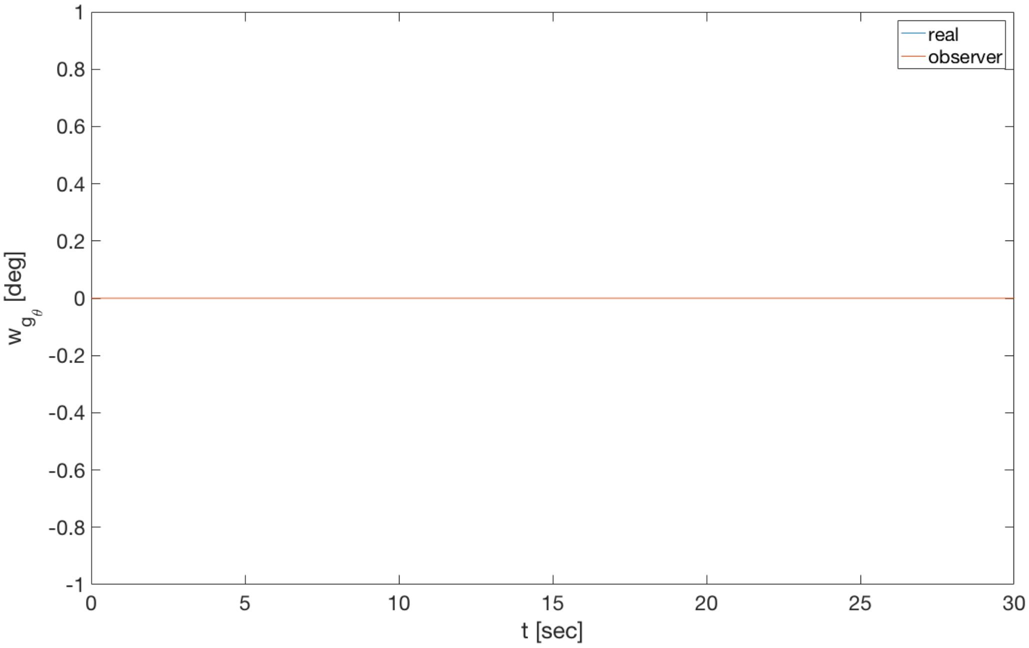

(b) Turbulence effect for pitch angle θ

Figure D.1: ESO disturbance estimation with respect to rigid-body states for LQR controller

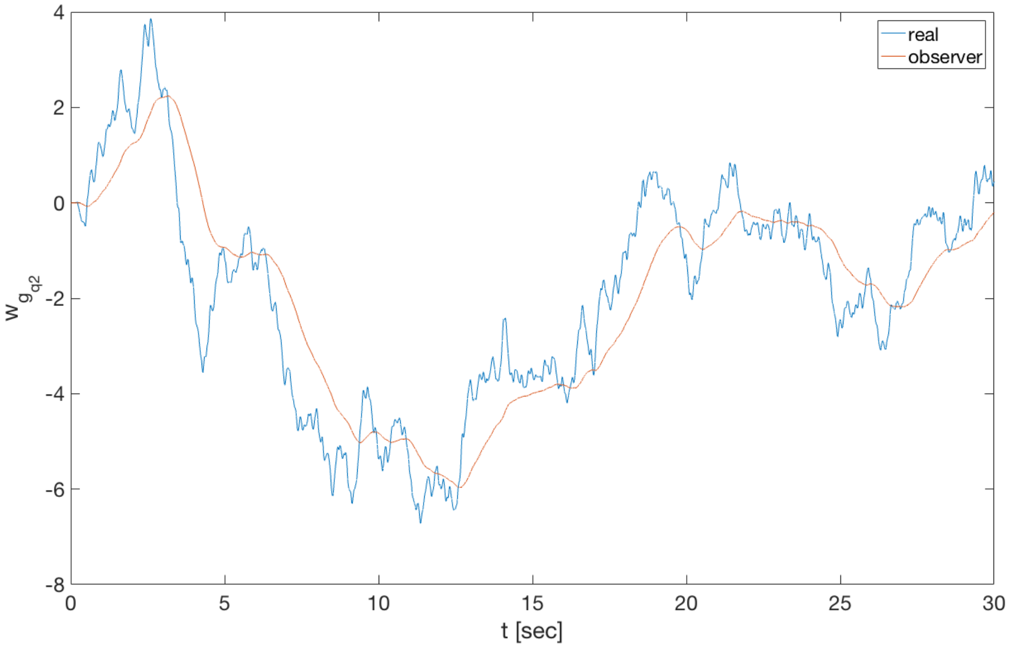

(a) Turbulence effect for second aeroelastic mode q_2

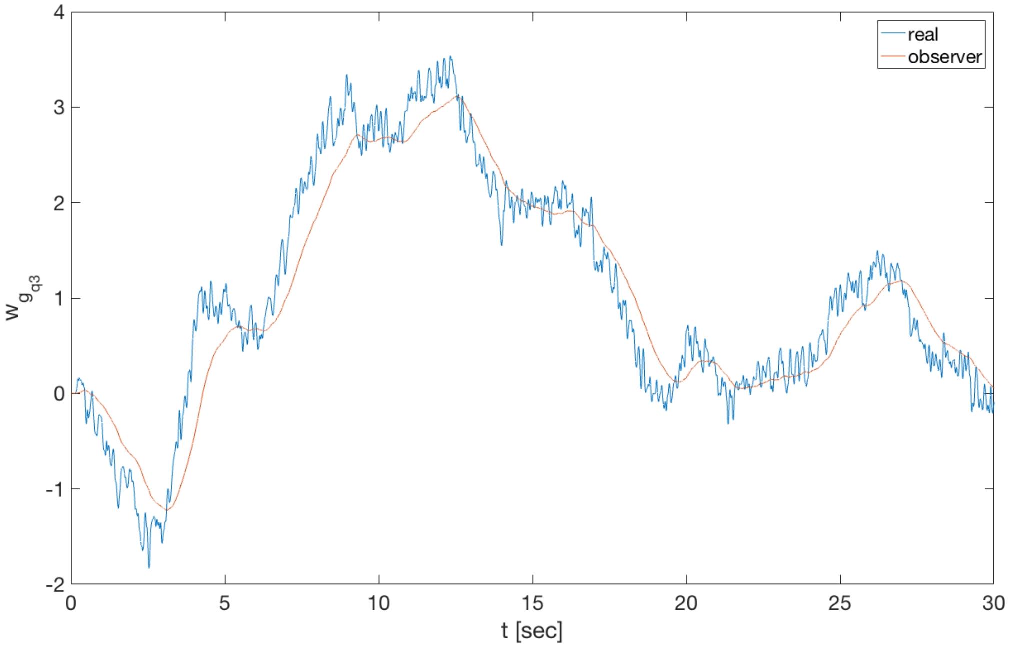

(b) Turbulence effect for third aeroelastic mode q_3

Figure D.2: ESO disturbance estimation with respect to aeroelastic states for LQR controller

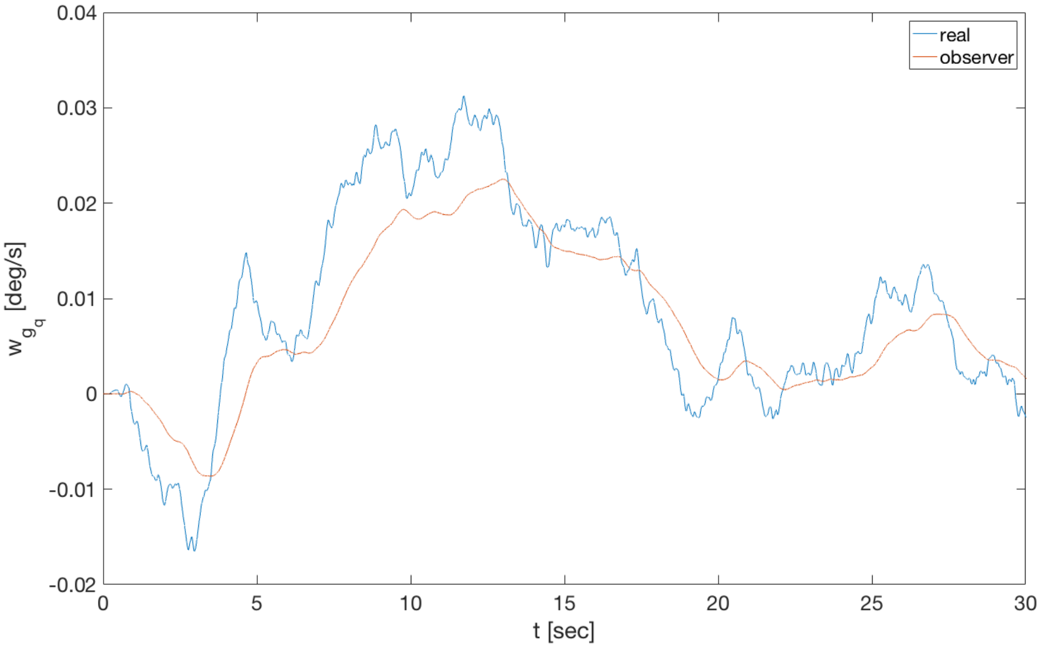

(a) Turbulence effect for pitch rate q

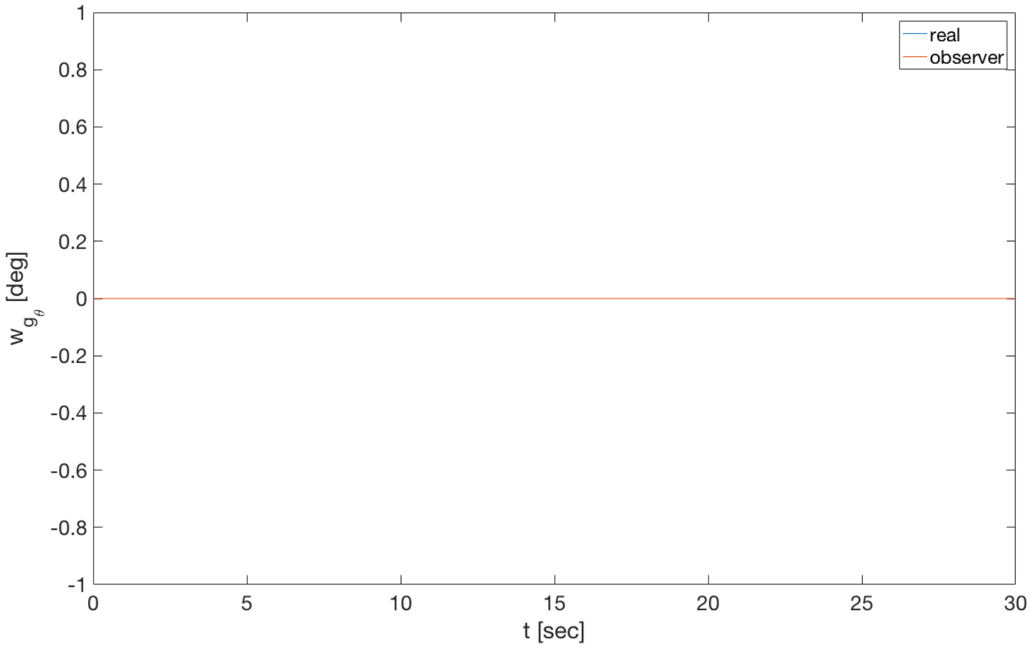

(b) Turbulence effect for pitch angle θ

Figure D.3: ESO disturbance estimation with respect to rigid-body states for LQG controller

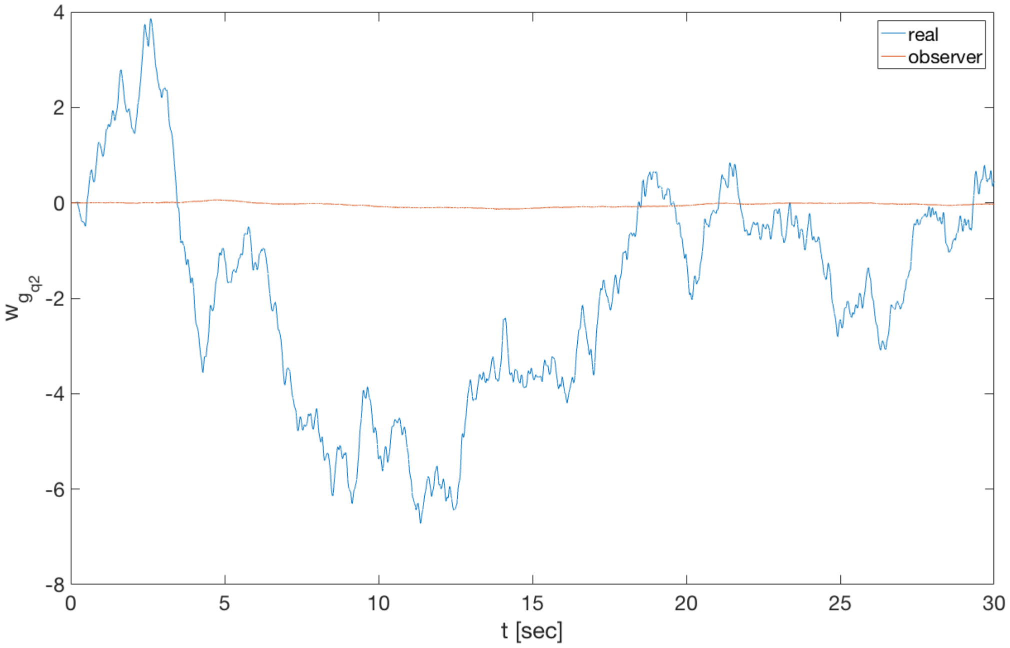

(a) Turbulence effect for second aeroelastic mode q_2

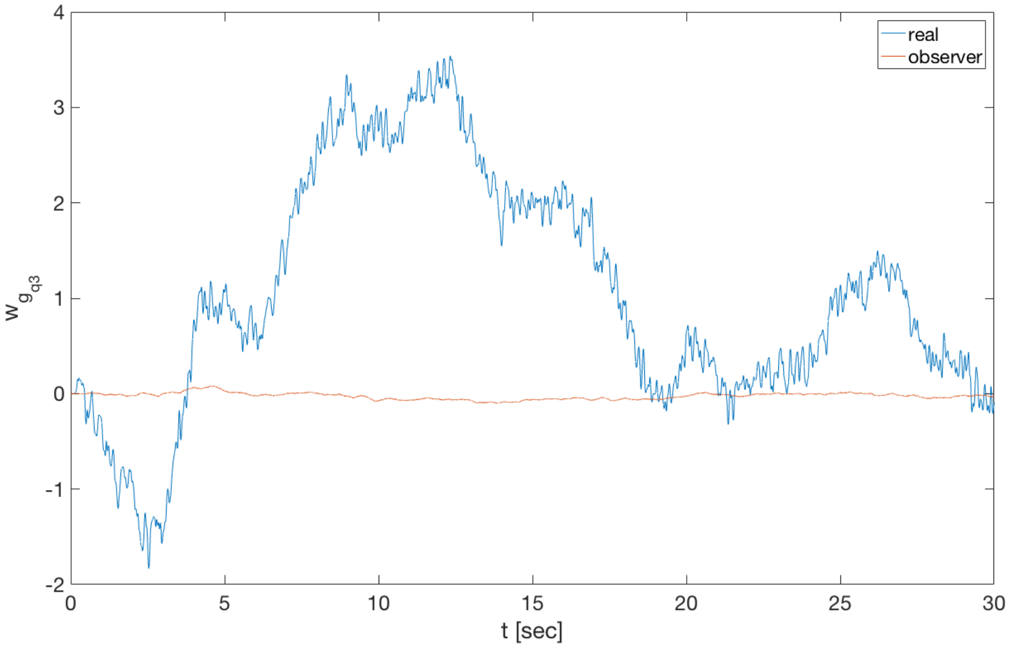

(b) Turbulence effect for third aeroelastic mode q_3

Figure D.4: ESO disturbance estimation with respect to aeroelastic states for LQG controller

E

Validation Results

This appendix shows the performance metric results for six validation runs using different turbulence models. Furthermore, the time responses of the validation discussed in chapter 10 are presented.

Dryden Light

The performance metric results with respect to the flight dynamic responses of the Dryden Light simulation run are presented in Table E.1.

Table E.1: Performance metrics results: flight dynamics responses for light Dryden turbulence

	$\sum\|\|x_r - x_{ref,r}\|\|$	%	$\sum\|\|x_e - x_{ref,e}\|\|$	%	$\|\|y - y_{ref}\|\|$	%
NRC	0.595	0	24.177	0	3.209	0
LQR	0.581	-2	25.751	7	1.716	-47
LQR + DM	0.437	- 27	21.314	-12	2.002	-38
LQR + DM + GLA	0.314	-47	9.776	-60	1.762	-45
LQG	0.437	-27	12.561	-48	2.146	-33
LQG + DM	0.350	-42	9.998	-59	2.197	-32
LQG + DM + GLA	0.173	-71	9.454	-61	2.360	-26

The performance metric results with respect to the structural and aerodynamic responses of the Dryden Light simulation run are presented in Table E.2.

Table E.2: Performance metrics results: structural and aerodynamic responses for light Dryden turbulence

	A_z [ft/s^2]	%	$M_{y,rms}$ [ft-lb]	%	ΔC_D [dragcount]	%
NRC	2.592	0	89579	0	24	0
LQR	2.613	1	68256	-24	20	-17
LQR + DM	2.485	-4	58578	-35	19	-21
LQR + DM + GLA	2.683	4	30233	-66	23	-4
LQG	2.663	3	36989	-59	18	-25
LQG + DM	2.546	-2	29721	-67	17	-29
LQG + DM + GLA	2.522	-3	17023	-81	19	-21

Figures E.1 - E.3 show the simulation responses to the Dryden Light turbulence for the LQG controller with aeroelastic mode suppression and the LQG controller with aeroelastic mode suppression and active gust load alleviation.

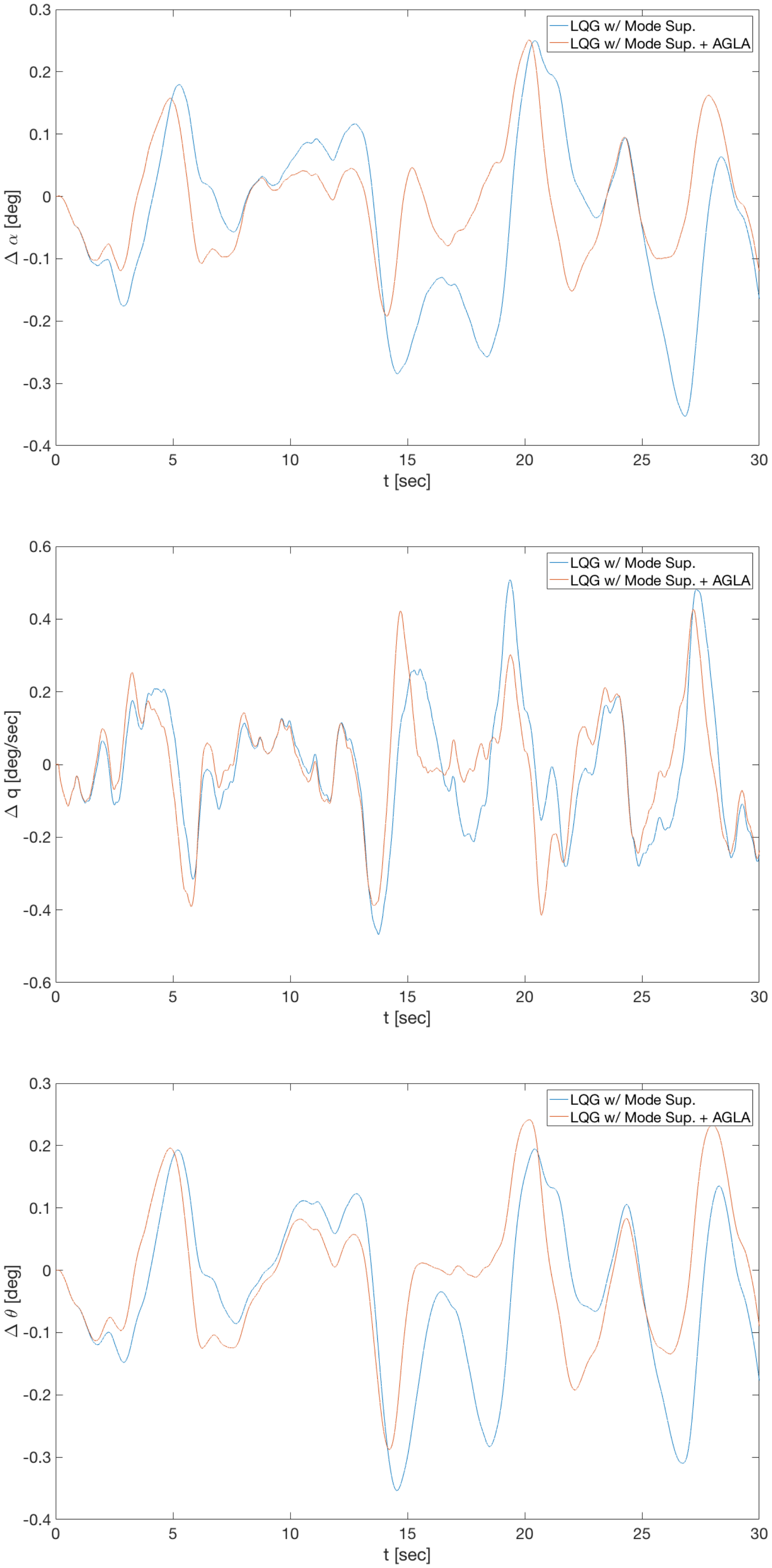

Figure E.1: Rigid-body response to light Dryden turbulence

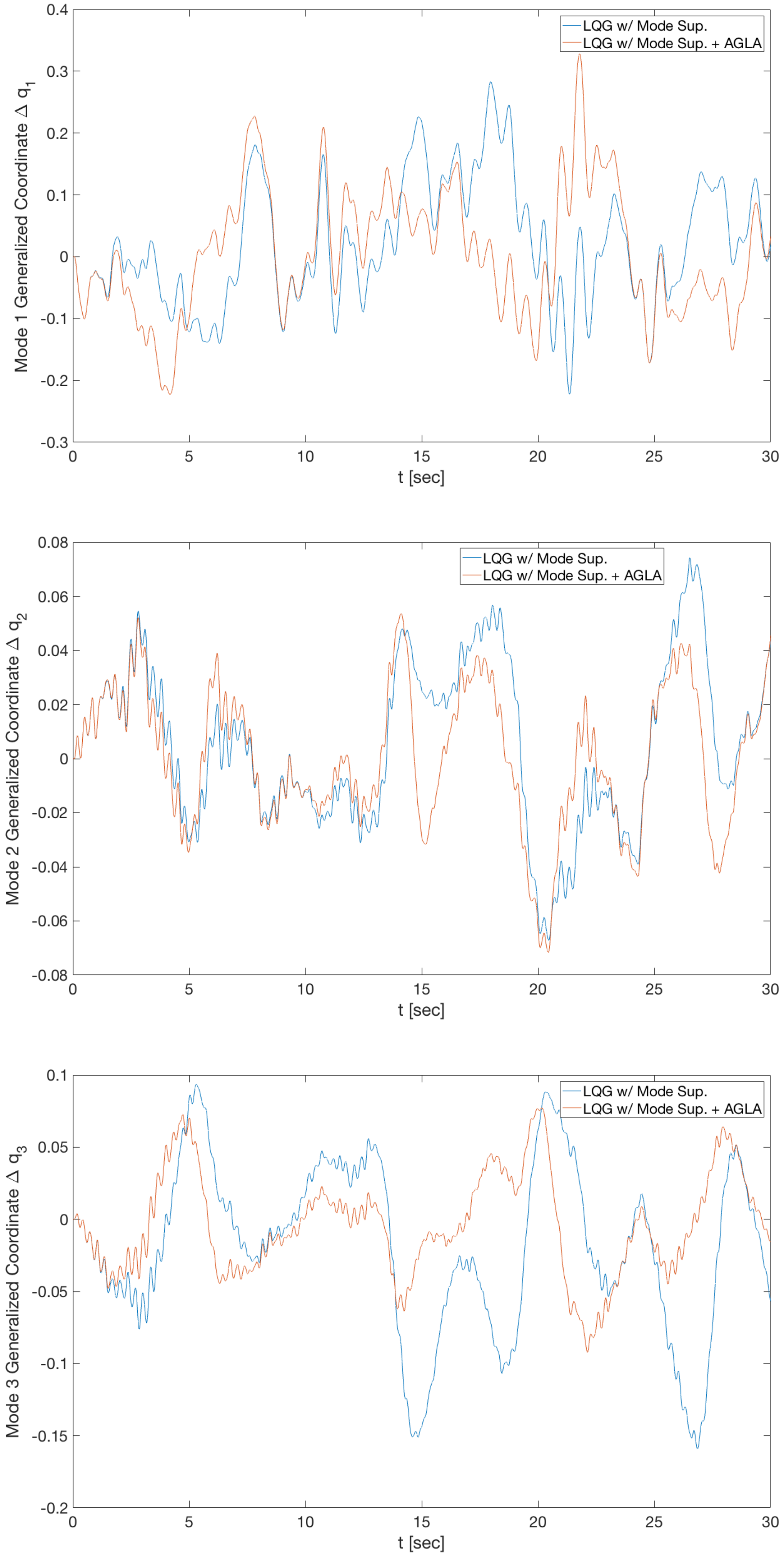

Figure E.2: Elastic response to light Dryden turbulence

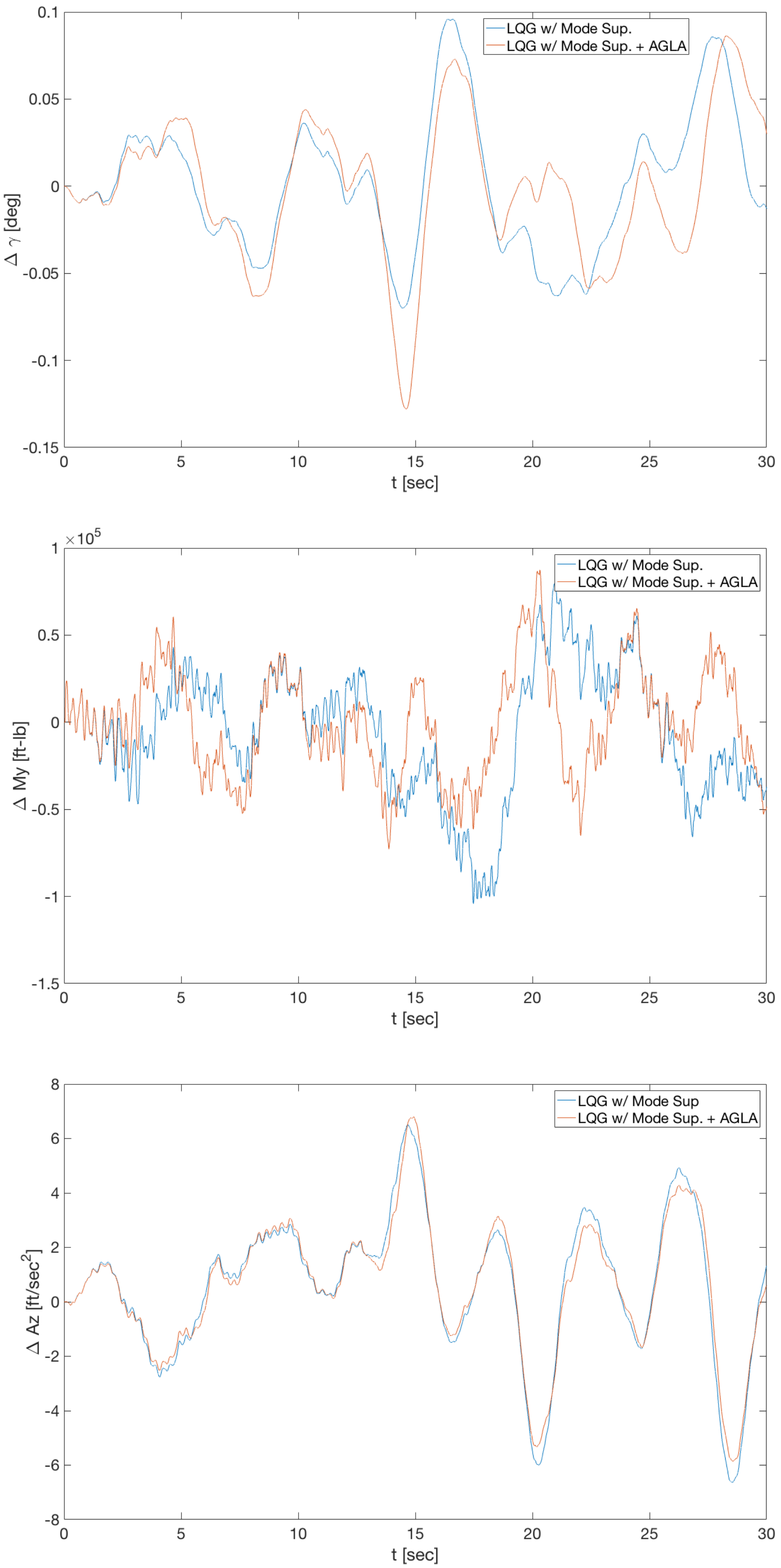

Figure E.3: Flight-path angle, structural and acceleration response to light Dryden turbulence

Dryden Moderate

The performance metric results with respect to the flight dynamic responses of the Dryden Moderate simulation run are presented in Table E.3.

Table E.3: Performance metrics results: flight dynamics responses for moderate Dryden turbulence

	$\sum\lVert x_r - x_{ref,r}\rVert$	%	$\sum\lVert x_e - x_{ref,e}\rVert$	%	$\lVert y - y_{ref}\rVert$	%
NRC	0.595	0	24.177	0	3.209	0
LQR	0.581	-2	25.751	7	1.716	-47
LQR + DM	0.437	-27	21.314	-12	2.002	-38
LQR + DM + GLA	0.314	-47	9.776	-60	1.762	-45
LQG	0.437	-27	12.562	-48	2.146	-33
LQG + DM	0.350	-41	9.998	-58	2.197	-32
LQG + DM + GLA	0.312	-46	9.454	-61	2.360	-26

The performance metric results with respect to the structural and aerodynamic responses of the Dryden Moderate simulation run are presented in Table E.4.

Table E.4: Performance metrics results: structural and aerodynamic responses for moderate Dryden turbulence

	A_z [ft/s^2]	%	$M_{y,rms}$ [ft-lb]	%	ΔC_D [dragcount]	%
NRC	2.592	0	89579	0	24	0
LQR	2.613	1	68256	-24	20	-17
LQR + DM	2.485	-4	58578	-35	19	-21
LQR + DM + GLA	2.683	4	30233	-66	23	-4
LQG	2.663	3	36989	-59	18	-25
LQG + DM	2.530	-2	32705	-63	17	-29
LQG + DM + GLA	2.522	-3	29721	-67	19	-21

Figures E.4 - E.6 show the simulation responses to the Dryden Moderate turbulence for the LQG controller with aeroelastic mode suppression and the LQG controller with aeroelastic mode suppression and active gust load alleviation.

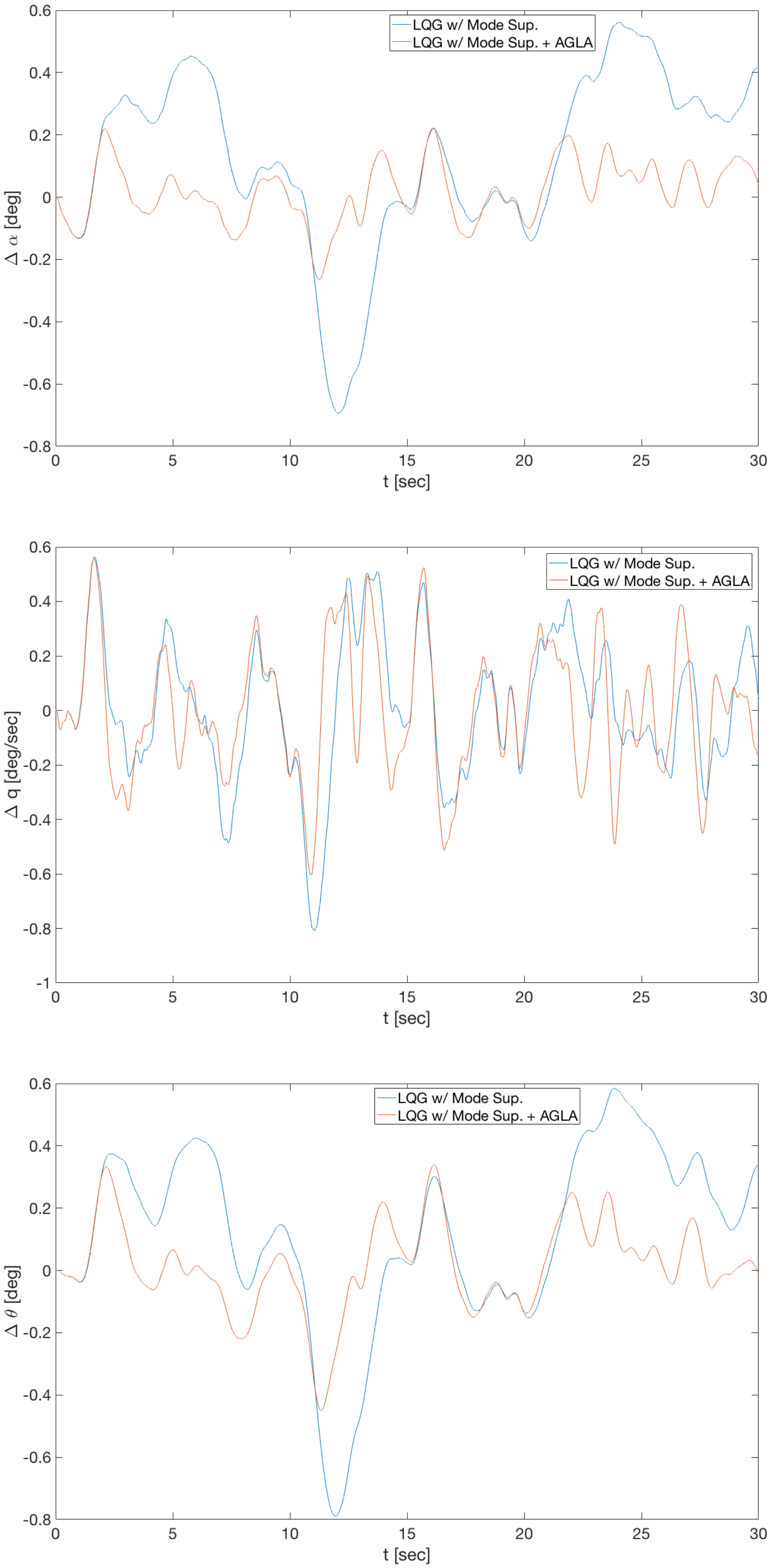

Figure E.4: Rigid-body response to moderate Dryden turbulence

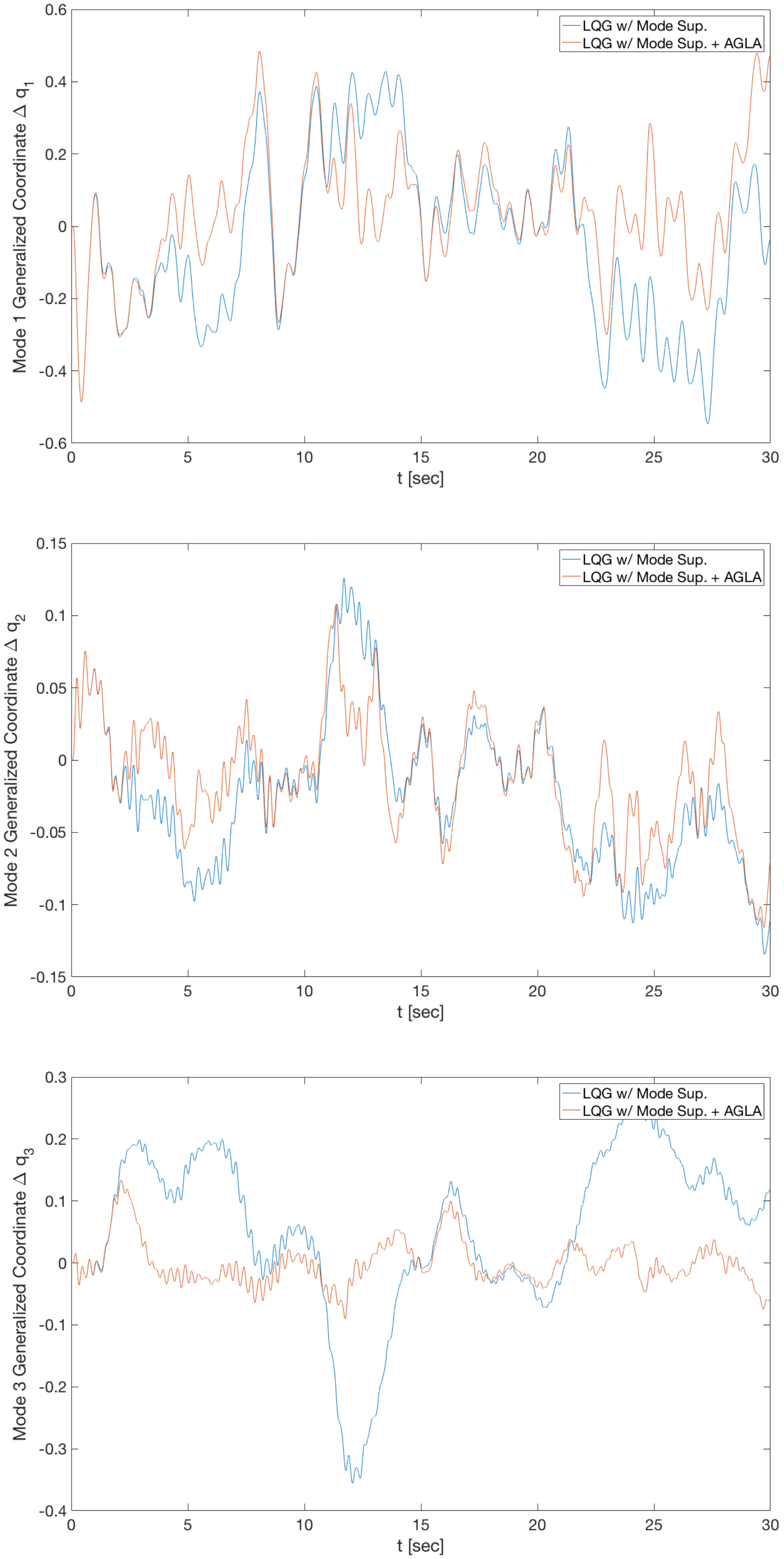

Figure E.5: Elastic response to moderate Dryden turbulence

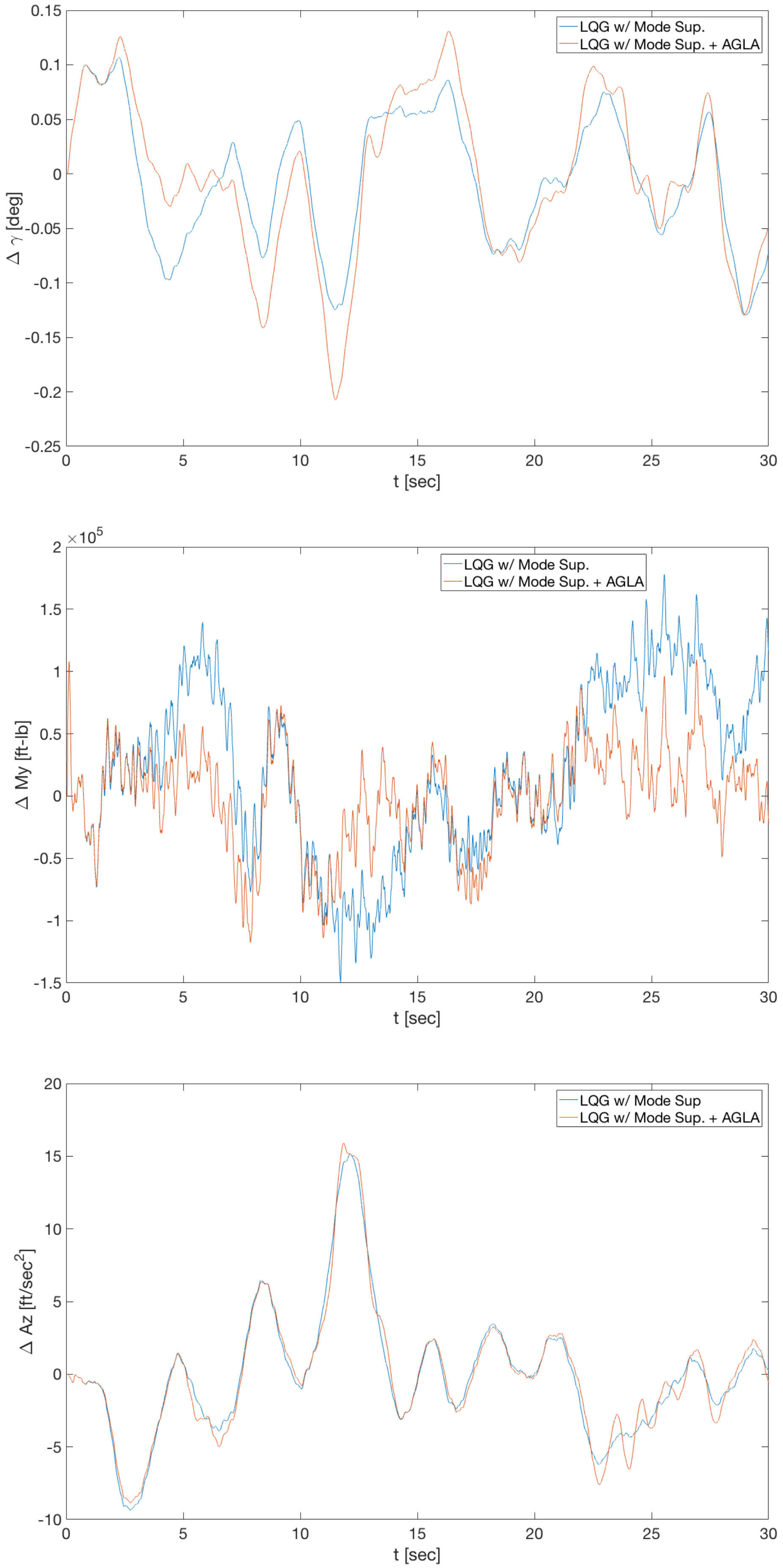

Figure E.6: Flight-path angle, structural and acceleration response to moderate Dryden turbulence

Dryden Severe

The performance metric results with respect to the flight dynamic responses of the Dryden Severe simulation run are presented in Table E.5.

Table E.5: Performance metrics results: flight dynamics responses for severe Dryden turbulence

	$\sum\|\|x_r - x_{ref,r}\|\|$	%	$\sum\|\|x_e - x_{ref,e}\|\|$	%	$\|\|y - y_{ref}\|\|$	%
NRC	0.595	0	24.177	0	3.209	0
LQR	0.581	-2	25.751	7	1.716	-47
LQR + DM	0.437	-27	12.562	-48	2.146	-33
LQR + DM + GLA	0.314	-47	9.776	-60	1.762	-45
LQG	0.437	-27	12.562	-48	2.146	-33
LQG + DM	0.173	-71	4.180	-83	1.025	-68
LQG + DM + GLA	0.312	-48	9.454	-61	2.360	-26

The performance metric results with respect to the structural and aerodynamic responses of the Dryden Severe simulation run are presented in Table E.6.

Table E.6: Performance metrics results: structural and aerodynamic responses for severe Dryden turbulence

	A_z [ft/s^2]	%	$M_{y,rms}$ [ft-lb]	%	ΔC_D [dragcount]	%
NRC	2.592	0	89579	0	24	0
LQR	2.613	1	68256	-24	20	-17
LQR + DM	2.485	-4	58578	-35	19	-21
LQR + DM + GLA	2.683	4	30233	-66	23	-4
LQG	2.613	1	36989	-59	18	-25
LQG + DM	2.530	-2	32705	-63	17	-29
LQG + DM + GLA	2.522	-3	29721	-67	19	-21

Figures E.7 - E.9 show the simulation responses to the Dryden Severe turbulence for the LQG controller with aeroelastic mode suppression and the LQG controller with aeroelastic mode suppression and active gust load alleviation.

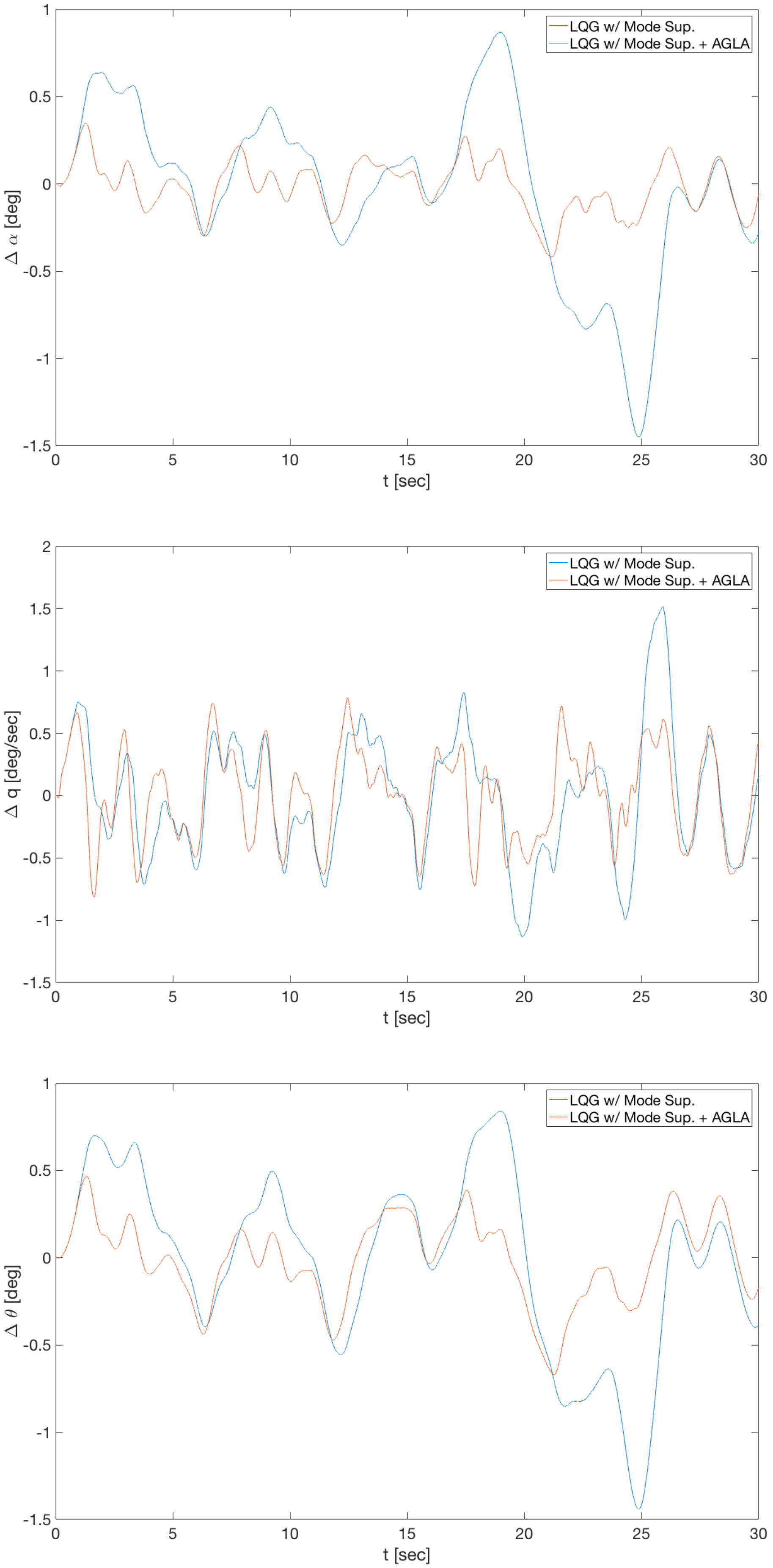

Figure E.7: Rigid-body response to severe Dryden turbulence

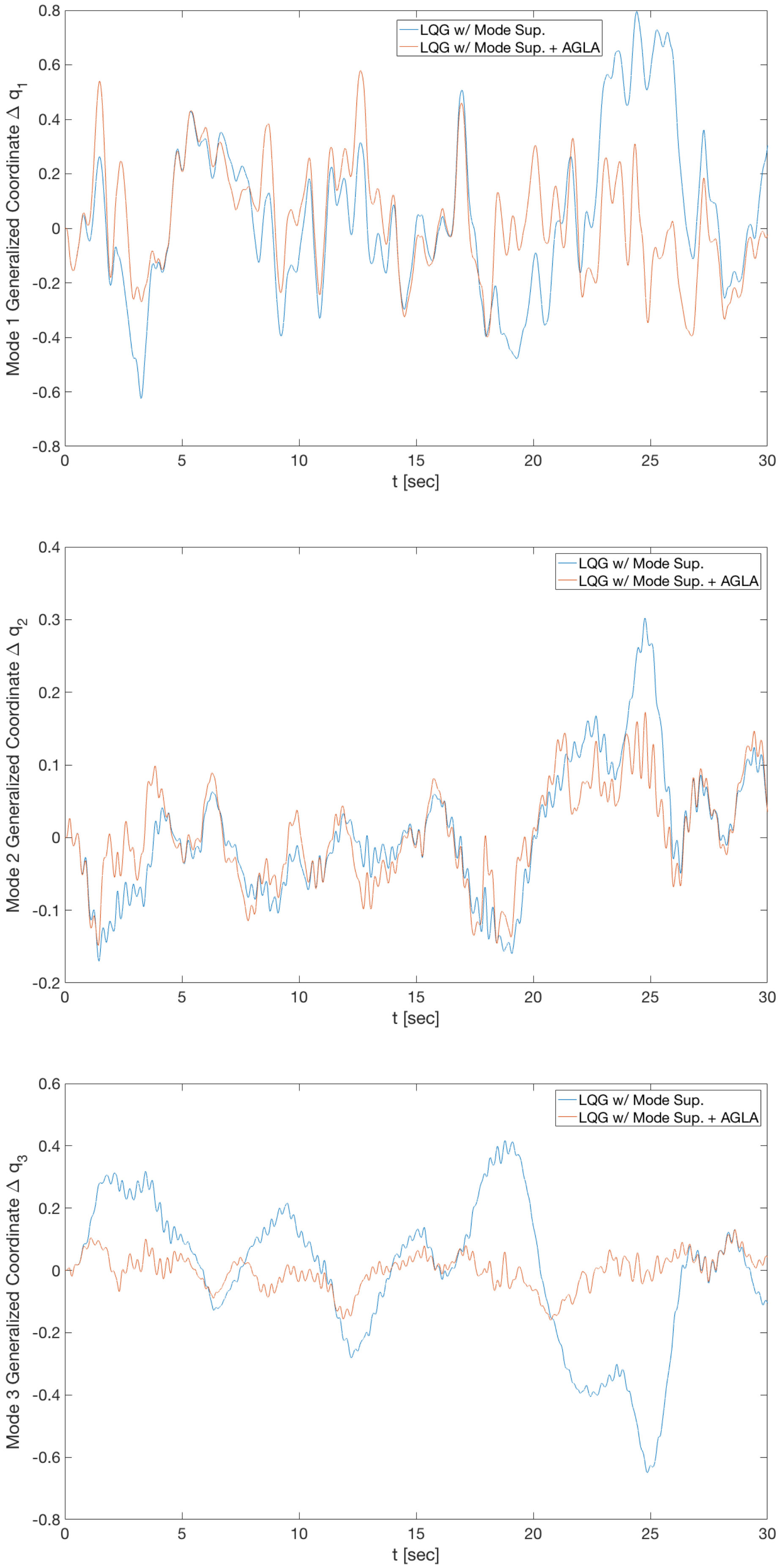

Figure E.8: Elastic response to severe Dryden turbulence

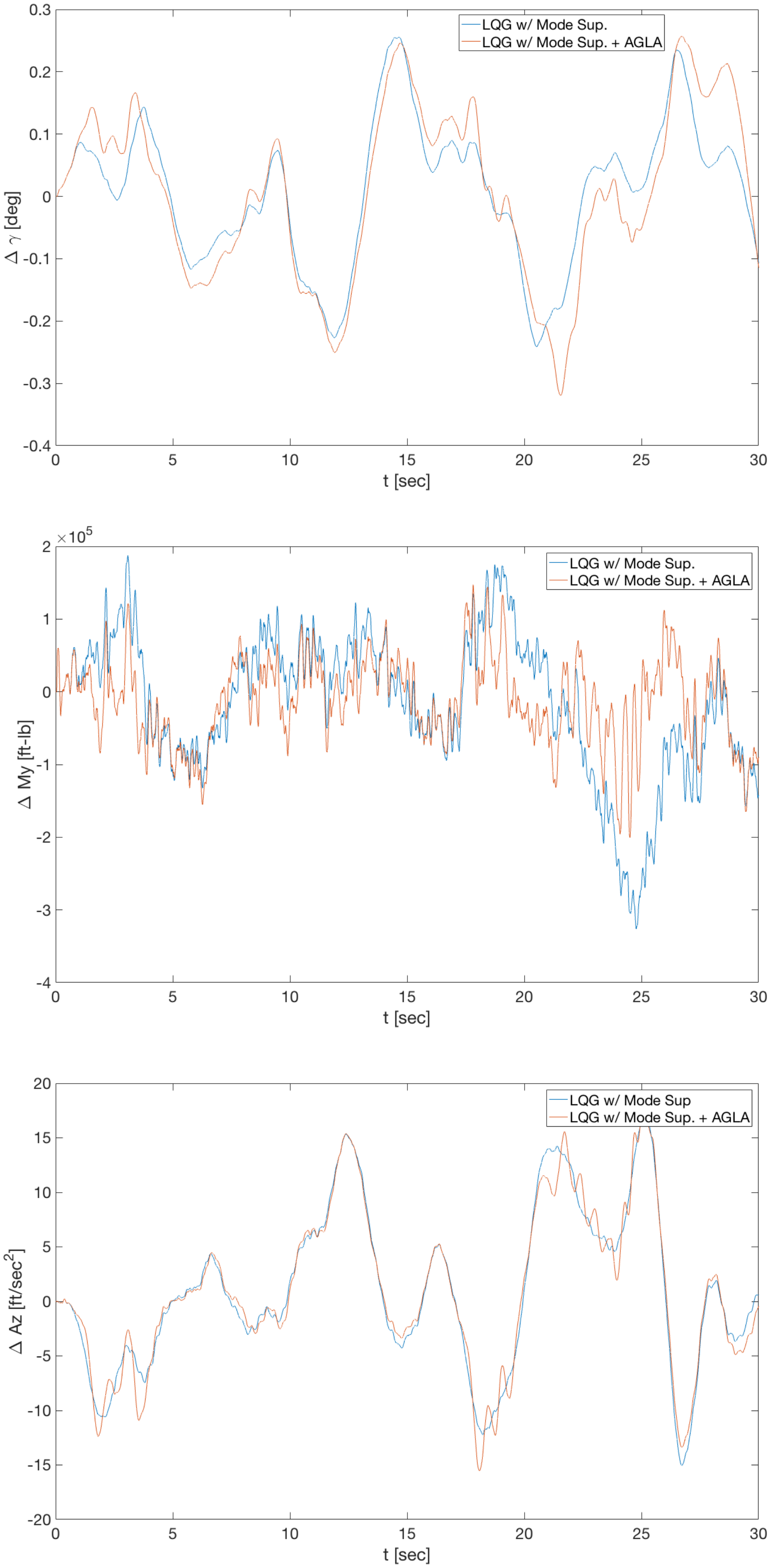

Figure E.9: Flight-path angle, structural and acceleration response to severe Dryden turbulence

von Kármán Light

The performance metric results with respect to the flight dynamic responses of the von Kármán Light simulation run are presented in Table E.7.

Table E.7: Performance metrics results: flight dynamics responses for light von Kármán turbulence

	$\sum\|\|x_r - x_{ref,r}\|\|$	%	$\sum\|\|x_e - x_{ref,e}\|\|$	%	$\|\|y - y_{ref}\|\|$	%
NRC	0.462	0	19.382	0	2.255	0
LQR	0.419	-9	21.501	11	1.268	-44
LQR + DM	0.312	-32	17.812	-8	1.547	-31
LQR + DM + GLA	0.272	-41	8.409	-57	1.547	-31
LQG	0.415	-10	14.014	-28	1.612	-29
LQG + DM	0.320	-31	10.243	-47	1.931	-14
LQG + DM + GLA	0.266	-42	8.119	-58	1.865	-17

The performance metric results with respect to the structural and aerodynamic responses of the von Kármán Light simulation run are presented in Table E.8.

Table E.8: Performance metrics results: structural and aerodynamic responses for light von Kármán turbulence

	A_z [ft/s^2]	%	$M_{y,rms}$ [ft-lb]	%	ΔC_D [dragcount]	%
NRC	2.176	0	66447	0	17	0
LQR	2.217	2	56861	-14	16	-6
LQR + DM	2.183	0	47259	-29	16	-6
LQR + DM + GLA	2.261	4	25618	-61	19	12
LQG	2.181	0	35637	-46	15	-12
LQG + DM	2.244	3	23724	-64	14	-18
LQG + DM + GLA	2.200	1	16305	-75	17	0

Figures E.10 - E.12 show the simulation responses to the von Kármán Light turbulence for the LQG controller with aeroelastic mode suppression and the LQG controller with aeroelastic mode suppression and active gust load alleviation.

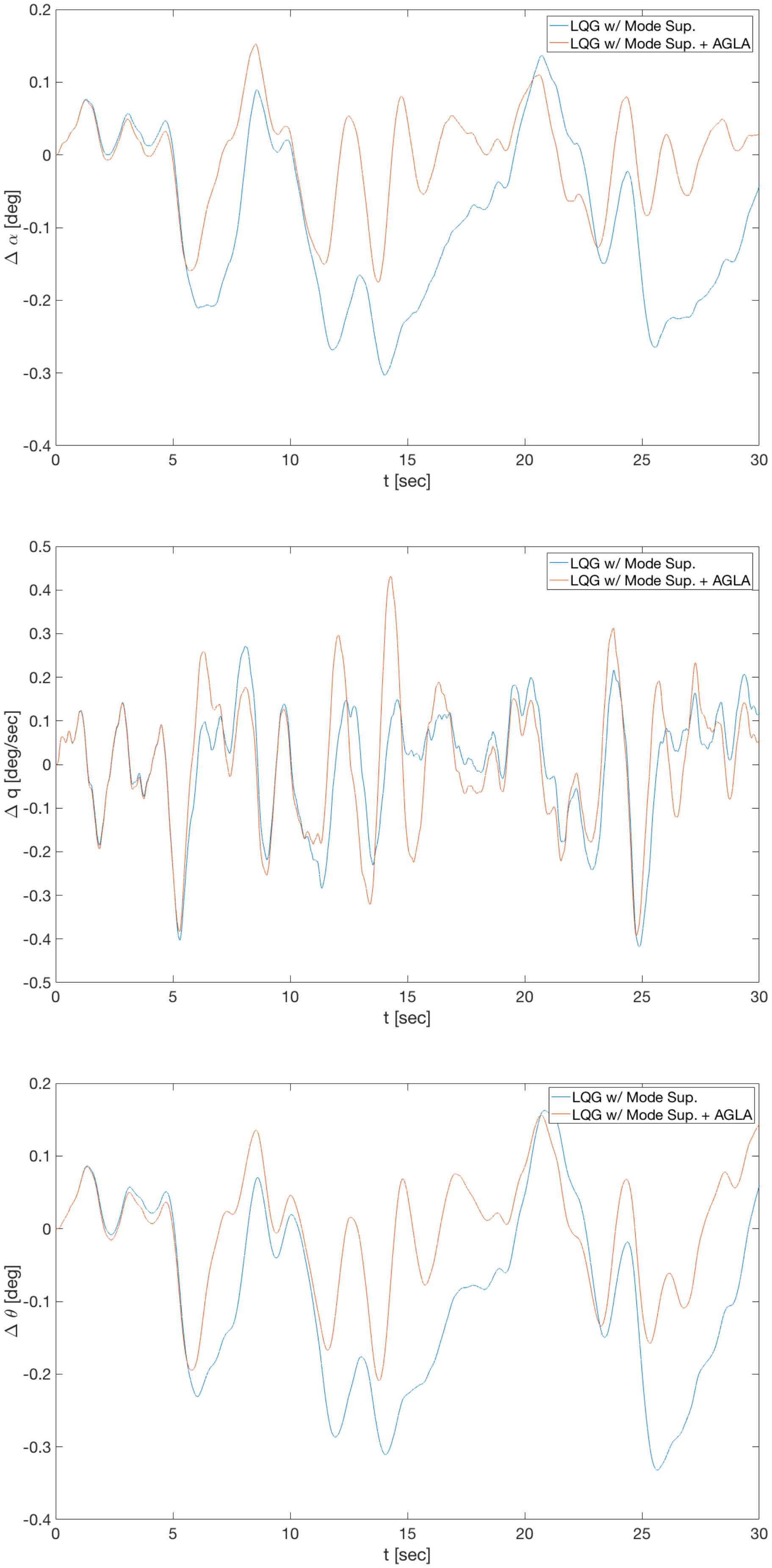

Figure E.10: Rigid-body response to light von Kármán turbulence

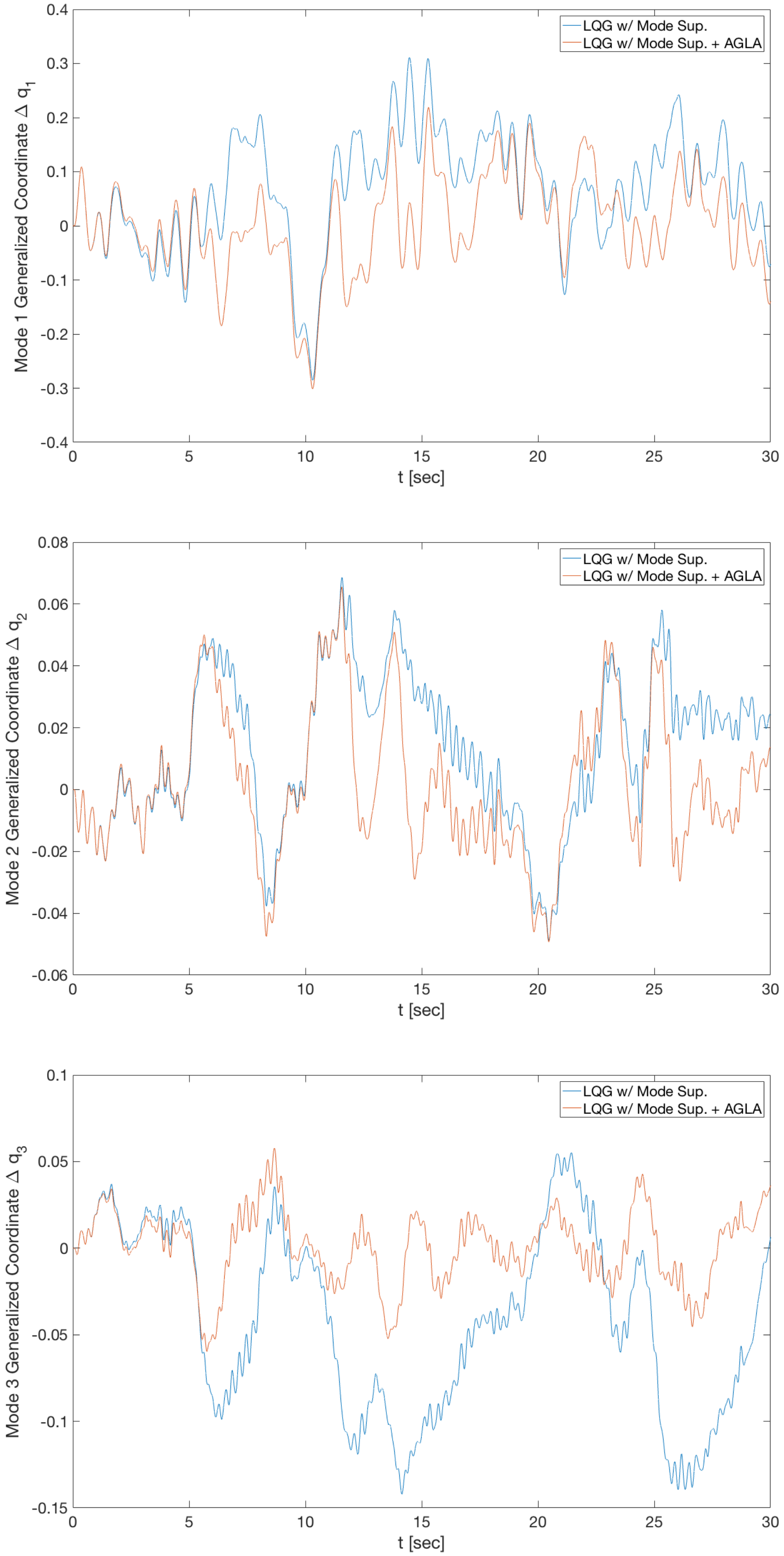

Figure E.11: Elastic response to light von Kármán turbulence

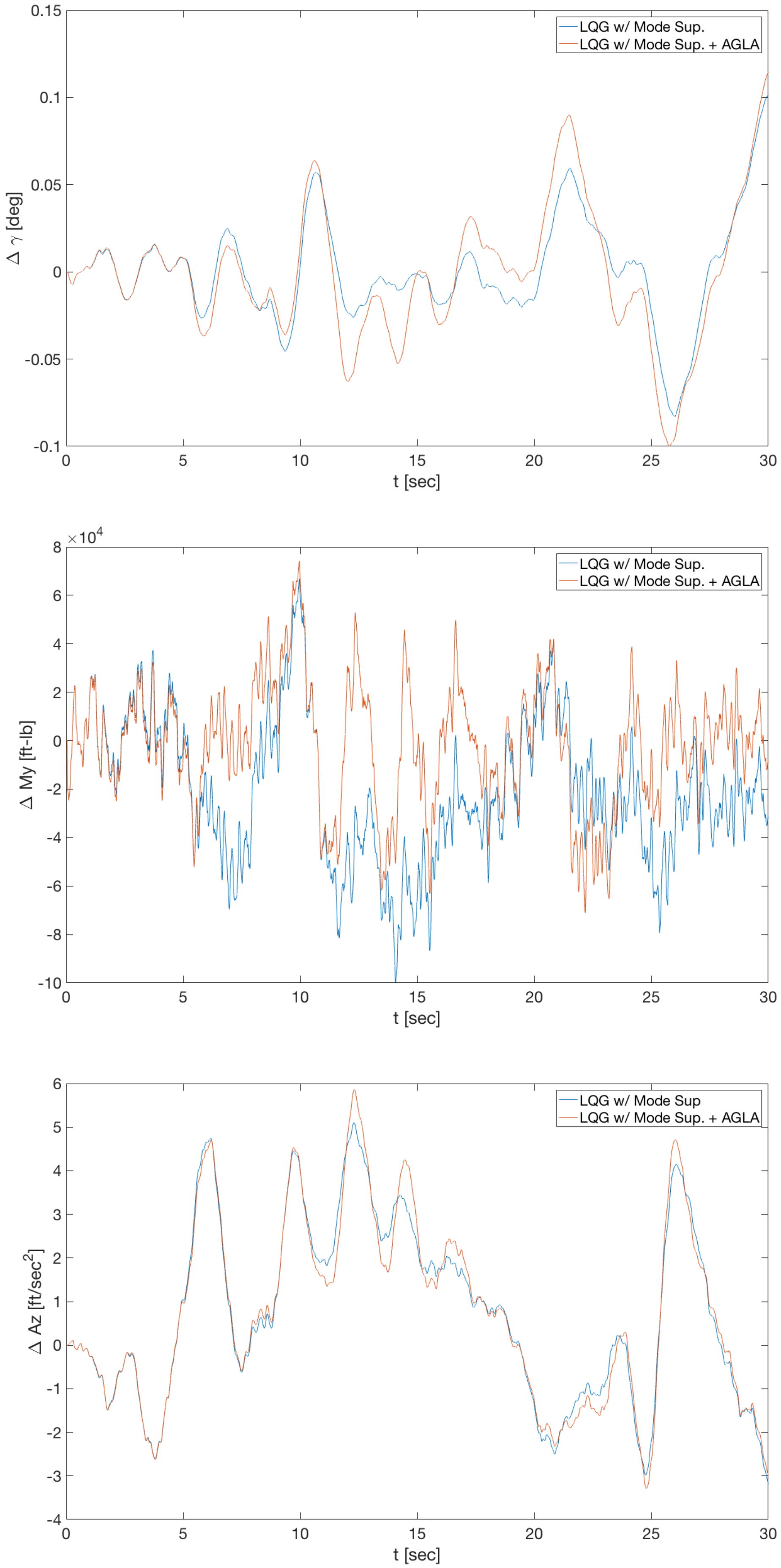

Figure E.12: Flight-path angle, structural and acceleration response to light von Kármán turbulence

von Kármán Moderate

The performance metric results with respect to the flight dynamic responses of the von Kármán Moderate simulation run are presented in Table E.9.

Table E.9: Performance metrics results: flight dynamics responses for moderate von Kármán turbulence

	$\sum\|\|x_r - x_{ref,r}\|\|$	%	$\sum\|\|x_e - x_{ref,e}\|\|$	%	$\|\|y - y_{ref}\|\|$	%
NRC	1.146	0	51.701	0	5.556	0
LQR	1.197	4	46.722	-10	3.566	-36
LQR + DM	0.850	-26	35.476	-31	5.280	-5
LQR + DM + GLA	0.528	-54	14.841	-71	3.725	-33
LQG	1.203	5	40.358	-22	4.114	-26
LQG + DM	0.861	-25	26.380	-49	5.514	-1
LQG + DM + GLA	0.590	-49	18.745	-64	5.431	-2

The performance metric results with respect to the structural and aerodynamic responses of the von Kármán Moderate simulation run are presented in Table E.10.

Table E.10: Performance metrics results: structural and aerodynamic responses for moderate von Kármán turbulence

	A_z [ft/s^2]	%	$M_{y,rms}$ [ft-lb]	%	ΔC_D [dragcount]	%
NRC	5.424	0	169176	0	39	0
LQR	5.318	-2	117393	-31	43	-31
LQR + DM	5.295	-2	89412	-47	41	-47
LQR + DM + GLA	5.436	0	49454	-71	45	-71
LQG	5.365	-1	115709	-32	35	-32
LQG + DM	5.331	-2	82471	-51	34	-51
LQG + DM + GLA	5.421	0	46021	-73	43	-73

Figures E.13 - E.15 show the simulation responses to the von Kármán Moderate turbulence for the LQG controller with aeroelastic mode suppression and the LQG controller with aeroelastic mode suppression and active gust load alleviation.

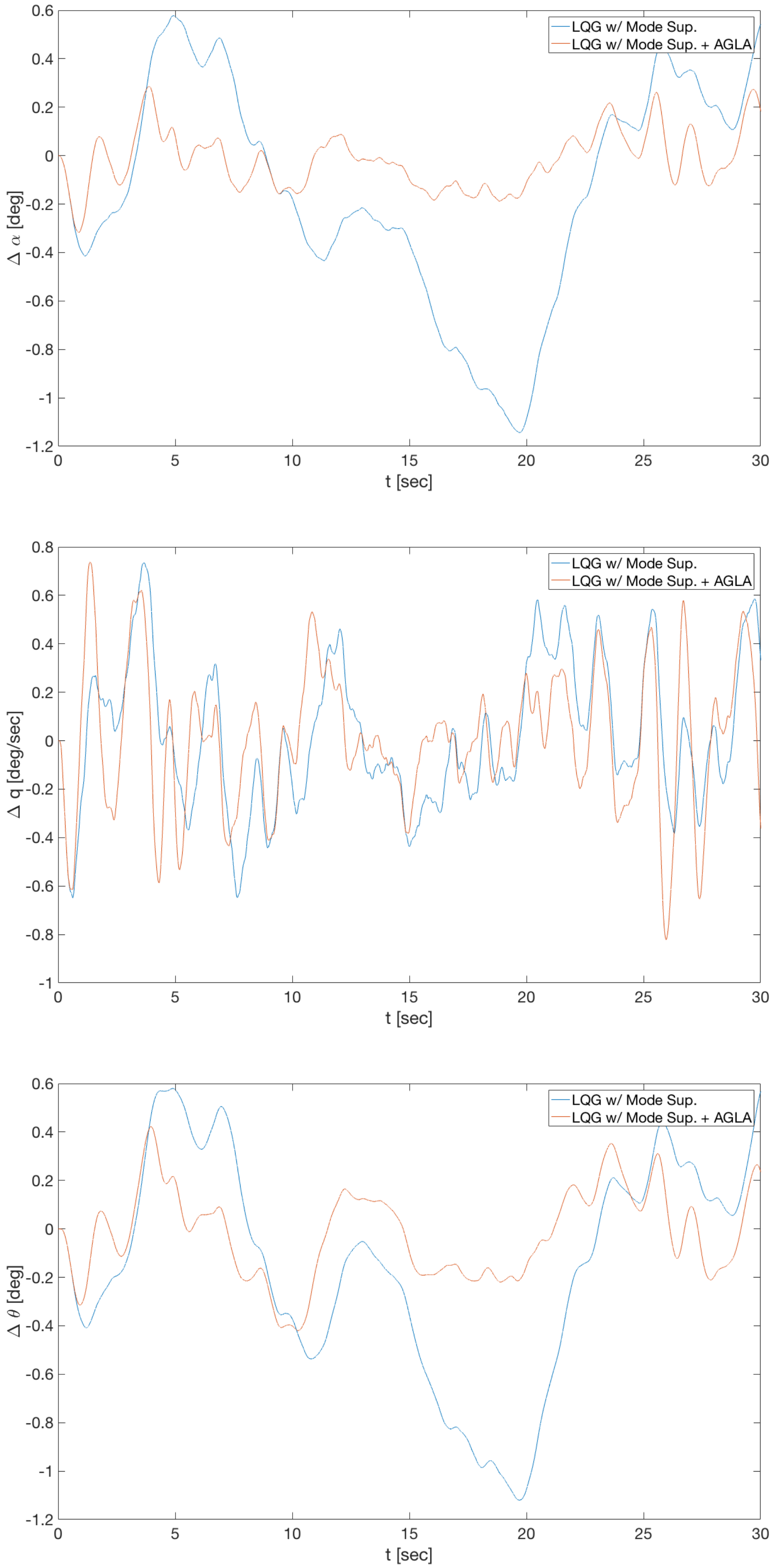

Figure E.13: Rigid-body response to moderate von Kármán turbulence

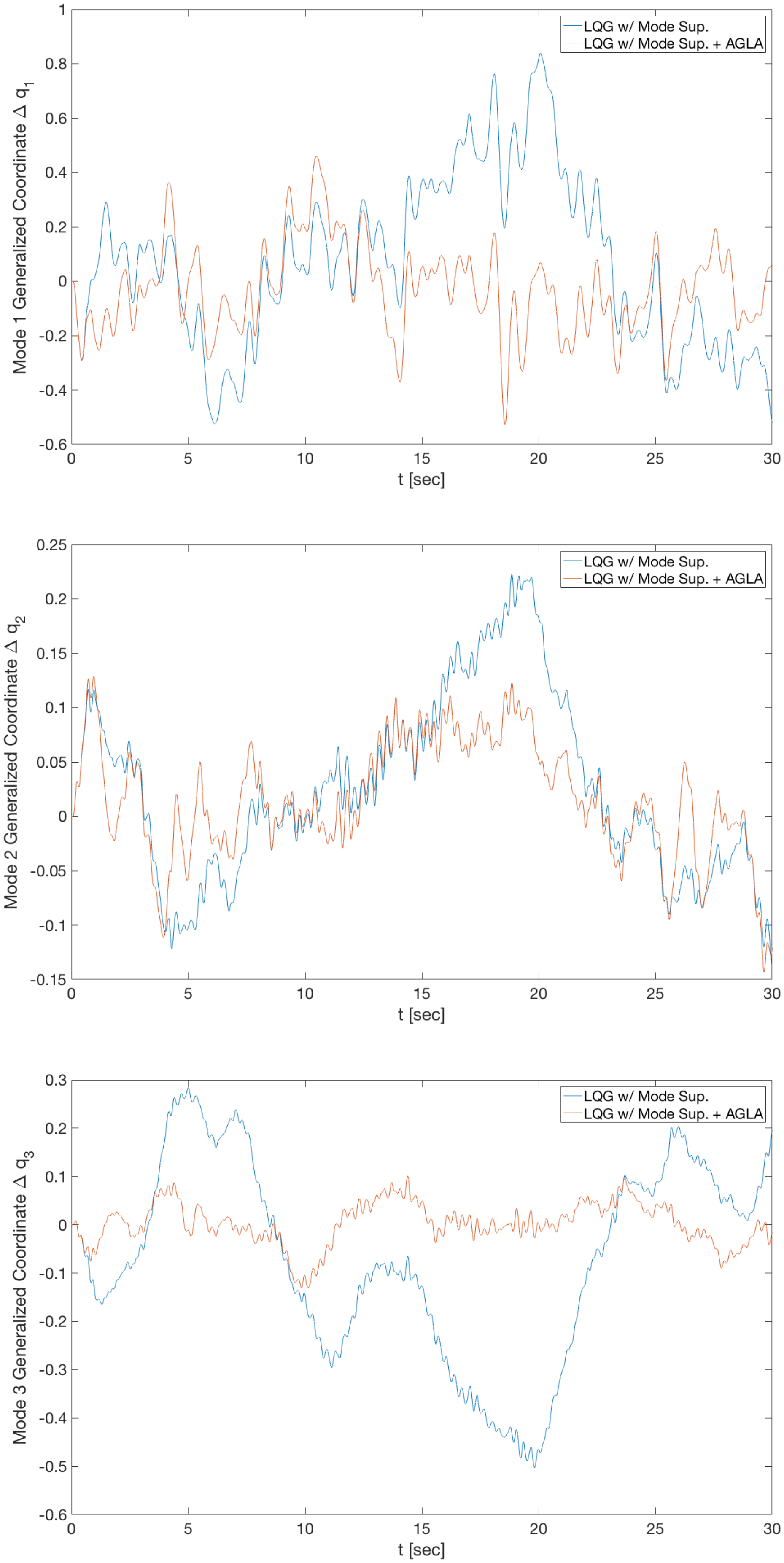

Figure E.14: Elastic response to moderate von Kármán turbulence

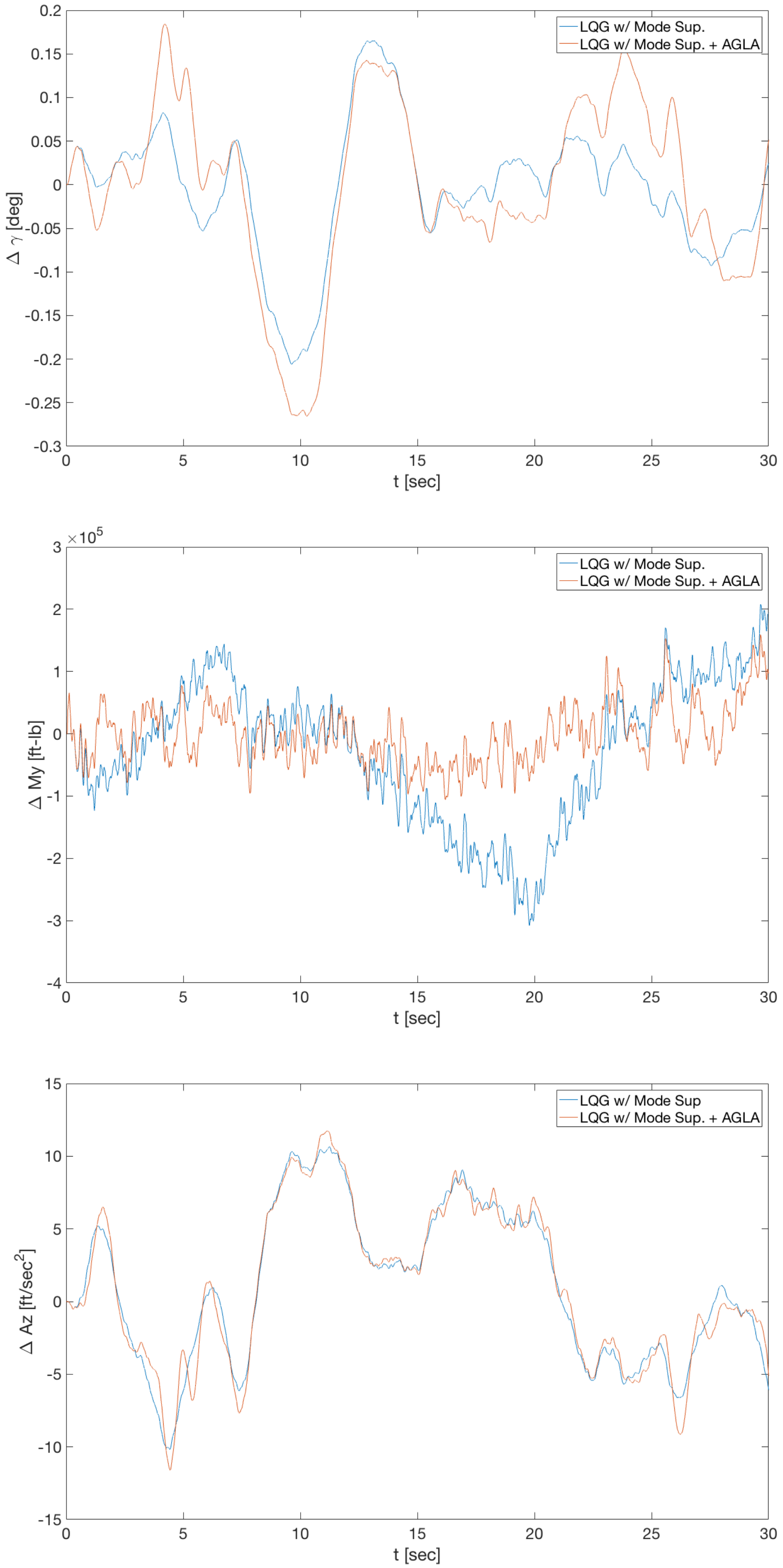

Figure E.15: Flight-path angle, structural and acceleration response to moderate von Kármán turbulence

Von Kármán Severe

The performance metric results with respect to the flight dynamic responses of the von Kármán Severe simulation run are presented in Table E.11.

Table E.11: Performance metrics results: flight dynamics responses for severe von Kármán turbulence

	$\sum\|\|x_r - x_{ref,r}\|\|$	%	$\sum\|\|x_e - x_{ref,e}\|\|$	%	$\|\|y - y_{ref}\|\|$	%
NRC	1.181	0	55.387	0	8.168	0
LQR	1.324	12	59.216	7	4.864	-40
LQR + DM	0.960	-19	45.838	-17	5.949	-27
LQR + DM + GLA	0.549	-54	18.853	-66	4.125	-49
LQG	1.132	-4	40.268	-27	6.532	-20
LQG + DM	0.858	-27	29.776	-46	7.420	-9
LQG + DM + GLA	0.642	-46	22.925	-59	6.092	-25

The performance metric results with respect to the structural and aerodynamic responses of the von Kármán Severe simulation run are presented in Table E.12.

Table E.12: Performance metrics results: structural and aerodynamic responses for severe von Kármán turbulence

	A_z [ft/s^2]	%	$M_{y,rms}$ [ft-lb]	%	ΔC_D [dragcount]	%
NRC	4.896	0	199224	0	61	0
LQR	5.020	3	148496	-25	66	8
LQR + DM	4.859	-1	115027	-42	57	-7
LQR + DM + GLA	5.267	8	66930	-66	62	2
LQG	4.912	0	114700	-42	54	-11
LQG + DM	4.761	-3	98302	-51	50	-18
LQG + DM + GLA	4.913	0	60113	-70	56	-8

Figures E.16 - E.18 show the simulation responses to the von Kármán Severe turbulence for the LQG controller with aeroelastic mode suppression and the LQG controller with aeroelastic mode suppression and active gust load alleviation.

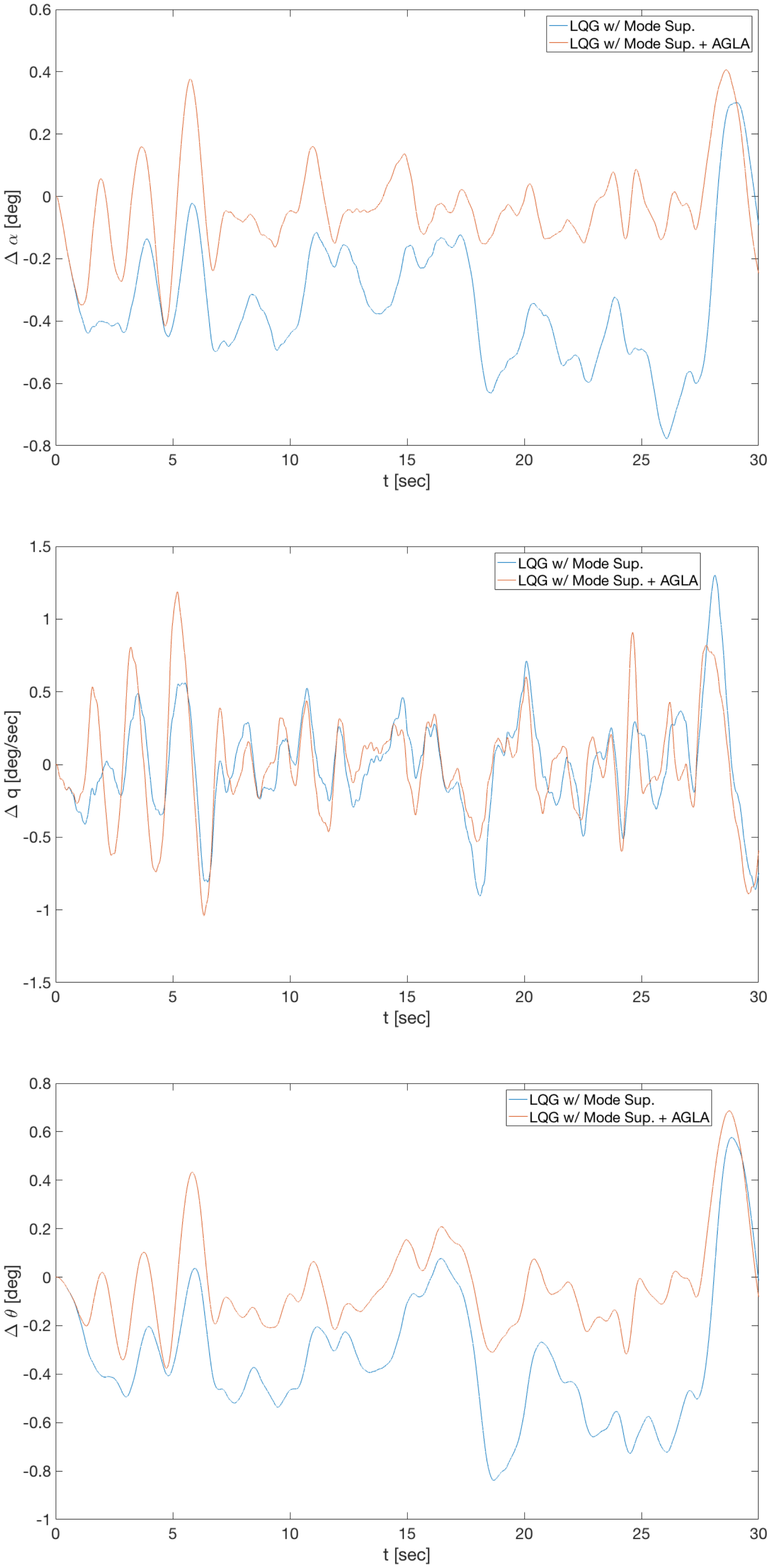

Figure E.16: Rigid-body response to severe von Kármán turbulence

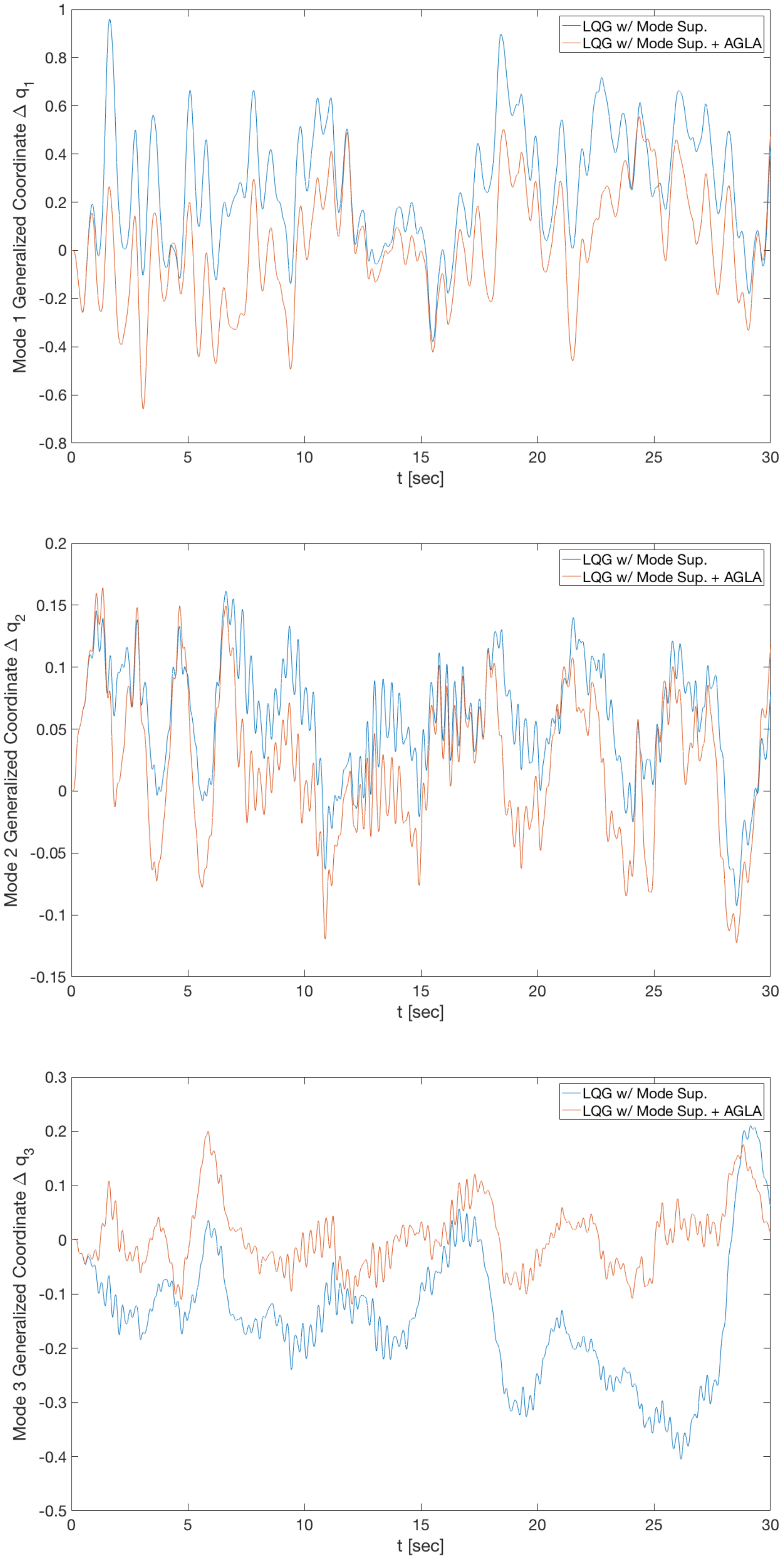

Figure E.17: Elastic response to severe von Kármán turbulence

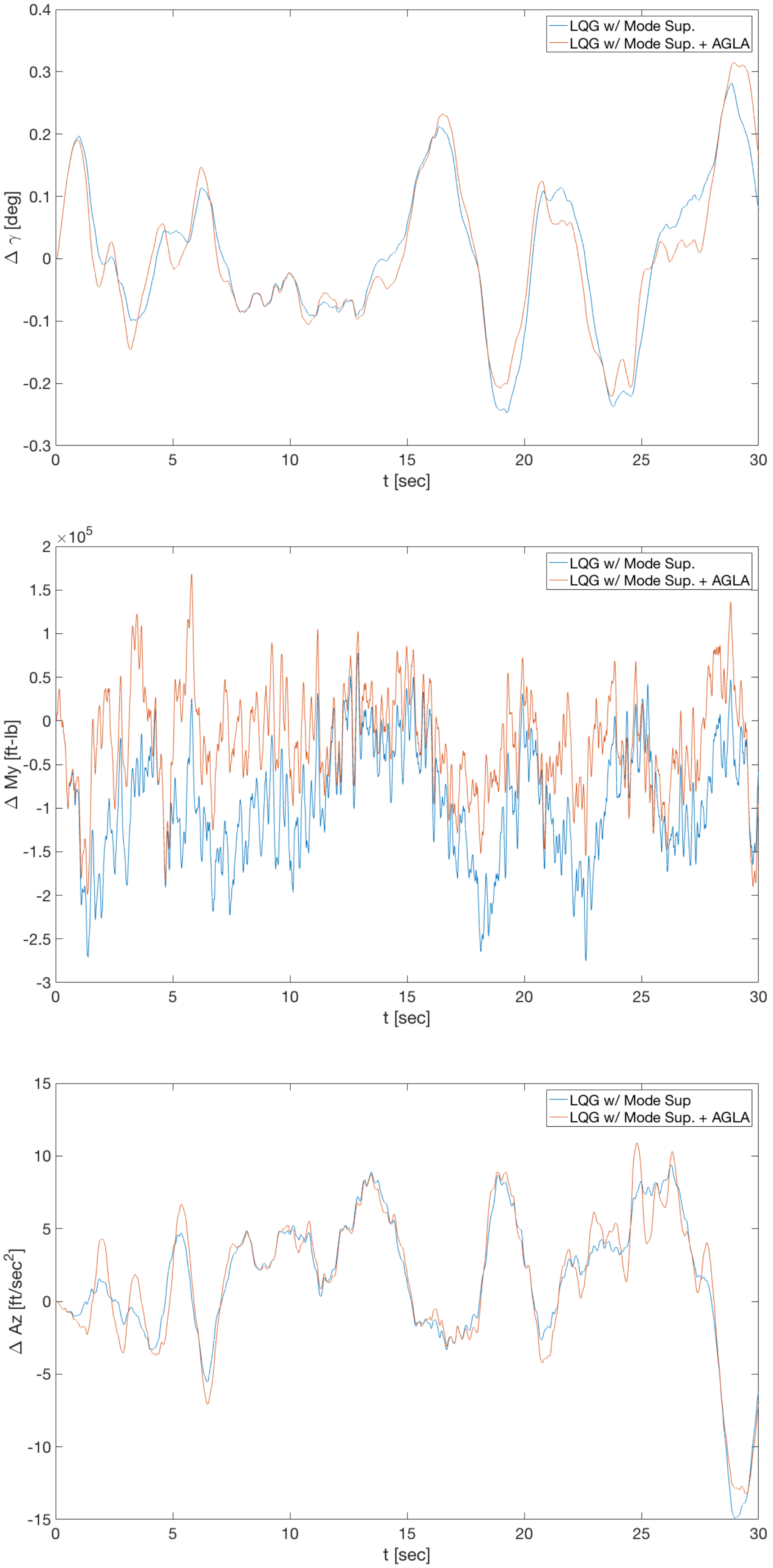

Figure E.18: Flight-path angle, structural and acceleration response to severe von Kármán turbulence

F

Active Gust Load Alleviation of High-Aspect Ratio Flexible Wing Aircraft

Active Gust Load Alleviation of High-Aspect Ratio Flexible Wing Aircraft

Y.L. Ferrier*

Delft University of Technology, Delft, The Netherlands

N.N. Nguyen[†] E. Ting[‡] D. Chaparro[§]

NASA Ames Research Center, Moffett Field, CA 94035

X. Wang [¶] C.C. de Visser[‖] Q.P. Chu [**]

Delft University of Technology, Delft, The Netherlands

This paper presents a novel active gust load alleviation approach within a multi-objective flight control framework developed by NASA for a flexible wing aircraft. The aircraft model is based on the NASA Generic Transport Model (GTM). The wing structures incorporate an aerodynamic control surface known as the Variable Camber Continuous Trailing Edge Flap (VCCTEF). Previous work already showed the ability of the VCCTEF to perform aeroelastic mode suppression, drag minimization and maneuver load alleviation in a multi-objective flight control framework. In this paper, the multi-objective flight control framework is extended to include active gust load alleviation. A Linear-Quadratic Gaussian (LQG) controller is augmented with Model Reference Adaptive Control (MRAC) to provide active gust load alleviation. Disturbance estimation is done using an Extended State Observer (ESO) to support the design of the active gust load alleviation controller. The results demonstrate the potential of active gust load alleviation within a multi-objective flight control framework for a high-aspect ratio flexible wing aircraft embodied with the VCCTEF.

---

[*] MSc. student, Control and Simulation Section, Faculty of Aerospace Engineering, Delft University of Technology; Kluyverweg 1, 2629HS, Delft, The Netherlands. y.l.ferrier@tudelft.nl.

[†] Senior Research Scientist, Associate Fellow AIAA, Intelligent Systems Division, nhan.t.nguyen@nasa.gov

[‡] Engineer, Intelligent Systems Division, eric.b.ting@nasa.gov

[§] Engineer, Intelligent Systems Division, daniel.chaparro@nasa.gov

[¶] PhD Candidate, Control and Simulation Section, Faculty of Aerospace Engineering, Delft University of Technology; Kluyverweg 1, 2629HS, Delft, The Netherlands. X.Wang-6@tudelft.nl.

[‖] Assistant Professor, Control and Simulation Section, Faculty of Aerospace Engineering, Delft University of Technology; Kluyverweg 1, 2629HS, Delft, The Netherlands, c.c.devisser@tudelft.nl, AIAA member.

[**] Associate Professor, Control and Simulation Section, Faculty of Aerospace Engineering, Delft University of Technology; Kluyverweg 1, 2629HS, Delft, The Netherlands, Q.P.Chu@tudelft.nl, AIAA member.

I. Introduction

Formerly, aircraft were designed to provide safe load-carrying capacity by maintaining sufficient structural rigidity. The introduction of composite materials in commercial aircraft has disrupted the aviation industry by providing the same-load carrying capacity at lower weight. The weight reduction that results from the use of these composite airframes can translate into a fuel consumption advantage. This advantage has triggered aircraft manufacturers to design the airframes of their new-generation aircraft mostly out of composite materials. An example of a light-weight airframe design is the Boeing 787 Dreamliner aircraft, which uses at least 50% of composite materials in the airframe construction.

The composite wing structures provide the same load-carrying capacity, however exhibit less structural rigidity. The disadvantage of the increased flexibility of the wings is that, especially in combination with a high-aspect ratio, large aeroelastic deflections can occur that may result in adverse aerodynamics. The benefit of the weight reduction by using these composite materials could be annihilated by the increase in drag, and thus fuel consumption, due to the adverse aerodynamics. Performance Adaptive Aeroelastic Wing (PAAW) technology was developed under NASA Advanced Air Transport Technology project to address these challenges for future flexible wing transports. PAAW technology strives to find a multi-disciplinary solution that maximizes the aerodynamic performance of the future wing designs while also addressing the operational constraints that can mitigate the aerodynamic performance and flight safety. For high-aspect ratio flexible wing aircraft, the most important operational constraints are the reduced flutter margins, increased airframe responses to gust and maneuver loads, and degraded pilot handling and ride qualities.

A multi-objective flight control framework has been developed to simultaneously address the aerodynamic performance objective and the operational constraints.[1–3] This framework takes advantage of a multi-functional aerodynamic control surface called the Variable Camber Continuous Trailing Edge Flap (VCCTEF).[4–6]

The VCCTEF is a candidate PAAW concept that was initially proposed by NASA[1,4] and subsequently jointly developed by NASA and Boeing Research & Technology under the NASA Fixed Wing project in 2010. The VCCTEF, illustrated on the GTM in Fig. 1, provides active wing shaping control to improve the aerodynamic efficiency throughout a flight envelope. Initial studies indicate the ability of the VCCTEF to reduce drag for significant fuel savings[7,8] and the ability to provide flutter mode suppression and maneuver load alleviation in combination with drag cognizant control.[2,9]

This paper describes the formulation of an aeroservoelastic model of the GTM with the VCCTEF and the application of a multi-objective flight control framework focusing on gust load alleviation for an altitude-hold flight control mode in symmetric flight conditions.

The GTM aircraft model used in this study represents a general short-to-medium range commercial

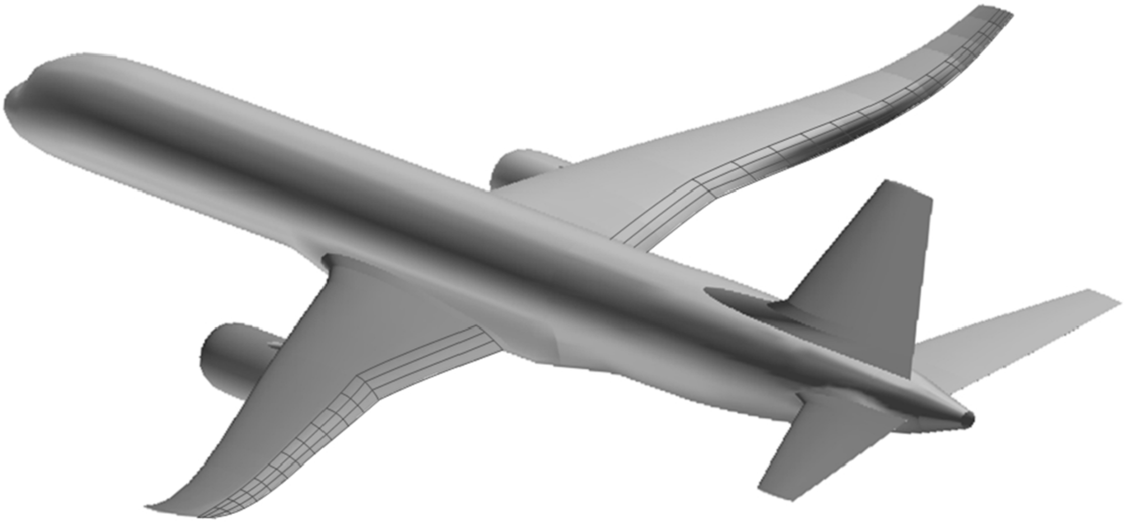

Figure 1. GTM with Variable Camber Continuous Trailing Edge Flap

passenger aircraft. The wing planform of the GTM incorporates the VCCTEF, illustrated in Fig. 2. The flap system consists of 16 individual spanwise sections which enable spanwise load tailoring. This lay-out provides the ability to control the wing twist shape in the spanwise direction. By changing the wing twist, and thus the spanwise loading, the aerodynamic performance can be improved for different flight conditions.

The spanwise flap sections are connected by an elastomer transition material, illustrated as black lines in between the spanwise flap sections as shown in Fig. 2. This transition material creates a continuous trailing edge flap when the flap sections are deflected. A continuous trailing edge flap has several advantages, such as improved aerodynamic efficiency and the mitigation of strong vortices by avoiding flap discontinuities.

The flap sections consist of three chordwise segments of equal chord length, illustrated in Fig. 3. These chordwise segments can be deflected individually to create camber surfaces for the desired aerodynamic performance. In this study the relative deflection of the chordwise segments is constrained to a circular-arc camber shape, which has a superior aerodynamic performance compared to other camber configurations,[10]

$$\begin{aligned} \delta_{i,1} &= \tfrac{1}{3}\delta_{i,3} \\ \delta_{i,2} &= \tfrac{2}{3}\delta_{i,3} \end{aligned} \tag{1}$$

This relation allows the control method to only regard the deflection of the outermost chordwise segment, $\delta_{i,3}$. The deflection angle of each chordwise segment is measured relative to the hinge and the undeflected trailing edge as shown in Fig. 3.

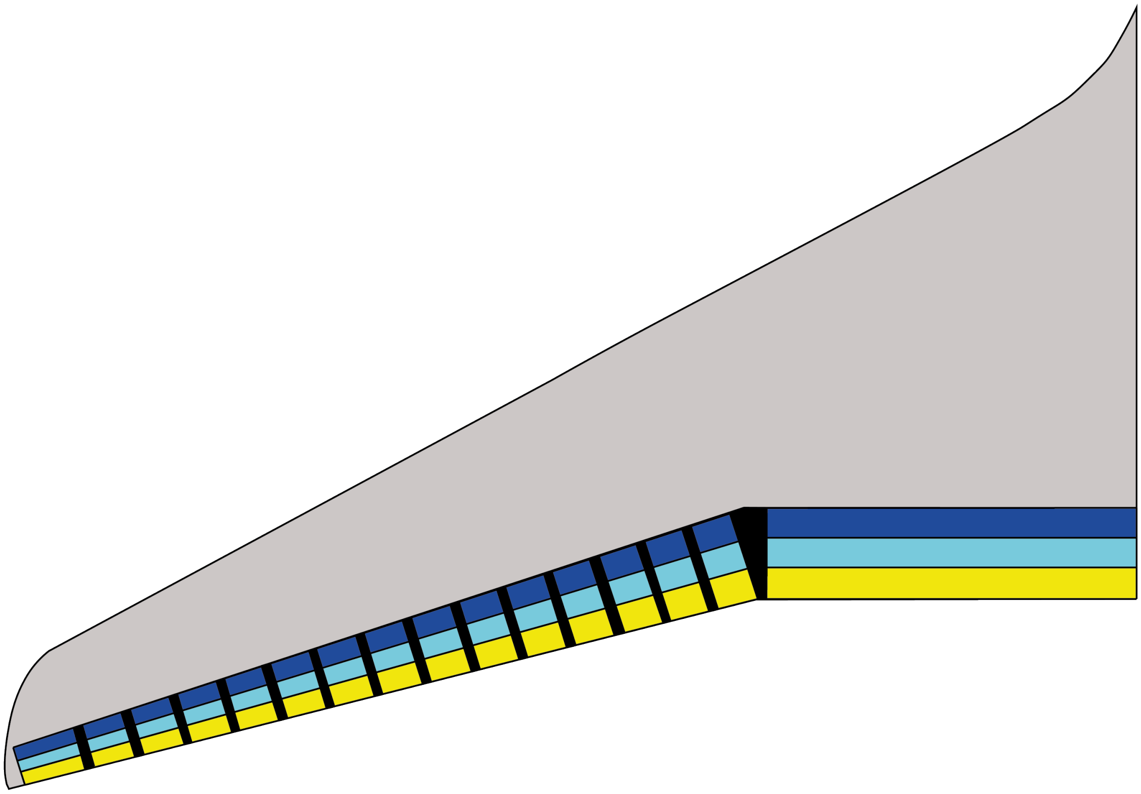

Figure 2. GTM Wing configured with VCCTEF

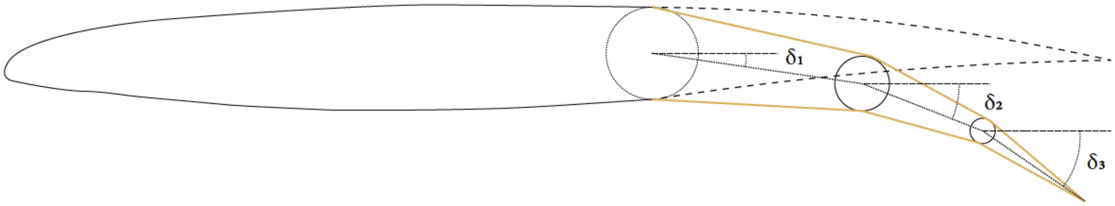

Figure 3. Three-Segment Variable Camber Continuous Trailing Edge Flap

II. Aeroservoelastic Model Formulation

For controller design and simulation purposes, an aeroservoelastic (ASE) model of a flexible wing aircraft equipped with the VCCTEF is developed by the Advanced Control and Evolvable Systems Group at NASA Ames Research Center. The ASE model includes the rigid aircraft flight dynamics, wing dynamic aeroelasticity, flight control actuator dynamics of the flap system, and servo-motor dynamics.[3, 11, 12]

In general, the rigid aircraft flight dynamic equation is expressed as[3]

$$\begin{aligned} M_r \dot{x}_r = {} & Q_r \dot{x}_r + P_r x_r + D_r \delta_r + V_{rn} \ddot{q} + \left(T_{rn} + 0.5 T_{rc}\right) \dot{q} + \left[S_{rn} + 0.5 S_{rc} + a_4 \left(\frac{2V_\infty}{c}\right) T_{rc}\right] q + S_{rc} y + \left(\frac{2V_\infty}{c}\right) T_{rc} z \\ & + F_{rn} \ddot{\delta}_e + \left(E_{rn} + 0.5 E_{rc}\right) \dot{\delta} + \left[D_{rn} + 0.5 D_{rc} + a_4 \left(\frac{2V_\infty}{c}\right) E_{rc}\right] \delta + D_{rc} \nu + \left(\frac{2V_\infty}{c}\right) E_{rc} w \end{aligned} \tag{2}$$

where x_r is the rigid aircraft state vector, q is the generalized displacement vector of the wing, y and z are the aerodynamic lag state vectors for the wing structural dynamics, δ_r is the rigid aircraft flight control surface deflection vector, δ is the VCCTEF deflection vector, ν and w are the aerodynamic lag state vectors for the VCCTEF actuator dynamics, the upper case variables are matrices, the subscript r denotes a rigid quantity, and the subscripts n and c signify non-circulatory and circulatory quantities according to the Theodorsen's theory.[9]

For symmetric flight conditions, the rigid aircraft state vector x_r includes the altitude h, airspeed V, angle of attack α, pitch rate q (not to be confused with the generalized displacement vector), and pitch angle θ. The rigid aircraft flight control surface deflection vector δ_r includes the thrust δ_T and elevator deflection δ_e.

The aerodynamic lag states account for the unsteady aerodynamic effect which is represented by the reduced frequency-dependent Theodorsen's function. The R.T. Jones approximation is used to convert the Theordorsen's function into a time-domain representation by the aerodynamic lag states.[12, 13]

Using the finite-element formulation, the aeroelastic equation of the wing structure is discretized in generalized coordinates q (not to be confused with the pitch rate) as

$$\begin{aligned} \left(M_s + M_{an}\right) \ddot{q} + \left(C_s + C_{an} + 0.5 C_{ac}\right) \dot{q} + \left[K_s + 0.5 K_{ac} + a_4 \left(\frac{2V_\infty}{c}\right) C_{ac}\right] q + K_{ac} y + \left(\frac{2V_\infty}{c}\right) C_{ac} z = {} & Q_e \dot{x}_r + P_e x_r \\ + F_{en} \ddot{\delta} + \left(E_{en} + 0.5 E_{ec}\right) \dot{\delta} + \left[D_{en} + 0.5 D_{ec} + a_4 \left(\frac{2V_\infty}{c}\right) E_{ec}\right] \delta + D_{ec} \nu + \left(\frac{2V_\infty}{c}\right) E_{ec} w & \end{aligned} \tag{3}$$

where the subscript s denotes a structural dynamic quantity, the subscript a denotes an aerodynamic quantity due to the unsteady aerodynamic effect, and the subscript e denotes an aeroelastic quantity associated with the wing aeroelasticity.

The aerodynamic lag state equations for the wing structural dynamics obtained from the R.T. Jones approximation are

$$\ddot{y} + a_3 \left(\frac{2V_\infty}{c} \right) \dot{y} + a_2 \left(\frac{2V_\infty}{c} \right)^2 y = a_4 \left(\frac{2V_\infty}{c} \right) \dot{q} + 0.5 a_2 \left(\frac{2V_\infty}{c} \right)^2 q \tag{4}$$

$$\ddot{z} + a_3 \left(\frac{2V_\infty}{c} \right) \dot{z} + a_2 \left(\frac{2V_\infty}{c} \right)^2 z = a_5 \left(\frac{2V_\infty}{c} \right) \dot{q} + a_6 \left(\frac{2V_\infty}{c} \right)^2 q \tag{5}$$

The actuator dynamic equation of the VCCTEF is expressed as

$$\begin{gathered} M_\delta \ddot{\delta} + C_\delta \dot{\delta} + K_\delta \delta = Q_\delta \dot{x}_r + P_\delta x_r + V_{\delta n} \ddot{q} + \left(T_{\delta n} + 0.5 T_{\delta c} \right) \dot{q} + \left[S_{\delta n} + 0.5 S_{\delta c} + a_4 \left(\frac{2V_\infty}{c} \right) T_{\delta c} \right] q \\ + S_{\delta c} y + \left(\frac{2V_\infty}{c} \right) T_{\delta c} z + F_{\delta n} \ddot{\delta} + \left(E_{\delta n} + 0.5 E_{\delta c} \right) \dot{\delta} + \left[D_{\delta n} + 0.5 D_{\delta c} + a_4 \left(\frac{2V_\infty}{c} \right) E_{\delta c} \right] \delta + D_{\delta c} \nu + \left(\frac{2V_\infty}{c} \right) E_{\delta c} w + \tau_\delta \end{gathered} \tag{6}$$

where τ_δ is the motor torque.

The aerodynamic lag state equations for the actuator dynamics are

$$\ddot{\nu} + a_3 \left(\frac{2V_\infty}{c} \right) \dot{\nu} + a_2 \left(\frac{2V_\infty}{c} \right)^2 \nu = a_4 \left(\frac{2V_\infty}{c} \right) \dot{\delta} + 0.5 a_2 \left(\frac{2V_\infty}{c} \right)^2 \delta \tag{7}$$

$$\ddot{w} + a_3 \left(\frac{2V_\infty}{c} \right) \dot{w} + a_2 \left(\frac{2V_\infty}{c} \right)^2 w = a_5 \left(\frac{2V_\infty}{c} \right) \dot{\delta} + 0.5 a_6 \left(\frac{2V_\infty}{c} \right)^2 \delta \tag{8}$$

The actuator dynamics of the rigid aircraft flight control are assumed to be a first-order model

$$\dot{\delta}_r = -\lambda \left(\delta_r - \delta_{rc} \right) \tag{9}$$

where $\lambda > 0$ is the actuator rate vector and δ_{rc} is the command vector of the rigid-body aircraft control.

The servo-motor dynamics for the VCCTEF are formed by a PID feedback control law

$$\dot{e} = \delta - \delta_c \tag{10}$$

$$\tau_\delta = k_p \left(\delta - \delta_c \right) + k_i e + k_d \dot{\delta} \tag{11}$$

where e is the integral error of the VCCTEF deflection command δ_c.

The fully coupled ASE flight dynamic model is given by Nguyen et al. (2017).[3] This ASE state-space model can be expressed as

$$\begin{bmatrix} M_{rr} & M_{re} & M_{r\delta} & M_{rs} \\ M_{er} & M_{ee} & M_{e\delta} & M_{es} \\ M_{\delta r} & M_{\delta e} & M_{\delta\delta} & M_{\delta s} \\ M_{sr} & M_{se} & M_{s\delta} & M_{ss} \end{bmatrix} \begin{bmatrix} \dot{x}_r \\ \dot{x}_e \\ \dot{x}_\delta \\ \dot{x}_s \end{bmatrix} = \begin{bmatrix} S_{rr} & S_{re} & S_{r\delta} & S_{rs} \\ S_{er} & S_{ee} & S_{e\delta} & S_{es} \\ S_{\delta r} & S_{\delta e} & S_{\delta\delta} & S_{\delta s} \\ S_{sr} & S_{se} & S_{s\delta} & S_{ss} \end{bmatrix} \begin{bmatrix} x_r \\ x_e \\ x_\delta \\ x_s \end{bmatrix} + \begin{bmatrix} T_r \\ T_e \\ T_\delta \\ T_s \end{bmatrix} u \tag{12}$$

where $x_r = \begin{bmatrix} h & u & \alpha & q & \theta \end{bmatrix}^T$, $x_e = \begin{bmatrix} q & y & z & \dot{q} & \dot{y} & \dot{z} \end{bmatrix}^T$, $x_\delta = \begin{bmatrix} \delta & \nu & w & \dot{\delta} & \dot{\nu} & \dot{w} \end{bmatrix}^T$, $x_s = \begin{bmatrix} \delta_r^T & e^T \end{bmatrix}^T$, and $u = \begin{bmatrix} \delta_{rc}^T & \delta_c^T \end{bmatrix}^T$. This dynamic model under gust excitation can be rewritten as

$$\dot{x} = Ax + Bu + w_g \tag{13}$$

where $x = \begin{bmatrix} x_r^T & x_e^T & x_\delta^T & x_s^T \end{bmatrix}^T$, w_g is the gust disturbance and

$$A = \begin{bmatrix} M_{rr} & M_{re} & M_{r\delta} & M_{rs} \\ M_{er} & M_{ee} & M_{e\delta} & M_{es} \\ M_{\delta r} & M_{\delta e} & M_{\delta\delta} & M_{\delta s} \\ M_{sr} & M_{se} & M_{s\delta} & M_{ss} \end{bmatrix}^{-1} \begin{bmatrix} S_{rr} & S_{re} & S_{r\delta} & S_{rs} \\ S_{er} & S_{ee} & S_{e\delta} & S_{es} \\ S_{\delta r} & S_{\delta e} & S_{\delta\delta} & S_{\delta s} \\ S_{sr} & S_{se} & S_{s\delta} & S_{ss} \end{bmatrix} \tag{14}$$

$$B = \begin{bmatrix} M_{rr} & M_{re} & M_{r\delta} & M_{rs} \\ M_{er} & M_{ee} & M_{e\delta} & M_{es} \\ M_{\delta r} & M_{\delta e} & M_{\delta\delta} & M_{\delta s} \\ M_{sr} & M_{se} & M_{s\delta} & M_{ss} \end{bmatrix}^{-1} \begin{bmatrix} T_r \\ T_e \\ T_\delta \\ T_s \end{bmatrix} \tag{15}$$

Four accelerometers are placed on the wing to observe the elastic states. Their output equations are computed as

$$\ddot{v} = \Phi \ddot{q} = \Phi E \dot{x}_e \tag{16}$$

where Φ is the matrix of eigenvectors and $E = \begin{bmatrix} 0 & 0 & 0 & I & 0 & 0 \end{bmatrix}$ such that $\ddot{q} = E\dot{x}_e$.

Then,

$$\ddot{v} = \Phi E G \left(Ax + Bu + w_g \right) \tag{17}$$

where $G = \begin{bmatrix} 0 & I & 0 & 0 \end{bmatrix}$ such that $\dot{x}_e = G\dot{x}$.

For a given acceleration location, then

$$\ddot{v}_c = F\ddot{v} = F\Phi EG\left(Ax + Bu + w_g\right) \tag{18}$$

where F is determined from the location of the acceleration measurement.

Let $y = \ddot{v}_c$ be the output, then

$$y = Cx + Du + Hw_g \tag{19}$$

where

$$C = F\Phi EGA \tag{20}$$

$$D = F\Phi EGB \tag{21}$$

$$H = F\mathit{\Phi} EG \tag{22}$$

In this study, the aircraft drag, wing root bending moment and vertical acceleration at the center of gravity are used in the multi-objective control formulation and to assess the controller performance. The aircraft drag is expressed as

$$C_D = C_{D_0} + \left(C_{L_0} + C_{L_{\dot{x}}}\dot{x} + C_{L_x}x + C_{L_u}u\right)^T K\left(C_{L_0} + C_{L_{\dot{x}}}\dot{x} + C_{L_x}x + C_{L_u}u\right) \tag{23}$$

The incremental drag is included in the optimal control cost function as a penalty for the drag minimization objective. From Eq.(23), the incremental drag is computed as

$$\Delta C_D = C_{D_x}x + C_{D_u}u + x^T C_{D_{x^2}}x + x^T C_{D_{xu}}u + u^T C_{D_{u^2}}u \tag{24}$$

The wing bending moment is expressed in general as

$$M_y = M_x x + M_u u + M_w w_g \tag{25}$$

where $M_w w_g$ is a bending moment component due to the gust disturbance.

The vertical acceleration at the aircraft center of gravity A_z is defined as

$$A_z = \frac{-Z}{m} \tag{26}$$

where Z is the downward vertical force and m is the aircraft mass. This definition can be expressed as

$$A_z = -V\dot{\alpha} - \dot{V}\alpha + qV + g\cos\theta \tag{27}$$

where V is the aircraft velocity, α is the angle of attack, q is the pitch rate, g is the local gravitational field of the Earth, and θ is the pitch angle. Because the term corresponding to the gravitational field is approximately constant ($g\cos\theta \approx g$), the incremental vertical acceleration of the aircraft center of gravity ΔA_z is used as a performance metric to evaluate the active gust load alleviation controller

$$\Delta A_z = -V\dot{\alpha} - \dot{V}\alpha + qV \tag{28}$$

The full-order coupled flight dynamic and ASE model includes a high number of elastic modes along with corresponding aerodynamic lag states. In this study, the full model has 198 elastic modes. Together with the rigid-body states, dynamic and aerodynamic lag states for the 16 VCCTEF elements and servo states this results in an ASE state-space model of 1307 states.

A reduced-order model is built for the convenience of a controller design. In general, an ASE state-space model contains rigid-body modes which usually have low frequencies and aeroelastic modes which are at higher frequencies than the rigid-body modes. In control design, it is sufficient to only consider the aeroelastic modes that are at the lower frequency range. This is because the high-frequency modes attenuate fast, and therefore have small response amplitudes. A reduced-order model is developed for control design purposes by only considering the low-frequency aeroelastic modes. The number of low-frequency aeroelastic modes is selected to ensure the flutter modes are captured. For this reduced-order model, the first lowest 10 frequency modes are retained.

III. Active Gust Load Alleviation in Multi-Objective Flight Control

A multi-objective flight control framework is designed to simultaneously address the operational constraints and the aerodynamic performance during the entire flight envelope. This is in contrast with conventional flight controllers of which the performance is only based on the pilot command-following ability. The introduction of the aerodynamic performance into the flight control framework allows the new controller to minimize the drag through adaptive aeroelastic wing shaping. This is done by adding a drag penalty into the control framework. The multi-objective flight control framework has both a pilot command-following objective and a drag reduction objective.[1–4]

Next to these two objectives, the stability of the aircraft is of utmost importance. The structural flexibility of the flexible wing aircraft can lead to degraded stability margins due to large aeroelastic deflections and interactions. The multi-objective flight control framework needs to contain an aeroelastic mode suppression objective to suppress the flutter or aeroelastic modes in order to meet the pilot handling quality requirements.

Furthermore, the increased airframe responses of flexible aircraft due to the gust and maneuver loads needs to be addressed. For flexible wing aircraft, gust disturbances and maneuvers can cause aeroelastic responses that may reduce the pilot handling and ride qualities. Gust load alleviation (GLA) can be provided by using either reactive feedback control or predictive feedforward control. The development of new sensor technologies such as light detection and ranging allows for predictive feedforward control methods. Currently, the advancement of these sensor technologies is still pending. Therefore this study uses reactive feedback control to design an active gust load alleviation approach. Likewise, the unwanted effects of maneuver loads can be suppressed by maneuver load alleviation.

In summary, the multi-objective flight control framework needs to harmoniously integrate the following objectives: 1) traditional pilot command-following control, 2) drag minimization, 3) aeroelastic mode suppression, and 4) gust and maneuver load alleviation. The integration of these objectives results in a complex control design that needs to take into account and compromise between competing objectives. The architecture of this control framework is illustrated in Fig. 4.[2] Next to these objectives a real-time drag minimization approach can be included in the control design.[8]

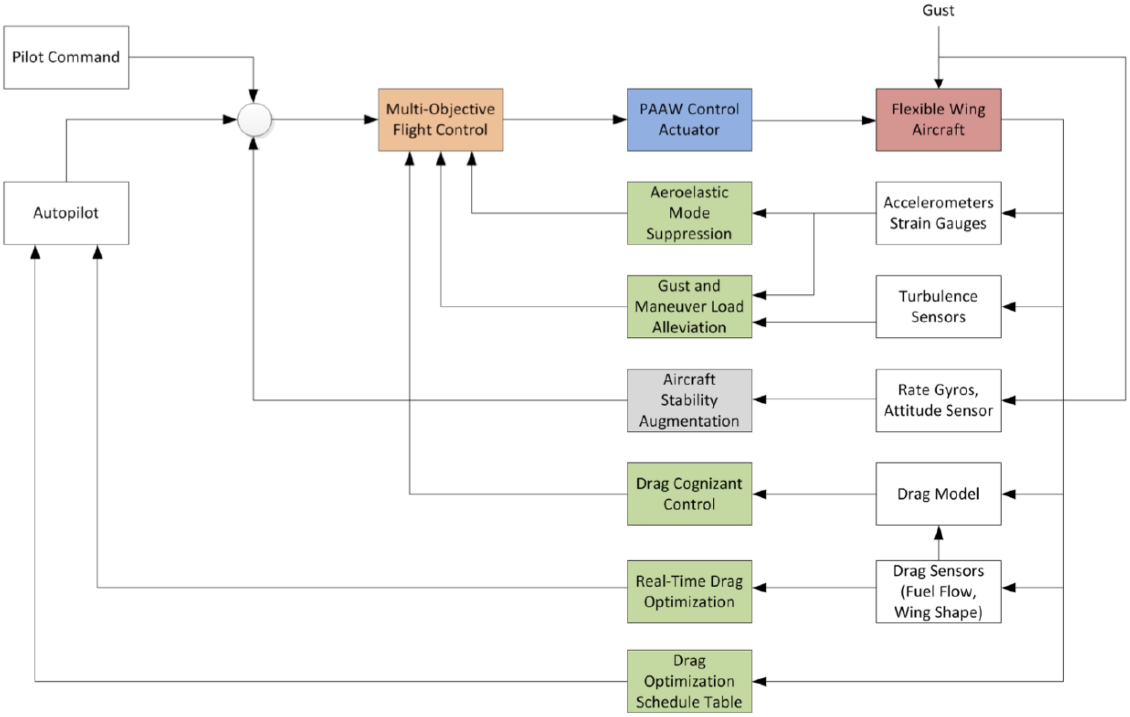

Figure 4. Multi-Objective Flight Control Architecture[2]

A. Controller Design

The flight controller is designed to provide an altitude-hold mode by following a flight path angle command. We define an integral error state of the flight path angle $x_a = \int_0^t \Delta\gamma d\tau$, where the error between the flight path angle and the command signal is expressed as

$$\Delta\gamma = \theta - \alpha - \gamma_c = A_a x_r - \gamma_c \tag{29}$$

where γ_c is the commanded flight path angle.

Now, let $x = \begin{bmatrix} x_r^T & x_e^T & x_\delta^T & x_s^T & x_a^T \end{bmatrix}^T$ and $u = \begin{bmatrix} \delta_{rc}^T & \delta_c^T \end{bmatrix}^T$, then the state-space system for the controller design is expressed as

$$\dot{x} = Ax + Bu + z + w_g \tag{30}$$

where

$$A = \begin{bmatrix} A_{rr} & A_{re} & A_{r\delta} & A_{rs} & 0 \\ A_{er} & A_{ee} & A_{e\delta} & A_{es} & 0 \\ A_{\delta r} & A_{\delta e} & A_{\delta\delta} & A_{\delta s} & 0 \\ A_{sr} & A_{se} & A_{s\delta} & A_{ss} & 0 \\ A_a & 0 & 0 & 0 & 0 \end{bmatrix}, B = \begin{bmatrix} B_{rr} & B_{re} \\ B_{er} & B_{ee} \\ B_{\delta r} & B_{\delta e} \\ B_{sr} & B_{se} \\ 0 & 0 \end{bmatrix} z = \begin{bmatrix} 0 \\ 0 \\ 0 \\ 0 \\ -\gamma_c \end{bmatrix} \tag{31}$$

The ASE state-space model of Eq.(30) can be written as

$$\dot{x}_r = A_{rr}x_r + A_{re}x_e + B_{rr}u_r + B_{re}u_e + z_r + w_r \tag{32}$$

$$\dot{x}_e = A_{er}x_r + A_{ee}x_e + B_{er}u_r + B_{ee}u_e + z_e + w_e \tag{33}$$

where x_r is the rigid-body state vector that includes the actuator state vector of the VCCTEF and the servo-motor state vector, x_e is the elastic state vector, u_r is the rigid aircraft control input vector, u_e is the VCCTEF control input vector, z_r is the command vector to the rigid aircraft state, z_e is the command vector to the elastic state, w_r is the disturbance to the rigid aircraft state, and w_e is the disturbance to the elastic state.

We formulate a multi-objective infinite time-horizon cost function as follows:

$$J = J_r + J_e \tag{34}$$

where

$$J_r = \lim_{t_f \to \infty} \frac{1}{2} \int_0^{t_f} \left[x_r^T Q_r x_r + u_r^T R_r u_r \right] dt \tag{35}$$

$$J_e = \lim_{t_f \to \infty} \frac{1}{2} \int_0^{t_f} \left[x_e^T Q_e x_e + u_e^T R_e u_e + q_D \Delta C_D \right] dt \tag{36}$$

The rigid aircraft controller u_r can be designed based on the cost function J_r to enable a rigid aircraft state $x_a = F x_r$ to track a command signal z. The VCCTEF controller u_e is designed based on the total cost function J to provide drag minimization and aeroelastic mode suppression.

B. Rigid Aircraft Control

A nominal rigid aircraft controller is designed to validate the performance of the multi-objective flight controller with active gust load alleviation. The design of the nominal rigid aircraft controller (NRC) is done by formulating the Hamiltonian function for the nominal rigid aircraft dynamics

$$H = \frac{1}{2} \left(x_r^T Q_r x_r + u_r R_r u_r \right) + \lambda^T \left(A_{rr} x_r + B_r u_r + z_r \right) \tag{37}$$

where λ is the adjoint variable.

The adjoint equation and optimal control are obtained as

$$\dot{\lambda} = -\frac{\partial H^T}{\partial x_r} = -Q_r x_r - A_{rr}^T \lambda \tag{38}$$

$$\frac{\partial H^T}{\partial u_r} = R_r u_r + B_r^T \lambda = 0 \Rightarrow u_r = -R_r B_r^T \lambda \tag{39}$$

subject to the transversality condition $\lambda(t_f) = 0$.

Let $\lambda = P x_r + S z_r$. Then,

$$\dot{P} x_r + P \dot{x}_r + \dot{S} z_r + S \dot{z}_r = -Q_r x_r - A_{rr}^T \left(P x_r + S z_r \right) \tag{40}$$

For the infinite time-horizon optimal control, $\dot{P} = 0$ and $\dot{S} = 0$. Therefore, we obtain the algebraic Ricatti equation

$$P A_{rr} + A_{rr}^T P - P B_r R_r^{-1} B_r^T P + Q_r = 0 \tag{41}$$

and

$$S = -\left(A_{rr}^T - P B_r R_r^{-1} B_r^T\right)^{-1} P \tag{42}$$

Then, the nominal rigid aircraft controller is given by

$$u_r = K_{x_r} x_r + K_z z_r \tag{43}$$

where

$$K_{x_r} = -R_r B_r^T P \tag{44}$$

$$K_{z_r} = -R_r B_r^T S \tag{45}$$

C. Multi-Objective Flight Control

The multi-objective flight controller is designed to include aeroelastic mode suppression and drag minimization.

We formulate the Hamiltonian of the total cost function J using the reduced-order model as

$$H = \frac{1}{2}\left(x^T Q x + u^T R u + q_D \Delta C_D\right) + \lambda^T \left(Ax + Bu + z\right) \tag{46}$$

Inserting Eq.(24) in the Hamiltonian gives

$$H = \frac{1}{2} x^T Q x + \frac{1}{2} u^T R u + \frac{1}{2} q_D \left(C_{D_x} x + C_{D_u} u + x^T C_{D_{x^2}} x + x^T C_{D_{xu}} u + u^T C_{D_{u^2}} u\right) + \lambda^T \left(Ax + Bu + z\right) \tag{47}$$

The adjoint equation and optimal control are obtained as

$$\dot{\lambda} = -\frac{\partial H^T}{\partial x} = -Qx - \frac{1}{2} q_D \left(C_{D_x}^T + 2 C_{D_{x^2}}^T x + C_{D_{xu}}^T u\right) - A^T \lambda \tag{48}$$

$$\frac{\partial H^T}{\partial u} = Ru + \frac{1}{2} q_D \left(C_{D_u}^T + C_{D_{xu}}^T x + 2 C_{D_{u^2}}^T u\right) + B^T \lambda = 0 \Rightarrow$$

$$u = -\left(R + q_D C_{D_{u^2}}^T\right)^{-1} \left(B^T \lambda + \frac{1}{2} q_D C_{D_u}^T + \frac{1}{2} q_D C_{D_{xu}}^T x\right) \tag{49}$$

We assume $\lambda = Wx + Vz + \lambda_0$. Then

$$\dot{W}x + W\dot{x} + \dot{V}z + V\dot{z} = -Qx - \frac{1}{2}q_D\left(C_{D_x}^T + 2C_{D_{x^2}}^T x + C_{D_{xu}}^T u\right) - A^T\left(Wx + Vz + \lambda_0\right) \tag{50}$$

Let γ_c be constant so that $\dot{\gamma}_c = 0$. Let $t_f \to \infty$, then the optimal solution approaches a steady-state solution. Therefore, $\dot{W}(t_f) = 0$ and $\dot{V}(t_f) = 0$. Then, separating terms yields the following expressions

$$W\bar{A} + \bar{A}^T W - WB\bar{R}^{-1}B^T W + \bar{Q} = 0 \tag{51}$$

$$V = -\left(\bar{A}^T - WB\bar{R}^{-1}B^T\right)^{-1} W \tag{52}$$

$$\lambda_0 = -\left(\bar{A}^T - WB\bar{R}^{-1}B^T\right)^{-1}\left(\frac{1}{2}q_D C_{D_x}\right) \tag{53}$$

where

$$\bar{R} = R + q_D C_{D_{u^2}}^T \tag{54}$$

$$\bar{A} = A - \frac{1}{2}q_D B\bar{R}^{-1}C_{D_{xu}}^T \tag{55}$$

$$\bar{Q} = Q + q_D C_{D_{x^2}}^T - \left(\frac{1}{2}q_D C_{D_{xu}}^T\right)^T \bar{R}^{-1}\left(\frac{1}{2}q_D C_{D_{xu}}^T\right) \tag{56}$$

Since $Q > 0$, $q_D > 0$, $C_{D_{x^2}} > 0$, and $C_{D_{xu}} > 0$ it follows that $\bar{Q} > 0$.

The multi-objective flight controller is expressed as

$$u = K_x x + K_z z + \Lambda_0 \tag{57}$$

where

$$K_x = -\bar{R}^{-1}\left(B^T W + \frac{1}{2}q_D C_{D_{xu}}^T\right) \tag{58}$$

$$K_z = -\bar{R}^{-1}B^T V \tag{59}$$

$$\Lambda_0 = -\bar{R}^{-1}\left(B^T\lambda_0 + \frac{1}{2}q_D C_{D_u}^T\right) \tag{60}$$

D. Disturbance Estimation using Extended State Observer

Active Gust Load Alleviation is a form of active disturbance rejection control, a control type that directly suppresses internal or external disturbances. This method requires measurement or estimation of the disturbances. Today, new sensor technologies, such as Light Detection and Ranging (LIDAR), are advancing rapidly and could be used for the prediction or measurement of turbulence. However, at the moment, the performance of these technologies are not yet reliable and sufficiently accurate. Therefore, this study proposes a disturbance estimation technique. The disturbance estimation is done using an Extended State Observer (ESO), introduced by Han in 1995.[14] The ESO is the extended version of a Luenberger observer. This observer is selected because of its low dependence on model accuracy and good robustness properties. The ESO estimates disturbances by extending the system of the observer states with disturbance states.

Consider a nonlinear system of order n:

$$\begin{aligned}
\dot{x}_1 &= f_1(x_1) + g_1(x_1)\,x_2\\
\dot{x}_2 &= f_2(x_1,x_2) + g_2(x_{1,}x_2)\,x_3\\
&\vdots\\
\dot{x}_n &= f_n(x_1,x_2,\ldots,x_n) + g_n(x_1,x_2,\ldots,x_n)\,u
\end{aligned} \tag{61}$$

An extended state observer of order $2n$, where the states from $\dot{x}_{n+1}$ forward are the extended states, for the system of Eq.(61) can be expressed as

$$\begin{aligned}
\dot{\hat{x}}_1 &= f_1(\hat{x}_1) + g_1(\hat{x}_1)\,\hat{x}_2 + \hat{x}_{n+1} - \beta_1^T e_1\\
\dot{\hat{x}}_2 &= f_2(\hat{x}_1,\hat{x}_2) + g_2(\hat{x}_1,\hat{x}_2)\,\hat{x}_3 + \hat{x}_{n+2} - \beta_2^T e_2\\
&\vdots\\
\dot{\hat{x}}_n &= f_n(\hat{x}_1,\hat{x}_2,\ldots,\hat{x}_n) + g_n(\hat{x}_1,\hat{x}_2\hat{x}_2,\ldots,\hat{x}_n)\,u + \hat{x}_{2n} - \beta_n^T e_n\\
\dot{\hat{x}}_{n+1} &= -\beta_{n+1}^T e_1\\
\dot{\hat{x}}_{n+2} &= -\beta_{n+2}^T e_2\\
&\vdots\\
\dot{\hat{x}}_{2n} &= -\beta_{2n}^T e_n
\end{aligned} \tag{62}$$

where e_i is the error between the estimated states and the system states

$$e_i = \hat{x}_i - x_i \tag{63}$$

and where β_i are the observer gains. The observer gains β_i can be chosen by pole placement of the error dynamics to provide stability.[15]

For this study, Eq.(62) can be rewritten as

$$\begin{gathered}\dot{\hat{x}}_{1\ldots n} = A\hat{x}_{1\ldots n} + Bu + z_{1\ldots n} + \hat{w}_{g_{1\ldots n}} - \beta^T_{1\ldots n} e_{1\ldots n} \\ \dot{\hat{w}}_{g_{1\ldots n}} = -\beta^T_{n+1\ldots 2n} e_{1\ldots n} \\ e_{1\ldots n} = \hat{x}_{i\ldots n} - x_{i\ldots n}\end{gathered} \tag{64}$$

where $\hat{x}_{1\ldots n}$ are the observed states, $\hat{w}_g$ are the extended states and represent the estimates of the gust contribution w_g to the system states $x_{1\ldots n}$.

E. Active Gust Load Alleviation

Active Gust Load Alleviation uses Model Reference Adaptive Control (MRAC) to actively suppress the effect of turbulence. The multi-objective flight controller of Eq.(57) is the optimal baseline controller which is augmented with MRAC to actively cancel out the disturbance w_g.

The total control is expressed as

$$u\left(x, r, t\right) = u^*\left(x, r\right) + u_{ad}\left(t\right) \tag{65}$$

where u^* is the optimal baseline controller

$$u^* = K_x \hat{x} + K_z z + \mathit{\Lambda}_0 \tag{66}$$

and u_{ad} is the time-varying adaptive element.

The closed-loop dynamics of the reduced-order model are then obtained as

$$\dot{x} = \left(A + BK_x\right) x + BK_z z + \Lambda_0 + Bu_{ad} + z + w_g \tag{67}$$

The adaptive element u_{ad} is formulated according to MRAC principles to make the system states x track the states of a reference model x_{ref}. We define the reference model as

$$x_{ref} = A_{ref} x_{ref} + B_{ref} z + \Lambda_0 + z \tag{68}$$

where $A_{ref} = A + BKx$ is Hurwitz and $B_{ref} = BK_z$. The reference model represents the ideal closed-loop behavior in the absence of turbulence.

The tracking error equation is obtained as

$$\dot{e} = \dot{x}_{ref} - \dot{x} = A_{ref}e - Bu_{ad} - w_g \tag{69}$$

If u_{ad} perfectly cancels out w_g, then the tracking error will tend to zero asymptotically, i.e., $e \rightarrow 0$ as $t_f \rightarrow \infty$. In practice, there will always be a small residual error. The adaptive signal is defined as

$$u_{ad} = \hat{K}_w \hat{w}_g \tag{70}$$

where $\hat{K}_w$ is the adaptive disturbance gain and $\hat{w}_g$ is the disturbance estimation. The definition of the adaptive signal as in Eq.(70) is inspired by optimal control theory. The adaptive disturbance gain $\hat{K}_w$ can be seen as an estimate of the optimal disturbance gain K_w. This optimal disturbance gain can be derived in theory using optimal control theory and the differential Lyapunov equation. See Appendix A for the derivation of the optimal disturbance gain.

This paper introduces the estimation of the optimal disturbance gain $\hat{K}_w$ as an alternative approach in order to avoid the use of the differential Lyapunov equation.

Inserting the definition of the adaptive signal of Eq.(70) into the tracking error equation of Eq.(69) gives

$$\dot{e} = \dot{x}_{ref} - \dot{x} = A_{ref}e - B\hat{K}_w \hat{w}_g - w_g \tag{71}$$

The adaptive disturbance gain $\hat{K}_w$ is computed by the direct MRAC update law

$$\dot{\hat{K}}_w^T = \mathit{\Gamma} \hat{w}_g e^T P B \tag{72}$$

where Γ is the MRAC gain matrix and P is the solution to the algebraic Lyapunov equation

$$PA_{ref} + A_{ref}^T P = -Q \tag{73}$$

with $Q > 0$.[16] The stability of the MRAC update law can be shown with Lyapunov stability theorem.

Proof: Choose a Lyapunov candidate function

$$V = e^T P e + \text{trace}\left(\hat{K}_w \Gamma^{-1} \hat{K}_w^T\right) \tag{74}$$

Then, $\dot{V}$ is evaluated as

$$\dot{V} = -e^T Qe + 2e^T P\left(-B\hat{K}_w\hat{w}_g - w_g\right) + 2\text{trace}\left(\hat{K}_w\Gamma^{-1}\dot{\hat{K}}_w^T\right)$$

$$= -e^T Qe - 2\text{trace}\left(\hat{K}_w\hat{w}_g e^T PB\right) - 2e^T Pw_g + 2\text{trace}\left(\hat{K}_w\Gamma^{-1}\dot{\hat{K}}_w^T\right)$$

$$= -e^T Qe - 2e^T Pw_g + 2\text{trace}\left(\hat{K}_w\left(-\hat{w}_g e^T PB + \Gamma^{-1}\dot{\hat{K}}_w^T\right)\right)$$

The definition of the update law becomes

$$-\hat{w}_g e^T PB + \Gamma^{-1}\dot{\hat{K}}_w^T = 0 \Rightarrow \dot{\hat{K}}_w^T = \Gamma\hat{w}_g e^T PB \tag{75}$$

Therefore $\dot{V}$ becomes

$$\dot{V} = -e^T Qe - 2e^T Pw_g \leq -\lambda_{min}(Q)\left\|e\right\|^2 + 2\lambda_{max}(P)\left\|e\right\|\left\|w_g\right\| \tag{76}$$

Thus, $\dot{V} \leq 0$ implies

$$\left\|e\right\| \geq \frac{2\lambda_{max}(P)\left\|w_g\right\|}{\lambda_{min}(Q)} \tag{77}$$

This implies e is bounded as $t \to \infty$. One cannot assume that $e \to 0$ because w_g is unknown.

The total control includes the linear-quadratic optimal control and the active gust load alleviation control

$$u = K_x x + K_z z + \Lambda_0 + \hat{K}_w\hat{w}_g \tag{78}$$

F. VCCTEF Virtual Control Variables

The elastomer transition material between the spanwise flap sections of the VCCTEF limits the relative motion between these sections. The elastomer transition material has certain displacement and rate limits, and consequently the flap sections are also constrained by relative displacement and rate limits. The relative constraints between the spanwise flap sections need to be included in the control design.

The constraints can be expressed as

$$\left|\delta_{i+1} - \delta_i\right| \leq \dot{\delta} \tag{79}$$

$$\left|\dot{\delta}_{i+1} - \dot{\delta}_i\right| \leq \Delta\dot{\delta} \tag{80}$$

where $i = 1, 2, \ldots, m$ is the index of the flap section and m is the total number of spanwise flap sections per wing.

The displacement constraint between each adjacent spanwise flap section for the VCCTEF is assumed to be 2°. The rate constraint is not defined and therefore not considered in this study.

The relative deflection limit is addressed in the control design by implementing a virtual control concept.[1] The deflections of the flap sections are constrained to a mathematical shape function. The actual flap deflections can now be described by a set of virtual control variables. In this study, the spanwise flap sections are constrained to a shape function described by a cubic Chebyshev polynomial of the first kind as[20]

$$\delta_i = c_0 + c_1 k + c_2 \left(2k^2 - 1\right) + c_3 \left(4k^3 - 3k\right) \tag{81}$$

where $k = \frac{i-1}{n-1}$, $i = 1, 2, \ldots, n$, $n = 16$, and $c_j\left(t\right), j = 0, 1, 2, 3$ are the virtual control variables.

The control design determines the commands for the virtual control variables with the implementation of this shape function. Since the shape function in Eq.(81) is linear with respect to the virtual control variables, a transformation matrix can be constructed that relates the physical control variables to the virtual control variables with the use of partial derivation.

IV. Simulations

Simulations are conducted to assess the performance of the active gust load alleviation control method in combination with the multi-objective flight controller. The simulations use the coupled ASE longitudinal dynamic model of the flexible wing GTM with VCCTEF as described in Section II. The wing stiffness is reduced by 50% from the baseline stiffness. The model has five rigid aircraft states in the longitudinal direction, 198 aeroelastic modes with two elastic states and four aerodynamic lag states per mode, two rigid aircraft flight control inputs; namely the engine throttle and elevator each with one actuator state, and 16 VCCTEF inputs to the outermost chordwise flap segments with two actuator states and four aerodynamic lag states per flap segment. Thus, the model has a total of 1307 states and 18 control variables. The model includes an aerodynamic model that computes the aircraft drag coefficient according to Eq.(23), a structural model that computes the wing root bending moment from Eq.(25), as well as accelerometer models that compute the vertical accelerations of the aeroelastic modes at the wing from Eq.(19) and the aircraft center of gravity from Eq.(27).

The controller is built using the reduced-order model that contains the first 10 aeroelastic modes. This reduced-order model has 179 states.

A flight path angle control is designed according to Eq.(30). The flight path angle command γ_c stays equal to 0, resulting in the objective of the baseline controller to stay at normal cruise conditions in the presence of turbulence. Cruise conditions for the GTM with VCCTEF are at Mach 0.797 at an altitude of 36,000 ft.

The optimal baseline controller has the cost weighting matrix $Q\left(x_r, x_e, x_\delta, x_s, x_a\right) = diag(100, 50, 1 \times 10^{-10}, 1 \times 10^{-10}, 1 \times 10^6)$ and the control weighting matrix is selected as $R = 1 \times 10^4 I$. As can be seen from the cost weighting matrix, the aeroelastic mode suppression uses as weighting matrix $Q_e = 50$. The drag minimization uses a weighting coefficient $q_D = 5 \times 10^4$. The nominal rigid controller has the same control weighting matrix and cost weighting matrix $Q\left(x_r, x_\delta, x_s, x_a\right) = diag(100, 1 \times 10^{-10}, 1 \times 10^{-10}, 1 \times 10^6)$.

The disturbance estimation is done using the ESO described in Eq.(64). The observer gains are selected as $\beta_i = 100$ for the rigid-body states x_r, aeroelastic states derivatives $\dot{q}$, and the VCCTEF states derivatives $\dot{\delta}$. Since the other states are not directly affected by the turbulence, their observer gains are kept to 0.

The MRAC update law for the adaptive disturbance gain of the active gust load alleviation control in Eq.(72) is calculated with the MRAC rates of adaptation $\Gamma(x_r) = 1 \times 10^3, \Gamma(x_e) = \Gamma(x_\delta) = 1 \times 10^{-2}$ and weight matrix $Q\left(x_r, x_e, x_\delta, x_s, x_a\right) = diag(5 \times 10^1, 1 \times 10^1, 1 \times 10^{-1}, 0, 0)$.

The simulations consider a 1-dimensional severe von Kármán turbulence model with a turbulence intensity σ of 4.5 and a characteristic length L of $1750 ft$.

A. Aeroelastic State Estimation

The multi-objective flight controller with active gust load alleviation is a feedback control design. This means that the control design needs information about the states. In this study, it is assumed that the rigid-body states x_r, VCCTEF states x_δ, and servo-motor states x_s can be measured. The aeroelastic state vector x_e cannot be measured and therefore needs to be estimated with an observer design.

The inclusion of an observer in the optimal control framework of the multi-objective flight controller transforms the Linear-Quadratic Regulator (LQR) control to Linear-Quadratic Gaussian (LQG) control. The state observer is designed using the Kalman filter optimal estimation method.

The state observer uses the measurements from four accelerometers that are placed in pairs at mid-span and near the wing tip of each wing. The accelerometer pairs are located forward and aft of the elastic axis at the same spanwise location, illustrated by the red dots in Fig.5. This relative positioning of the accelerometer pairs with respect to the elastic axis allows the measurement of both the vertical and angular acceleration of the wing section.

The accelerometer measurements need to be filtered before they can be used in the Kalman filter estimation. This is because of two reasons: 1) measurement noise needs to diminish, and 2) the effect of the high-frequency modes that are removed in the reduced-order model needs to be attenuated. Otherwise, these high-frequency modes can significantly affect the accelerometer output, but this effect is not taken into

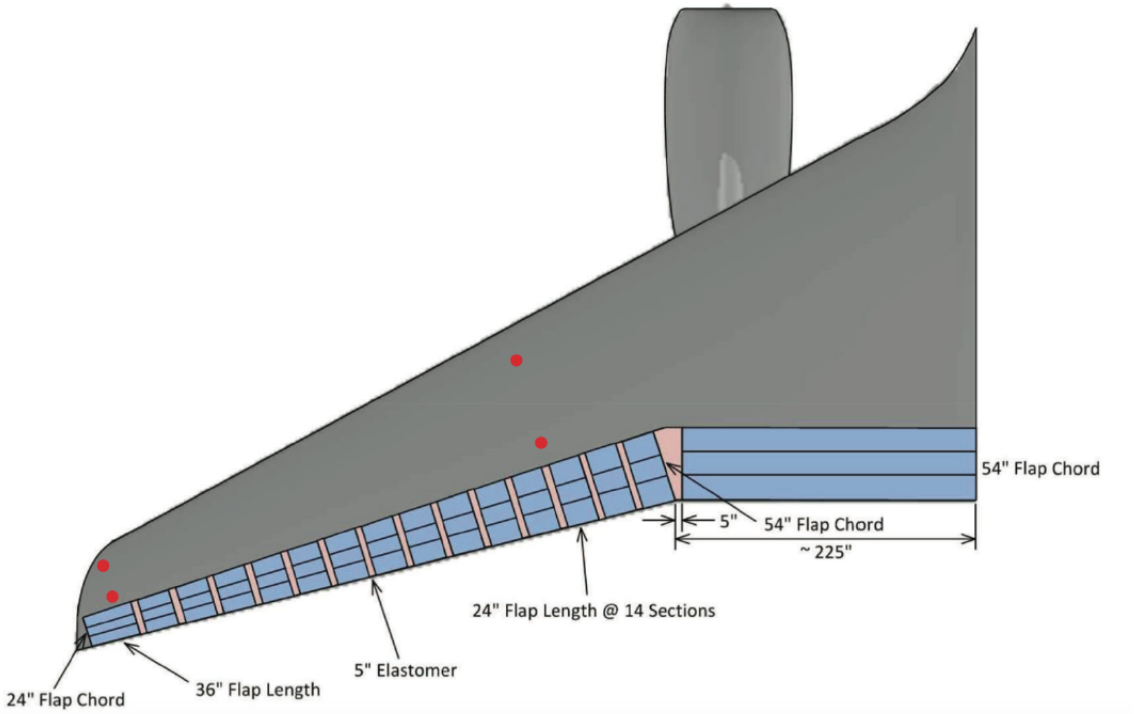

Figure 5. Accelerometer Locations

account in the predicted output of the Kalman filter. The disparity between the measured and predicted output can negatively influence the state estimation. A low-pass filter provides a solution to both problems. The cut-off frequency of the filter should be selected based on the maximum frequency of the aeroelastic modes in the reduced-order model. A Bessel filter is selected since this filter has a limited phase shift and therefore a smaller delay with respect to the accelerometer measurements.[2]

In this simulation study, the outputs of the four accelerometers are modeled by Eq.(19). The Kalman filter estimates the aeroelastic states with

$$\dot{\hat{x}}_e = A_{er}x_r + A_{ee}\hat{x}_e + A_{e\delta}x_\delta + A_{es}x_s + B_e u + z_e + L\left(y_K - \hat{y}\right) \tag{82}$$

where L is the optimal Kalman filter gain and $\hat{y}$ is the estimated output as

$$\hat{y} = C\left[\begin{array}{ccccc} x_r^T & \hat{x}_e^T & x_\delta^T & x_s^T & x_a^T \end{array}\right]^T + Du \tag{83}$$

and y_K is the filtered accelerometer output given by

$$y_K = F(s)\left(y + v\right) \tag{84}$$

where $F(s)$ is the transfer function of the Bessel filter and v is the measurement noise. The measurement noise is modeled as white noise.

By implementing the state estimates in the controller design of Eq.(78), the multi-objective flight controller with active gust load alleviation becomes

$$u = K_x\hat{x} + K_z z + \Lambda_0 + \hat{K}_w\hat{w}_g \tag{85}$$

where $x = \begin{bmatrix} x_r^T & \hat{x}_e^T & x_\delta^T & x_s^T & x_a^T \end{bmatrix}^T$.

B. Performance Metrics for Gust Load Alleviation

The goal of the simulations is to assess the performance of the active gust load alleviation control method. Several performance metrics have been used in previous research on gust load alleviation to analyze the controller performance. In this study, five performance metrics will be analyzed

1. The sum of the Euclidean norm of the rigid-body states

$$\sum_{i=1}^{m_r} \|x_r - x_{ref,r}\| = \sum_{i=1}^{m_r} \left(\sum_{j=1}^{n} |x_{r,ij}|^2 \right)^{1/2} \tag{86}$$

where n is the number of samples and m_r is the number of rigid-states.

2. The sum of the Euclidean norm of the aeroelastic states

$$\sum_{i=1}^{m_e} \|x_e - x_{ref,e}\| = \sum_{i=1}^{m_e} \left(\sum_{j=1}^{n} |x_{e,ij}|^2 \right)^{1/2} \tag{87}$$

where m_e is the number of elastic states.

3. The Euclidean norm of the flight path angle γ

$$\|\gamma - \gamma_{ref}\| = \left(\sum_{j=1}^{n} |\gamma_j|^2 \right)^{1/2} \tag{88}$$

4. The root-mean-square incremental vertical acceleration at the center of gravity of the aircraft

$$A_{z,rms} = \sqrt{\frac{1}{n} \sum_{i=1}^{n} \Delta A_{z,i}^2} \tag{89}$$

5. The root-mean-square bending moment at the wing root

$$M_{y,rms} = \sqrt{\frac{1}{n}\sum_{i=1}^{n} M_{y,i}^2} \tag{90}$$

In previous research,[21–24] the wing root bending moment M_y and the rigid-body x_r and elastic state x_e responses have been selected as the main performance metrics to consider. Consequently, the performance metrics relating to these variables (1, 2, and 5) will be considered to be of most importance.

Furthermore, the drag minimization control feature is also analyzed. The incremental drag is calculated according to Eq.(24).

C. Simulation Results

This section contains the results of the simulations for the flexible wing GTM aircraft in symmetric cruise conditions subjected to severe von Kármán turbulence. The performance of seven different controllers is analyzed and compared:

1. Nominal Rigid Controller (NRC)
2. Linear-Quadratic Regulator Control (LQR)
3. Linear-Quadratic Regulator Control with Drag Minimization (LQR + DM)
4. Linear-Quadratic Regulator Control with Drag Minimization and Active Gust Load Alleviation (LQR + DM + GLA)
5. Linear-Quadratic Gaussian Control (LQG)
6. Linear-Quadratic Gaussian Control with Drag Minimization (LQG + DM)
7. Linear-Quadratic Gaussian Control with Drag Minimization and Active Gust Load Alleviation (LQG + DM + GLA)

The difference between LQR and LQG is that the LQR controller assumes that all the states can be measured, while the LQG controller needs the Kalman filter estimation of the aeroelastic states. Both the LQR and LQG controller include the aeroelastic mode suppression objective ($Q_e = 50$). Drag minimization is added to the controller by switching the drag weighting coefficient q_D from 0 to 5×10^4.

Tables 1 and 2 show the performance metric results of the flight dynamic, structural and aerodynamic responses. In these tables both the LQR and LQG simulations are shown. The LQG simulations represent the most realistic scenario, in which the aeroelastic states cannot be measured but need to be estimated with the use of a Kalman filter. This state estimation introduces errors in the control method. For this reason, the LQR simulations are also shown. The LQR simulations show the performance of the aeroelastic mode suppression, drag minimization, and active gust load alleviation without the interference of state estimation errors.

	$\sum \lVert x_r - x_{ref,r} \rVert$	%	$\sum \lVert x_e - x_{ref,e} \rVert$	%	$\lVert \gamma - \gamma_{ref} \rVert$	%
NRC	0.395	0	20.355	0	1.169	0
LQR	0.368	-7	11.735	-42	1.521	30
LQR + DM	0.289	-27	9.755	-52	0.876	-25
LQR + DM + GLA	0.114	-71	14.078	-80	0.665	-43
LQG	0.461	17	17.886	-12	0.366	-69
LQG + DM	0.321	-19	11.732	-42	0.604	-48
LQG + DM + GLA	0.175	-56	6.078	-70	0.724	-38

Table 1. Performance Metrics Results: Flight Dynamic Responses

First of all, the aeroelastic mode suppression is noticeable by considering the sum of the Euclidean norm of the aeroelastic states $\sum \lVert x_e - x_{ref,e} \rVert$. The LQR and LQG controllers significantly suppress the aeroelastic responses. Furthermore, the Euclidean norms of the rigid-body states $\sum \lVert x_r - x_{ref,r} \rVert$ and aeroelastic states $\sum \lVert x_e - x_{ref,e} \rVert$ show the ability of the active gust load alleviation control to significantly counteract the effects of the turbulence. The drag minimization objective also suppresses the rigid-body and aeroelastic states. The performance metric related to the flight path angle $\lVert \gamma - \gamma_{ref} \rVert$ shows an increase in performance for the LQR controllers when adding drag minimization and active gust load alleviation. The LQG controller, however, shows the opposite effect with respect to this flight path angle performance metric. The contrary results could be caused by errors in the aeroelastic state estimation.

	$A_{z,rms}$ $[ft/s^2]$	%	$M_{y,rms}$ $[ft-lb]$	%	ΔC_D [dragcount]	%
NRC	0.482	0	63598	0	18	0
LQR	0.296	-39	26352	-59	23	28
LQR + DM	0.241	-50	15374	-76	21	17
LQR + DM + GLA	0.268	-44	10584	-83	18	0
LQG	0.187	-61	46289	-27	21	17
LQG + DM	0.235	-51	29781	-53	19	6
LQG + DM + GLA	0.269	-44	10533	-83	19	6

Table 2. Performance Metrics Results: Structural and Aerodynamic Responses

The results in Table 2 show the ability of active gust load alleviation to significantly decrease the root-mean-square of the wing root bending moment $M_{y,rms}$. As mentioned earlier, the wing root bending moment is a main criterion in the analysis of gust load alleviation controls. The vertical acceleration of the center of gravity $A_{z,rms}$ decreases when including aeroelastic mode suppression, but does not show a coherent relation with the controller type. The incremental drag ΔC_D is lowest for the nominal rigid controller. However, the effect of drag minimization control is certainly noticeable when comparing the LQR and LQG controllers with the LQR and LQG controllers with drag minimization.

Figure 6 shows the incremental rigid-body response of the aircraft to the severe von Kármán turbulence. The plots compare the responses of the nominal rigid controller, the LQG controller with aeroelastic mode suppression, the LQG controller with aeroelastic mode suppression and drag minimization and the LQG controller with aeroelastic mode suppression, drag minimization, and active gust load alleviation. The angle of attack $\Delta\alpha$ and pitch angle $\Delta\theta$ illustrate the improvements gained by including drag minimization and the significant improvement when including active gust load alleviation. The pitch rate Δq shows a clear improvement of all the LQG controllers with respect to the nominal rigid controller. Furthermore, active gust load alleviation shows the largest improvement in suppressing the response of the pitch rate. The flight path angle γ response benefits the most from aeroelastic mode suppression, and all LQG controllers perform better than the nominal rigid controller.

Figure 7 shows the response of the first three aeroelastic modes. The effect of active gust load alleviation is clearly visible. The LQG controller with mode suppression, drag minimization, and active gust load alleviation performs best in suppressing the aeroelastic states.

Figure 8 shows the control surface deflections of the elevator and the VCCTEF. The VCCTEF sections are numbered from 1 at the wing root to 16 at the wing tip. The elevator deflections are well within the standard elevator deflection limit of 25° and the deflection rates are well-behaved. The VCCTEF deflections are illustrated separately for the four different controllers. For all control methods the VCCTEF deflections are well-behaved and within the deflection limit of 20°. Furthermore, the deflection limit constraint of 2° between each adjacent flap section is obeyed. The inclusion of the aeroelastic mode suppression objective results in higher control surface deflections.

Figure 9 shows the wing root bending moment response ΔM_y, vertical acceleration at the center of gravity response ΔA_z, and the incremental drag response ΔC_D. The wing root bending moment is significantly decreased with the use of active gust load alleviation. The vertical acceleration at the center of gravity is mainly suppressed by the aeroelastic mode suppression objective. The incremental drag is lowest for the nominal rigid controller. However, the drag minimization objective decreases the incremental drag with respect to the LQG controller.

Figure 10 shows the results of the ESO disturbance estimation. In this figure, the estimations of the disturbance to the angle of attack w_{g_α} and the disturbance to the first aeroelastic mode $w_{g_{q1}}$ are compared for the LQR and LQG simulations. First of all, for both the LQR and LQG simulations the estimation of the disturbance to the angle of attack is reasonably accurate. Secondly, the estimation of the disturbance to the first aeroelastic mode is again accurate for the LQR simulation, but far off for the LQG simulation.

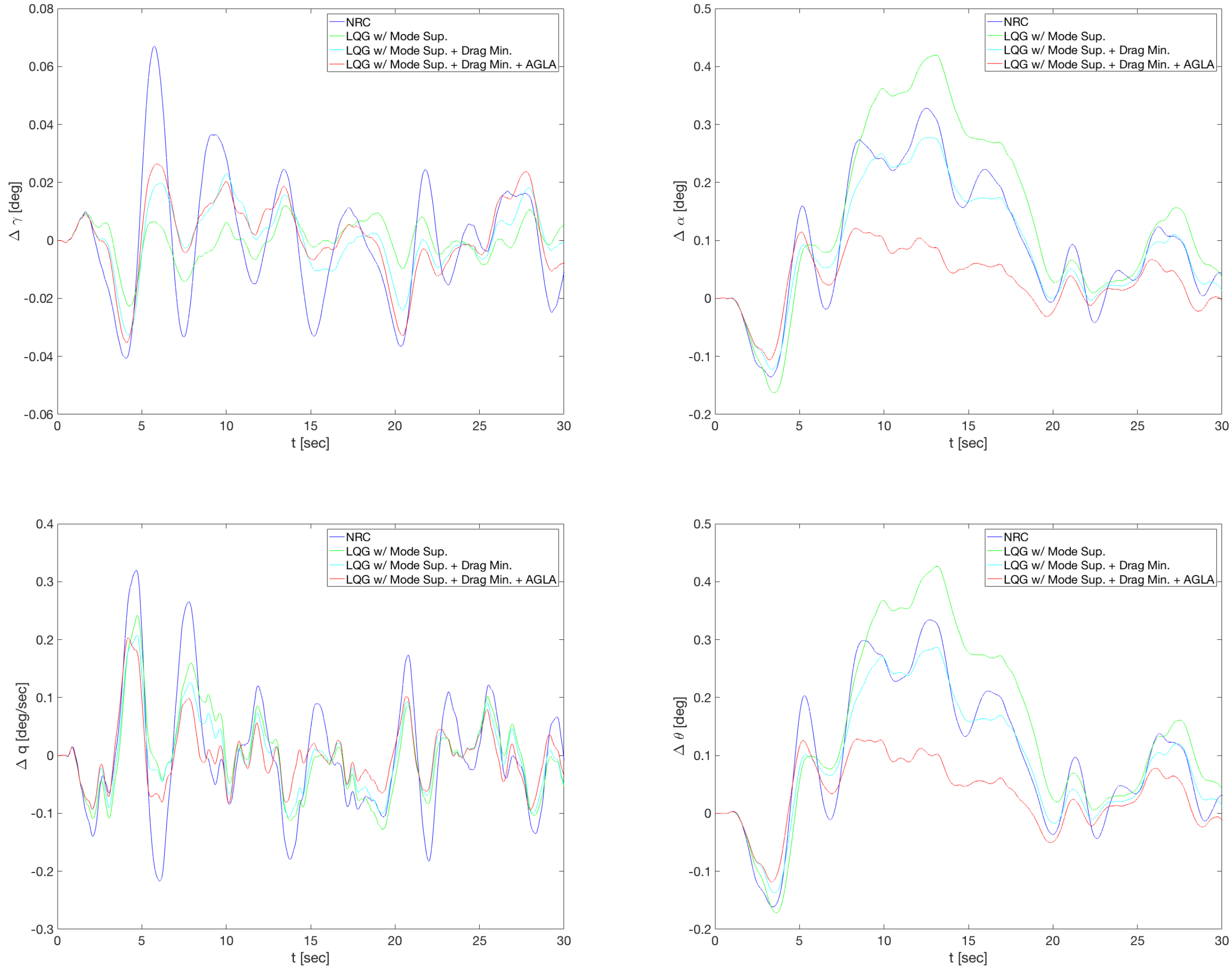

Figure 6. Rigid Aircraft Response to Multi-Objective Flight Control with Mode Suppression, Drag Minimization and Active Gust Load Alleviation

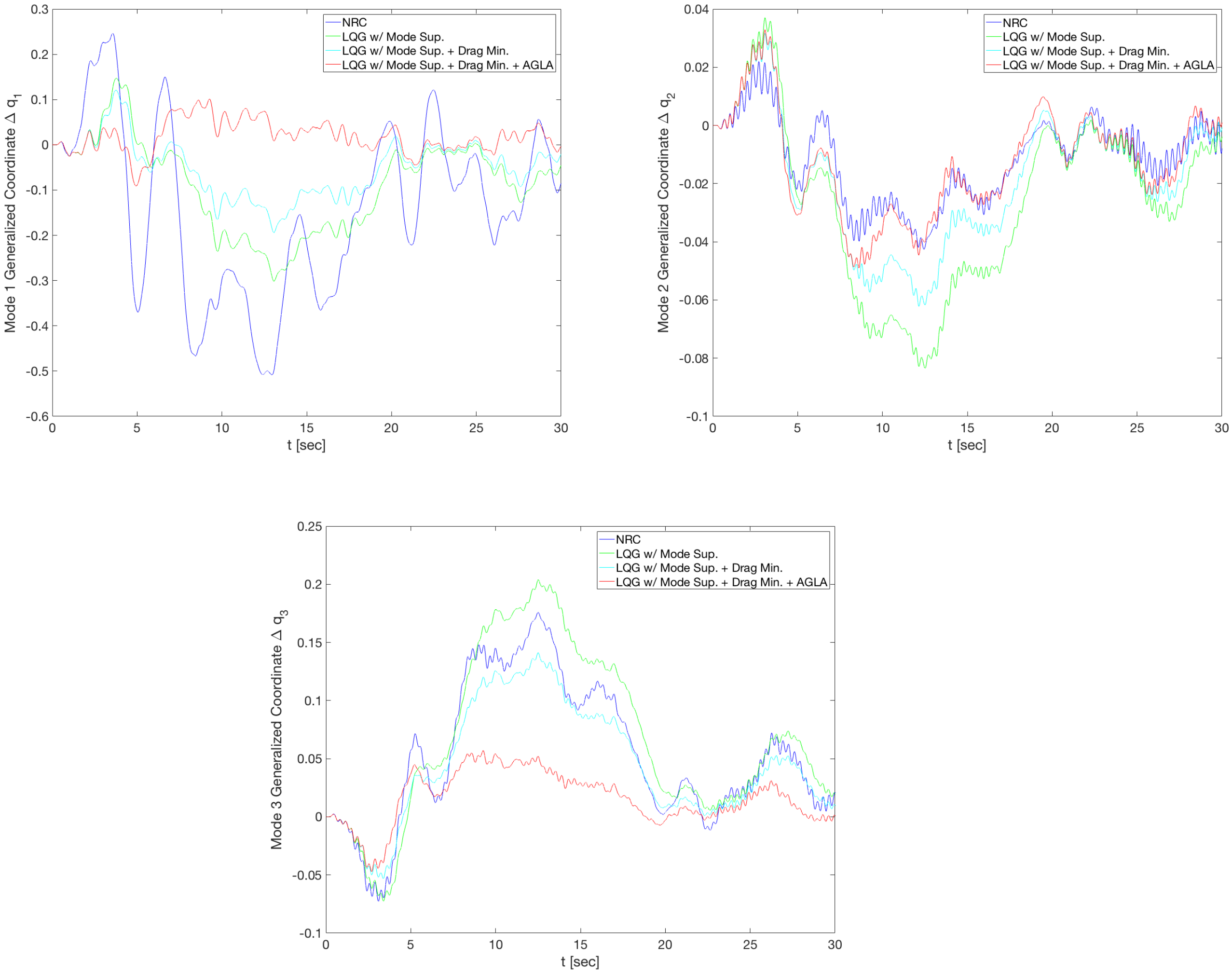

Figure 7. Elastic Response to Multi-Objective Flight Control with Mode Suppression, Drag Minimization and Active Gust Load Alleviation

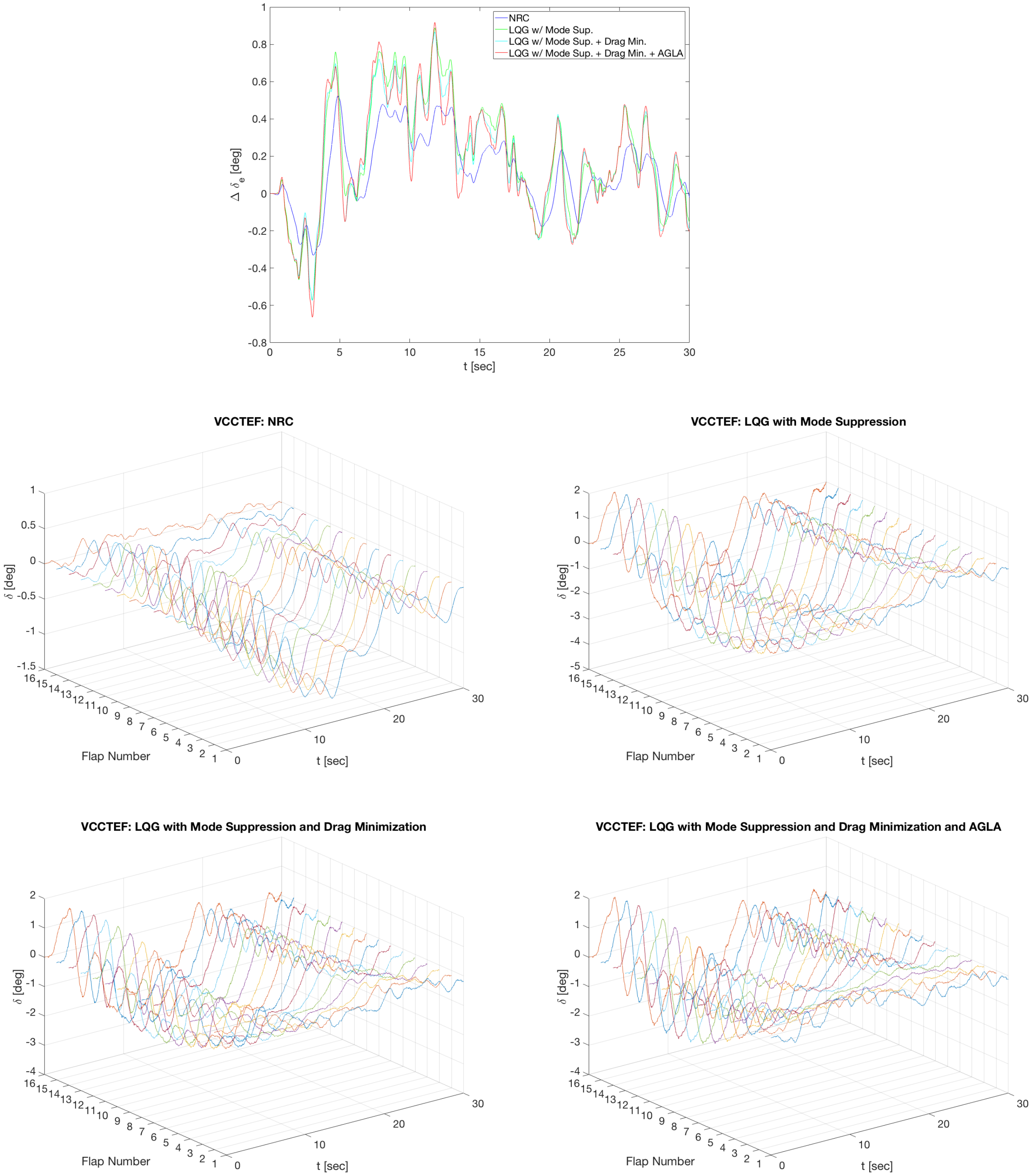

Figure 8. Control Surface Deflections for Multi-Objective Flight Control with Mode Suppression and Drag Minimization

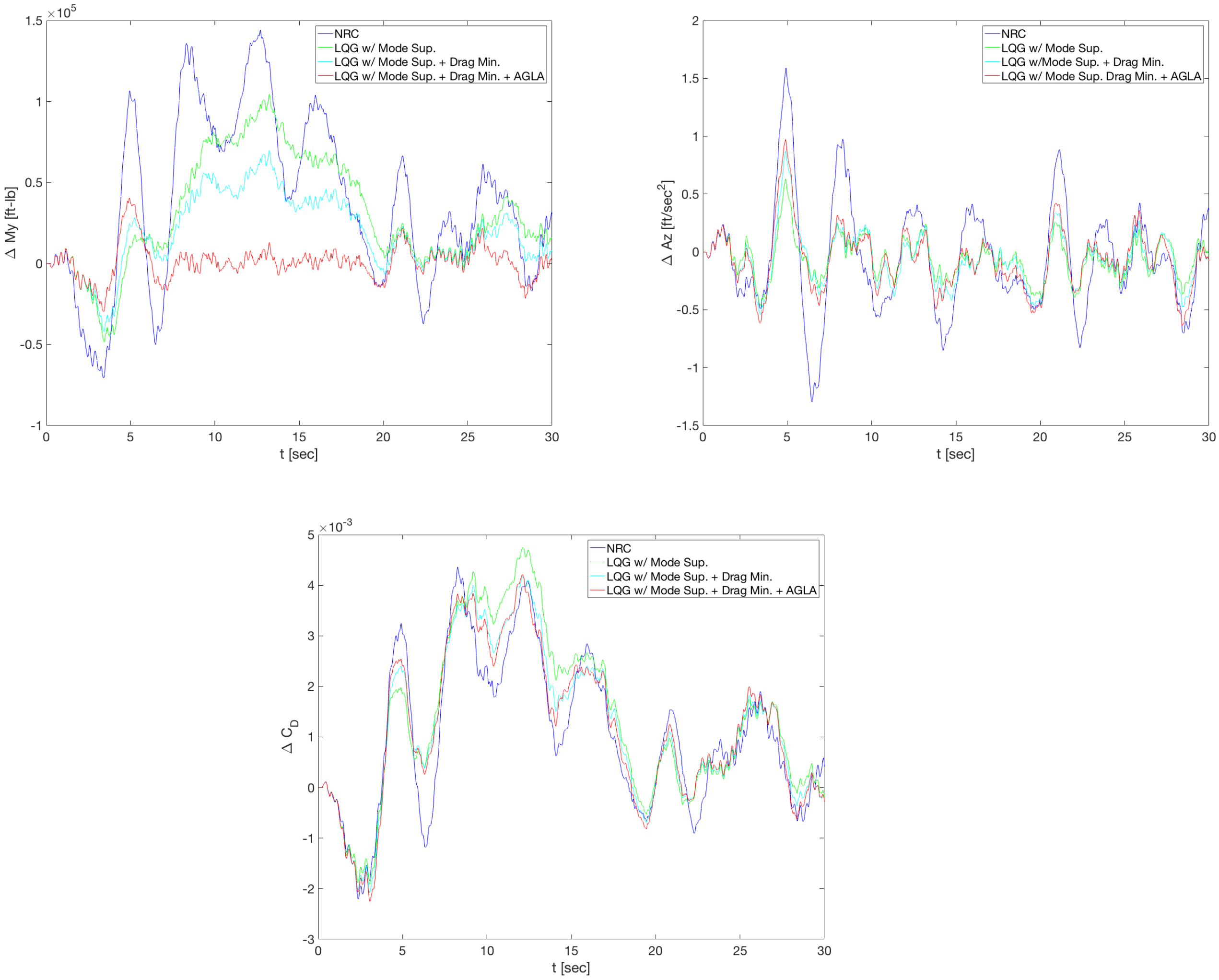

Figure 9. Performance Response to Multi-Objective Flight Control with Mode Suppression, Drag Minimization and Active Gust Load Alleviation

This means that the errors between the actual and estimated aeroelastic states significantly impact the ESO estimation of the disturbances related to the aeroelastic states. Both the disturbance estimations for the LQR and LQG controllers show a phase lag with respect to the real disturbance. This lag decreases the performance of the controllers.

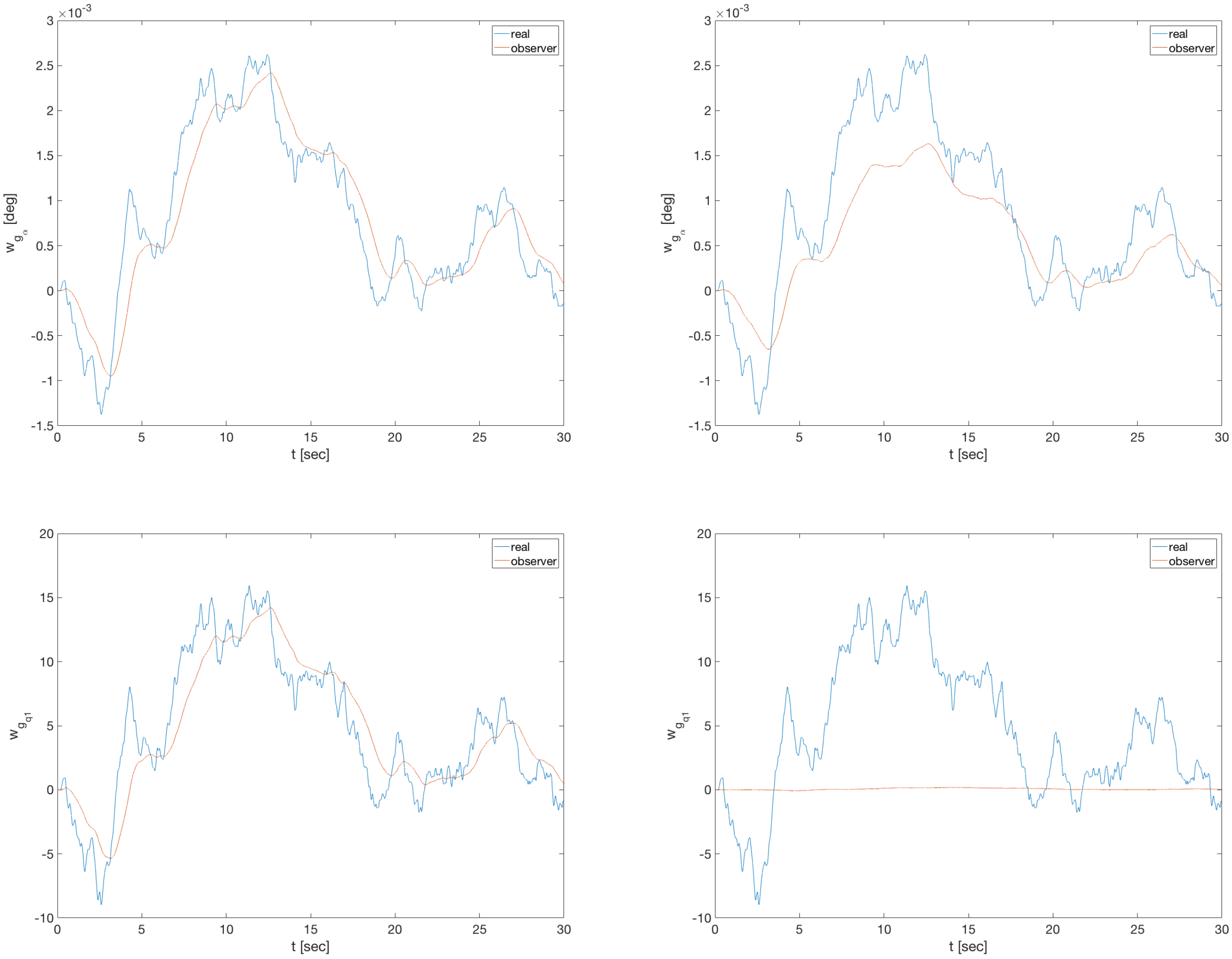

Figure 10. ESO Disturbance Estimation

D. Validation

The active gust load alleviation control is validated for six additional turbulence models.

1. Dryden Light with intensity $\sigma = 1.5$ and characteristic length $L = 1750ft$
2. Dryden Moderate with intensity $\sigma = 1.5$ and characteristic length $L = 1750ft$
3. Dryden Severe with intensity $\sigma = 3.0$ and characteristic length $L = 1750ft$
4. von Kármán Light with intensity $\sigma = 3.0$ and characteristic length $L = 1750ft$

5. von Kármán Moderate with intensity $\sigma = 5.0$ and characteristic length $L = 1750ft$
6. von Kármán Severe with intensity $\sigma = 5.0$ and characteristic length $L = 1750ft$

The validation results are summarized in Table 3. Table 3 shows the difference in performance metrics in percentage when comparing the LQG controller with and without active gust load alleviation. A negative value indicates an increase in performance while a positive values indicates a decrease in performance. For all six turbulence models, active gust load alleviation increases the performance with respect to the rigid-body states $\sum \|x_r - x_{ref,r}\|$, aeroelastic states $\sum \|x_e - x_{ref,e}\|$, and wing root bending moment $M_{y,rms}$. However, it decreases the performance with respect to the flight path angle $\|\gamma - \gamma_{ref}\|$ and does not show any coherent relation with respect to the vertical acceleration at the center of gravity $A_{z,rms}$.

	$\sum \|x_r - x_{ref,r}\|$ [%]	$\sum \|x_e - x_{ref,e}\|$ [%]	$\|\gamma - \gamma_{ref}\|$ [%]	$A_{z,rms}$ [%]	$M_{y,rms}$ [%]
Dryden Light	-21	-17	5	-6	-18
Dryden Moderate	-45	-42	23	2	-43
Dryden Severe	-49	-47	21	-1	-38
von Kármán Light	-31	-40	29	3	-29
von Kármán Moderate	-53	-57	35	1	-59
von Kármán Severe	-38	-43	0	2	-45

Table 3. Validation Results for Active Gust Load Alleviation

V. Discussion

It is important to qualify the limitations and assumptions in this study that may affect the active gust load alleviation assessments.

First, the Kalman filter state estimation needs to be improved in order to improve the performance of the controller and the ESO estimation of the disturbances. The LQR simulation results have indicated the ability of the active gust load alleviation to significantly improve the performance metrics for the rigid-body and aeroelastic responses, wing root bending moment, vertical acceleration of the center of gravity and even the incremental drag. It is expected that the closer the estimation of the aeroelastic states complies with the actual aeroelastic states, the better the LQG controller with active disturbance rejection will perform. Furthermore, the illustration of the ESO disturbance estimation in Fig.10 shows that the ESO disturbance estimation performs very well for the LQR simulations. Following the same line of reasoning, it is expected that a close compliance between the estimates of the aeroelastic states and actual aeroelastic states improves the ESO disturbance estimation for the LQG simulations. A more accurate estimation of the disturbances will improve the active gust load alleviation control.

Secondly, Lyapunov stability theorems are used in general to proof that an MRAC update law is stable. However, in the presence of a bounded disturbance, such as turbulence w_g, only bounded tracking can be accomplished. Furthermore, the robustness of the MRAC update law can be increased by using a robust modification scheme such as optimal control modification.[17, 18] Future research should look into the application of the optimal control modification in active gust load alleviation.

Thirdly, this study does not consider any constraints on the rate of the VCCTEF and no lag in the actuator response. Active gust load alleviation requires a highly reactive flap system. In reality, rate constraints and controller lag for the VCCTEF can decrease the performance of the active gust load alleviation control. Future research should study these limitations.

Furthermore, in this study, the VCCTEF is constrained to follow a cubic Chebyshev polynomial shape function. It is plausible that a higher order or more flexible shape function can improve the controller performance by allowing more degrees of freedom. Future research should look into the effect of the shape constraint on the multi-objective flight control and active gust load alleviation control performance.

Finally, stability margins of the controllers should be analyzed to determine how robust they are. This can be done by injecting a time delay at the input to assess the time delay margin of the controllers. The LQR is expected to be most robustly stable among all the controllers but it is not realizable. On the other hand, the LQG design can be designed with a Loop Transfer Recovery (LTR) method to provide a stability margin close to that of the LQR.[16, 19]

VI. Conclusions

This paper presents a multi-objective flight control framework for aeroelastic mode suppression, drag minimization, and active gust load alleviation. The present study is an extension of the previous development of multi-objective flight control for flexible aircraft equipped with multi-functional flight control surfaces such as the Variable Camber Continuous Trailing Edge Flap system. The multi-objective flight control addresses multiple competing needs in a flight control design to achieve the goals of maximizing the aerodynamic performance of an aircraft, minimizing structural loads and aeroelastic response of the wing structure, and tracking a pilot command. The aerodynamic performance and structural response objectives are integrated into the traditional cost function of linear-quadratic optimal control to synthesize a multi-objective flight control design. Active gust load alleviation is added to the flight control framework by augmenting the linear-quadratic optimal controller with an adaptive increment. This adaptive increment is designed using Model Reference Adaptive Control and Extended State Observers. The Extended State Observers are used to estimate the turbulence in flight. Simulations of the multi-objective flight control are conducted for a flexible wing NASA Generic Transport Model. The results demonstrate the effectiveness of the active gust load alleviation approach within a multi-objective flight control framework that includes aeroelastic mode suppression, drag minimization, and gust load alleviation.

Acknowledgements

The authors would like to thank the Fixed Wing / Advanced Air Transport Technology Project under the Advanced Air Vehicles Program of NASA Aeronautics Research Mission Directorate (ARMD) for funding support of this work.

References

[1] Nguyen, N. and Urnes, J., “Aeroelastic Modeling of Elastically Shaped Aircraft Concept via Wing Shaping Control for Drag Reduction," AIAA Atmospheric Flight Mechanics Conference, AIAA-2012-4642, August 2012.

[2] Nguyen, N. and Tal, E., “A Multi-Objective Flight Control Approach for Performance Adaptive Aeroelastic Wing,” 56th AIAA/ASCE/AHS/ASC Structures, Structural Dynamics, and Materials Conference (AIAA Science and Technology Forum), January 2015.

[3] Nguyen, N., Ting, E., Chaparro, D., Drew, M., and Swei, S., “Multi-Objective Flight Control for Drag Minimization and Load Alleviation of High-Aspect Ratio Flexible Wing Aircraft,” 58th AIAA/ASCE/AHS/ASC Structures, Structural Dynamics, and Materials Conference, AIAA 2017-1589, January 2017.

[4] Nguyen, N., “Elastically Shaped Future Air Vehicle Concept,” NASA Innovation Fund Award 2010 Report, October 2010, Submitted to NASA Innovative Partnerships Program, http://ntrs.nasa.gov/archive/nasa/casi.ntrs.nasa.gov/20110023698.pdf.

[5] Nguyen, N., Trinh, K., Reynolds, K., Kless, J., Aftosmis, M., Urnes, J., and Ippolito, C., “Elastically Shaped Wing Optimization and Aircraft Concept for Improved Cruise Efficiency,” AIAA Aerospace Sciences Meeting, AIAA-2013-0141, January 2013.

[6] Urnes, J., Nguyen, N., Ippolito, C., Totah, J., Trinh, K., and Ting, E., “A Mission Adaptive Variable Camber Flap Control System to Optimize High Lift and Cruise Lift to Drag Ratios of Future N+3 Transport Aircraft,” AIAA Aerospace Sciences Meeting, AIAA-2013-0214, January 2013.

[7] Lebofsky, S., Ting, E., and Nguyen, N., “Aeroelastic Modeling and Drag Optimization of Flexible Wing Aircraft with Variable Camber Continuous Trailing Edge Flap,” 32nd AIAA Applied Aerodynamics, AIAA 2014-2443, June 2014.

[8] Ferrier, Y., Nguyen, N., and Ting, E., “Real-time Adaptive Least-Squares Drag Minimization for Performance Adaptive Aeroelastic Wing,” 34th AIAA Applied Aerodynamics, AIAA 2016-3567, June 2016.

[9] Nguyen, N., Ting, E., Chaparro, D., Drew, M., and Swei, S., “Multi-Objective Flight Control for Drag Minimization and Load Alleviation of High-Aspect Ratio Flexible Wing Aircraft,” 58th AIAA/ASCE/AHS/ASC Structures, Structural Dynamics, and Materials Conference. AIAA 2017-1589, January 2017.

[10] Kaul, U. and Nguyen, N., “Drag Optimization Study of Variable Camber Continuous Trailing Edge Flap (VCCTEF) Using OVERFLOW,” 32nd AIAA Applied Aerodynamics, AIAA 2014-2444, June 2014.

[11] Nguyen, N., Ting, E., Nguyen, D., and Trinh, K., “Flight Dynamic Modeling and Stability Analysis of Flexible Wing Generic Transport Aircraft,” 55th AIAA/ASME/ASCE/AHS/ASC Structures, Structural Dynamics, and Materials Conference, AIAA-2014-1040, January 2014.

[12] Tal, E. and Nguyen, N., “Unsteady Aeroservoelastic Modeling of Flexible Wing Generic Transport Aircraft with Variable

Camber Continuous Trailing Edge Flap," 33rd AIAA Applied Aerodynamics Conference, AIAA 2015-2722, June 2015.

[13] Tal, E., Nguyen, N. and Ting, E., "Comparison of Unsteady Aerodynamics Approximations for Time-Domain Representation of Frequency-Independent Aeroelastic State-Space Models," 56th AIAA/ASME/ASCE/AHS/ASC Structures, Structural Dynamics, and Materials Conference, January 2015.

[14] Han, J., Control and Decision **138**, Vol. 85, 1995.

[15] Erazo, C., Angulo, F., and Olivar, G., "Stability analysis of the extended state observers by Popov criterion," Theoretical & Applied Mechanics Letters **2**, 043006, 2012.

[16] Lavretsky, E., and Wise, K.A., "Robust and Adaptive Control, with Aerospace Applications," Springer-Verlag, London, 2013, pp. 281-292.

[17] Nguyen, N., Krishnakumar, K., and Boskovic, J., "An Optimal Control Modification to Model-Reference Adaptive Control for Fast Adaptation," AIAA Guidance, Navigation and Control Conference and Exhibit, AIAA 2008-7283, August 2008.

[18] Nguyen, N., "Optimal Control Modification for Robust Adaptive Control with Large Adaptive Gain," Systems & Control Letters, 61 (2012) pp. 485-494.

[19] Stengel, R., "Optimal Control and Estimation," Dover Publications, New York, 1994.

[20] Nguyen, N., Hashemi, K.E., Yucelen, T., and Arabi, E., "Performance Optimizing Multi-Objective Adaptive Control with Time-Varying Reference Model Modification," AIAA Guidance, Navigation, and Control Conference, AIAA-2017-1715, January 2017.

[21] Liu, X., and Sun, Q., "Gust Load Alleviation with Robust Control for a Flexible Wing," Shock and Vibration, Volume 2017, Article ID 1060574, Hindawi Publishing Corporation, November 2015.

[22] Alam, M., Hromcik, M., and Hanis, T., "Active gust load alleviation system for flexible aircraft: Mixed feedforward/feedback approach," Aerospace Science and Technology, 41 (2015) pp. 122-133, Elsevier, December 2014.

[23] Haghighat, S., Liu, H.H.T., and Martins, J.R.R.A., "Model-Predictive Gust Load Alleviation Controller for a Highly Flexible Aircraft," Journal of Guidance, Control, and Dynamics, Vol. 35, No.6, November-December 2012.

[24] Frost, S.A., Taylor, B.R., and Bodson, M., "Investigation of Optimal Control Allocation for Gust Load Alleviation in Flight Control," AIAA Atmospheric Flight Mechanics Conference, AIAA 2012-4858, August 2012.

[25] Huang, Y., Xu, K., Han, J., and Lam, J., Flight Control Design using Extended State Observer and Non- Smooth Feedback, 40th IEEE Conference on Decision and Control, 2001.

[26] Drela, M., and Youngren, H., AVL 3.26 User Primer, MIT Aero/Astro, Aerocraft, Inc., Cambridge, MA, 2006.

[27] Theodorsen, T., "General Theory of Aerodynamic Instability and the Mechanism of Flutter," NACA-TR-496, January 1949.

[28] Basappa and Jategaonkar, R.V., "Evaluation of Recursive Methods for Aircraft Parameter Estimation," AIAA Atmospheric Flight Mechanics Conference and Exhibit, AIAA 2004-5063, August 2004.

[29] Su, W., Reich, G., "Modeling of Artificial Hair Sensors for Vibration Control of Flexible Wings," AIAA/ASCE/AHS/ASC Structures, Structural Dynamics, and Materials Conference, AIAA-2016-1958, January 2016.

[30] Boeing Report No. 2012X0015, "Development of Variable Camber Continuous Trailing Edge Flap System," October 4, 2012.

[31] Nguyen, N, Precup, N., Urnes, J., Nelson, C., Lebofsky, S., Ting, E., and Livne, E., "Experimental Investigation of a Flexible Wing with a Variable Camber Continuous Trailing Edge Flap Design," 32nd AIAA Applied Aerodynamics Conference, AIAA-2014-2442, June 2014.

[32] Nguyen, N., Ting, E., Nguyen, D., Trinh, K., "Flutter Analysis of Mission-Adaptive Wing with Variable Camber Contin-

uous Trailing Edge Flap," 55th AIAA/ASME/ASCE/AHS/ASC Structures, Structural Dynamics, and Materials Conference, AIAA-2014-0839, January 2014.

[33] Nguyen, N., Swei, S., and Ting, E., "Adaptive Linear Quadratic Gaussian Optimal Control Modification for Flutter Suppression of Adaptive Wing," AIAA Infotech@Aerospace Conference, AIAA 2015-0118, January 2015.

[34] Kokotovic, P., Khalil, H., and O'Reilly, J., *Singular Perturbation Methods in Control: Analysis and Design*, Society for Industrial and Applied Mathematics, 1987.

[35] Ardema, M., "Computational Singular Perturbation Method for Dynamical Systems", AIAA Journal of Guidance, Control, and Dynamics, Vol. 14, pp. 661-663, 1981.

[36] Ippolito C. and Nguyen, N., "A Preliminary Study for Optimal Longitudinal-Mode Flight Control through Distributed Aeroelastic Shaping," 55th AIAA/ASME/ASCE/AHS/ASC Structures, Structural Dynamics, and Materials Conference, AIAA-2014-1044, January 2014.

[37] Brown, N. and Schaefer, J., "Peak-Seeking Optimization of Trim for Reduced Fuel Consumption: Flight-Test Results," AIAA Guidance, Navigation, and Control Conference, AIAA-2013-5171, August 2013.

[38] Nobbs, S.G., "Development of the Full-Envelope Performance Seeking Control Algorithm," 28th AIAA Joint Propulsion Conference, AIAA-1992-3748, July 1992.

A. Optimal Disturbance Gain

This appendix shows the derivation of the optimal disturbance gain K_w. Consider our system

$$\dot{x} = Ax + Bu + z + w_g \tag{91}$$

An optimal control is designed with the following cost function

$$J = \frac{1}{2}\int_0^{t_f} \left(x^T Q x + u^T R u\right) dt \tag{92}$$

where $Q = Q_r \oplus Q_e \oplus Q_\delta \oplus Q_s \oplus Q_a > 0$.

We define the Hamiltonian as

$$H = \frac{1}{2}\left(x^T Q x + u^T R u\right) + \lambda^T \left(Ax + Bu + z + w_g\right) \tag{93}$$

The adjoint equation and optimal control are obtained as

$$\dot{\lambda} = -\frac{\partial H^T}{\partial x} = -Qx - A^T\lambda \tag{94}$$

$$\frac{\partial H^T}{\partial u} = Ru + B^T\lambda = 0 \Rightarrow u = -R^{-1}B^T\lambda \tag{95}$$

Let $\lambda = Wx + Vz + T$. Then

$$\dot{W}x + W\dot{x} + \dot{V}z + V\dot{z} + \dot{T} = -Qx - A^T\left(Wx + Vz + T\right) \tag{96}$$

In this study, the command flight path angle γ_c is constant and therefore $\dot{\gamma}_c = 0$. Let $t_f \to \infty$, then the optimal solution approaches a steady state solution. Therefore, according to the transversality condition, $\dot{W}\left(t_f\right) = 0$ and $\dot{V}\left(t_f\right) = 0$. Then, separating terms yields the following expressions

$$WA + A^TW - WBR^{-1}B^TW + Q = 0 \tag{97}$$

$$V = -\left(A^T - WBR^{-1}B^T\right)^{-1} W \tag{98}$$

$$\dot{T} = -\left(A^T - WBR^{-1}B^T\right) T - W\hat{w}_g \tag{99}$$

Equation 99 needs to be calculated numerically. This is done with the following derivation

$$\dot{T} = \frac{T_{i+1} - T_i}{\Delta t} = -\left(A^T - WBR^{-1}B^T\right)T - W\hat{w}_g \tag{100}$$

$$T_{i+1} = T_i - \Delta t\left(\left(A^T - WBR^{-1}B^T\right)T - W\hat{w}_g\right) \tag{101}$$

In the presence of state and disturbance estimation, the multi-objective flight controller is expressed as

$$u = K_x\hat{x} + K_z z + K_w \tag{102}$$

where

$$K_x = -R^{-1}B^T W \tag{103}$$

$$K_z = -R^{-1}B^T V \tag{104}$$

$$K_w = -R^{-1}B^T T \tag{105}$$

Another approach would be to define λ as $\lambda = Wx + Vz + T\hat{w}_g$. The adjoint equation in Eq.94 then becomes

$$\dot{W}x + W\dot{x} + \dot{V}z + V\dot{z} + \dot{T}\hat{w}_g + T\dot{\hat{w}}_g = -Qx - A^T\left(Wx + Vz + T\hat{w}_g\right) \tag{106}$$

It is invalid to assume that $\dot{\hat{w}}_g = 0$ and therefore Eq.106 cannot be solved analytically nor numerically.